UNIVERSITÀ
DEGLI STUDI
DI PADOVA

Department of Civil, Environmental and Architectural Engineering
Ph. D Course in Science of Civil, Environmental and Architectural Engineering
Curriculum: Risk, vulnerability, environment, health and territory
XXXV Cycle

Numerical modeling for groundwater protection in the Venetian plain between the Brenta and Piave Rivers

Thesis written with the financial contribution of Alto Trevigiano Servizi and UniSmart

Coordinator: Prof. Massimiliano Ferronato
Supervisor: Prof. Matteo Camporese
Co-supervisor: Prof. Paolo Salandin

Ph. D. Student: Beatrice Gatto
Badge number: 1220396

Summary

Abstract

This Ph.D. thesis tackles the scientific challenges that a water utility company in northeast Italy, Alto Trevigiano Servizi, must face in the elaboration of the Water Safety Plan (WSP), which is the most effective preventive tool to ensure good quality water and consumer health protection. The WSP guidelines were defined by the World Health Organization and were subsequently implemented in a European Directive and Italian legislation.

The study area represents an important source of drinking water supply for the Treviso province and has an extension of around 900 km^2. It is delimited to the northeast by the Piave river, to the west side by a flow line approximately parallel to the Brenta river, while the southern boundary is closed by the *Risorgive* area, and the north boundary by the Montello and colli Asolani. The north part is characterized by an undifferentiated aquifer, while the southern part hosts a multilayer system with 8 confined aquifers.

The thesis, after an introduction on the main scientific issues, starts with a description of the work done to reproduce in CATHY (CATchment Hydrology model) a previous model built using the software FeFlow. Before the calibration step, the initial mesh that hosts the multilayer systems of 8 aquitards and 8 aquifers was cut at the bottom of the first unconfined aquifer. This allowed the calibration to be sped up and for focusing on the unconfined aquifer, which is directly influenced by the atmospheric boundary conditions and subject to recharge variability. The calibration was performed by alternating FePEST and CATHY (through the Shuffled Complex Evolution algorithm). Both the bottom of the unconfined aquifer and the hydraulic conductivity field were calibrated. The calibration resulted in the root mean square errors being reduced to 1/3 compared to the uncalibrated model. Once the calibrated model was obtained, a validation step was also performed. The resulting model allowed us to investigate a scenario of changed irrigation management, planned in compliance with the European directive indications, to decrease water withdrawals from the Piave River and preserve its ecological flow. Currently, a large area of the domain is irrigated by the flood method, which is considered no more sustainable, due to large losses to infiltration. However, infiltration can represent an important source of good quality groundwater recharge. The scenario considered a switch to sprinkler irrigation only. The results show a local decrease in groundwater head, in wells located in the area affected by the conversion of the irrigation technique. This was confirmed by the difference in total cumulative recharge in the whole domain between the case of flood and sprinkler irrigation and sprinkler only irrigation. The model does not seem to be particularly affected by irrigation variations, but is more sensitive to hydraulic conductivity, the largest fraction of recharge occurring where hydraulic conductivity is higher.

A study on the analysis of solute transport numerical dispersion affecting the CATHY model was also carried out, in view of possible future applications of the model to contamination problems. This analysis allowed us to establish a criterion for the Péclet number (Pe) more restrictive than the traditional condition of $Pe < 2$ coming from the theoretical analysis of a linear convective-diffusive problem solved by a standard FD or FEM scheme. This study will be useful for future simulations on vulnerability to contaminations that require accurate solute transport modeling.

Overall, this thesis resulted in the development of an integrated surface-subsurface model capable to reproduce groundwater dynamics and its drivers at an unprecedented scale. Although it can be improved, this model represents a useful tool to investigate possible responses of the considered hydrosystem to future land use and climate change.

1. Introduction

Groundwater accounts for almost 99% of the available liquid freshwater present on Earth and is the main source of drinking water and irrigation (*Xiong et al., 2022*). In pristine conditions, the high quality of groundwater is guaranteed by natural soil processes such as attenuation, retention, and adsorption of non-anthropogenic contaminants. Starting with the Industrial Revolution, disturbances in groundwater flow and quality began to occur at large scales (*Edmunds and Shand, 2008*). Since then, new pollutants, unsustainable aquifers exploitation and land use, and climate changes have led to the so-called global groundwater crisis (*Famiglietti, 2014*). While in industrialized countries clean and safe drinking water is often taken for granted, in the rest of the world it is unevenly distributed (*Gleick and Cooley, 2021*).

Water is too often seen as an infinite resource, and therefore too many human behaviors do not pay appropriate attention to this very precious resource. According to a WWF report on the world's water availability (https://www.worldwildlife.org/threats/water-scarcity), more than 1.1 billion people worldwide do not have access to water and at least 2.7 billion people find water scarce for at least one month of the year. *Mesfin and Arjen, 2016*, claim that the population affected by water scarcity would even be 70% of the entire world population, 4.3 billion of humans. The sanitation conditions of the water to which they have access are quite always inadequate and cause in a year 3.4 million deaths (*Osiemo et al., 2019*).

Climate change and unsustainable rates of consumption are worsening these issues. For instance, climate change affects drinkable water because higher temperatures lead to increased growth of new parasites and survival of bacteria (*Jeon et al., 2019*), while altered weather patterns and water cycles around the world are causing more frequent extreme events such as droughts and floods (*Richts et al., 2016; Mahlalela et al., 2019*), with associated reductions in groundwater recharge.

Sustainable management of aquifers relies on a delicate balance between input fluxes, i.e., snow, rainfall, losing rivers, and sometimes excess irrigation, and outputs fluxes, including withdrawals for economic, social and environmental development. This equilibrium, which in some cases took centuries to be achieved, can be easily upset by unsustainable human activities and extreme climate events that lead to year-by-year recharge variability (*Gumuła-Kawęcka et al. 2022*). If the amount of water extracted exceeds the amount of water replenishing the aquifer, the result is a groundwater depletion that can imply less drinking water supply, reduction in groundwater quality, problem of salinization, subsidence, and strong impacts on the environmental ecosystems (*Konikow and Kendy, 2005*). For this reason, there is a compelling need to carefully evaluate all the terms of the aquifer water balance, to ensure their sustainable management.

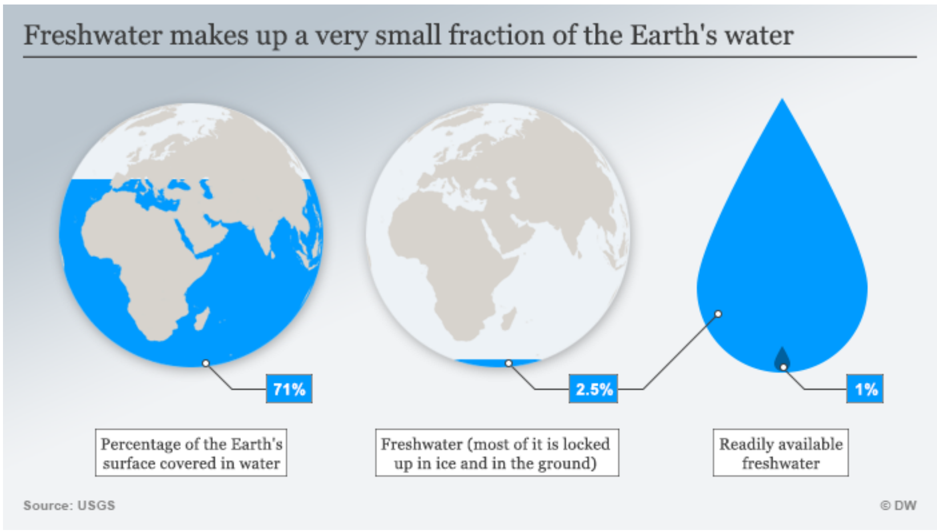

Figure 1: Fresh word water percentage (https://www.dw.com/en/are-we-running-out-of-fresh-water/a-40241057).

The first step taken by the United Nations to face these issues has been the definition of the *2030 Agenda for Sustainable Development,* then adopted by all member states of the United Nations in 2015. Agenda 2030 contains 17 actions that have been defined with the aim of improving human life conditions, both in developing and developed countries, and the health of the Earth within the year 2030. This is an ambitious project, but it needs to get started!

The sixth goal, *clean water and sanitation,* is related to the protection of water resources. On the official United Nations Organization website, it is possible to find the following explanation of the goal: "Ensure availability and sustainable management of water and sanitation for all". Tracking progress or worsening is kept continuously updated. Unfortunately, according to the water goal, there is no good news, this is what the report says: "In 2020, 129 countries and territories were not on track to meet the target of implementing integrated water resource management by 2030, including financing and intersectoral coordination mechanisms, basin management, and monitoring. The rate of implementation must double globally […]".

Figure 2: Sustainable development goals 2030.

For improving water management and quality, the two main sectors in which every member state could intervene are the industrial one, which is responsible for 20% of the global water withdrawal, and the agricultural one, which consumes around 70% of the water resource (*Mesfin and Winnie, 2020; Hossain 2019*). An increasing number of companies should track, manage and implement water solutions using the tools proposed by the existing regulation.

One of these tools is the Water Safety Plans (WSPs). WSPs constitute the most effective preventive model to ensure good water quality and consumer health protection, through integrated control measures extended to the entire water supply chain. Guidelines to be followed have been developed by the World Health Organization (WHO), which advocated the WSP approach since 2004 to ensure safe drinking water. Their implementation is required by European Union Directive 2015/1787, which substitutes the annexes of the European Drinking Water Directive 98/83/EC and requires the member states to implement the WSPs within 2025. Also, the new European Drinking Water Directive (Directive 2020/2184) mentions the WSPs and reflects the sixth goal of Agenda 2030 in requiring a risk-based approach with risk assessment and risk management (*Dettori et al., 2022*).

In Italy, the implementation of WSPs is required by the Decree of the Ministry of Health of 14.06.2017, in the implementation of the European Directive 2015/1787. The guidelines have been developed by *Istituto Superiore di Sanità*, in accordance with the WHO, and are aimed at water service managers, operators of the prevention departments of health agencies, regional environmental agencies, and other public bodies involved in the management and control of the drinking water supply chain (*Lucentini et al., 2021*).

On the official WHO website the key steps for effective water safety planning are presented (https://www.euro.who.int/en/health-topics/environment-and-health/water-and-sanitation/water-safety-plans).

The basis of WSPs is the risk assessment and risk management approach that involve all steps of the water supply chain, from the catchment to the consumer. Moreover, the WHO underlines how the “WSPs guide day-to-day system operation and with the aim to ensure the continued reliability and safety of the water supply” and they are adaptable to all types and sizes of water supply systems.

The steps that characterize a WSP are the following:

a) create a multidisciplinary team of local water supply stakeholders for the development and implementation of the WSP;
b) collect detailed and updated water system information, that must be verified in the field;
c) for the risk assessment approach, identify hazardous events that could affect water safety in the whole supply chain (introduction of chemical, physical and microbiological hazards, risk of extreme weather events, accidents, or malpractice in the vicinity of the supply);
d) evaluate the health risks associated with each hazardous event and plan the corresponding control measures;
e) plan actions and develop an improvement plan to address priority risks that are not controlled appropriately (revised control measures, upgrades to infrastructure and improved management procedures, etc.);

f) establish management procedures for normal operating conditions and incident situations;
g) provide monitoring of the control measures to assess their continuous effectiveness and allow timely action to limit any damage to public health and environmental ecosystems;
h) verify the effectiveness of the WSP through compliance monitoring and auditing;
i) perform periodic review of the WSP to keep it up to date, and if necessary, modify the WSP, taking into consideration lessons learned from shortcomings and unforeseen events that took place.

The WSP output is a 3D risk matrix (magnitude × risk × impact) that allows one to identify the areas with the highest priority of monitoring and intervention. Other information that is fundamental for the WSP realization can be obtained through the land use and the hydrogeologic charts: the recharge areas are the most vulnerable. The vast majority of freshwater available for drinking purposes comes from groundwater (*Freeze and Cherry, 1979*). The study area of interest in this thesis is no exception. From a qualitative point of view, one of the most important variables that must be considered is the type of contaminant that could reach the aquifer. The most common are As, Cr, Cu, Cd, Pb, Zn, F, polycyclic aromatic hydrocarbons (PAH), volatile organic compounds (VOCs), pesticides, and biological contaminants (*Al-Hashimi et al., 2021*). An aspect that should make us reflect is that of the 50000-100000 chemical agents used in western countries, only a few dozen are included in the lists relating to water safety and, for this reason, monitored (*Khorram-Manesh, 2015*). Moreover, in the last decades, emerging contaminants like pharmaceuticals and personal body products are increasing exponentially in the groundwater together with microplastics and nanoplastics. The latter, although smaller and therefore more problematic, are generally ignored due to the difficulty of measuring them (*Ebele et al., 2017; Ling et al., 2018; Al-Thawadi, 2020*).

The procedure described for the WSP realization is iterative and proactive and has the aim of continuous improvement, like the Deming cycle approach (*Reid et al., 2007*). For a complete and exhaustive tool application, WHO and the International Water Association (IWA) developed a WSP manual (*Bartram et al., 2009*) to guide local water supply stakeholders step by step.

This was an outline of the scientific problem that the WSPs would like to face. The theory must be translated into practice by water management companies.

The research presented here tries to contribute to the long WSP realization process that a water utility company in the northeast of Italy must perform in compliance with the European directives and Italian law. The thesis will focus on the scientifical aspects that the companies are expected to face in the WSP elaboration. The accurate definition of the protection areas of the extraction wells is one of that. To individuate these areas is necessary to have an adequate knowledge of the aquifers configuration to properly built a satisfactory numerical model that simulate more faithfully the real water behavior. Once built and validate this tool it will be possible to perform future scenarios simulations varying the input values of rainfall, irrigation, evapotranspiration or pumping wells extraction rate. The modification of the input values will translate in a different recharge for the aquifers and consequently a different water table distribution. Given the drought problems of the recent years in Italy (*Rossi et al., 2023*), the kind of problems to expect will be related to the decrease of groundwater, that will imply less drinking water supply, reduction in groundwater quality, problem of salinization, subsidence, and strong impacts on the environmental ecosystems.

For the WSP implementation, as it is possible to imagine, a huge amount of data, work, and time are required. A relevant role could be played by hydrological models, whose use is becoming a common practice and whose reliability in the assessment of present and future states of the watershed is at this point proven by several scientific publications. In this specific case, a numerical model of groundwater will be necessary, since groundwater represents the main mechanism of water supply in the study area.

As further explained in the next chapters, Veneto, the region that includes the area of study, is characterized by an agricultural tradition that has endured for centuries. Moreover, Veneto's drinking water needs are supplied almost totally with groundwater, withdrawn through pumping wells set in the strongly anthropized plain. The phreatic aquifer of the high and middle plain guarantees the aqueducts supply also of the lower plain. Hundred thousand wells withdraw per second more than 100 m^3 of water (DGR nr. 1621/2019). Areas in which water for human consumption is extracted, require particular attention and limitation of potential hazard activities. In Italy, the obligation for the wells protection area was already defined through the Lgs. D. n. 152/2006. From an integrated water management perspective, the multiple uses of water resources must be taken into consideration simultaneously: what happens on the surface influences what flows in the subsurface. The type of irrigation that has generally been used in these zones is flood irrigation: this requires large amounts of water, in the specific case taken from Piave river, which defines one of the boundaries of the study area. The same water withdrawal from one side constitutes the groundwater recharge in the other side. According to the new directives, this kind of irrigation is no more sustainable, and within some years must be converted into sprinkler irrigation, which would reduce the waste of this precious resource. The point is that this "waste" of water, in the venetian plain, coincides with an important fraction of groundwater recharge (*Dal Prà A., et al, 1996*; http://www.liferisorgive.it/en/partners/brenta-consortium-for-land-reclamation/). What consequences could be induced by upsetting this equilibrium, and reducing the recharge?

To investigate the interaction between surface water (rivers and irrigation) and subsurface water, an integrated surface-subsurface hydrological model (ISSHM) is here employed.

Some of the ISSHMs developed in the last years and commonly used are Process-Based Adaptive Watershed Simulator (PAWS; *Shen and Phanikumar, 2010*), CATchment Hydrology (*CATHY; Camporese et al., 2010*), HydroGeoSphere (HGS; *Brunner and Simmons 2012*), MIKE SHE (*Long et al., 2015*), and ParFlow (*Maxwell et al., 2015*). From a first literature analysis, it emerges that ISSHMs are rarely used in the practical-operational field as decision support tool by water utilities companies. They are used mainly to reproduce experimental data (*Pertti et al., 2017; Bizhanimanzar et al., 2020*; *Bizhanimanzar et al., 2019*), assessment of possible future scenarios after increasing or decreasing withdrawal (*Hossein and Kaveh, 2022*), simulation of contamination spreading (*Reszler and Fank, 2016; Gatel et al., 2019; Gatel et al., 2020*), but generally stop after the validation phase.

Some recent studies used HGS for purposes similar to the one presented in this thesis. *Haque et al., 2021*, presents the application of HydroGeoSphere to a Canadian groundwater system to investigate the impacts caused by water use, different withdrawal scenarios, and climate changes. The model application has a clear aim: the results obtained by the ISSHM will be used to "support the development of a sustainable water management plan", as mentioned in the article.

A second paper, *Surinaidu 2022*, investigated the stream flow and the groundwater response of an Indian river basin that supplies water to millions of people. The rapid urbanization of the area and the increase in agricultural pressures modified the hydrological equilibrium, reducing the storage of groundwater. Also, in this case, hydrological modeling is proposed as a support for sustainable water resources management.

The simulation of contaminants transport is another important aspect of ISSHMs. This is hugely important in relation to the water quality issues mentioned above that are the real objectives of the WSP application. Once the contaminant source is identified, it is important to have a clear understanding of the area interested by the pollution and the timing of the solute spreading. The regional scale of application of the present case study, on the order of magnitude of 1000 km^2, requires particular attention to the numerical errors that may affect the hydrological model results. This kind of error tends to overpredict the spreading of the contaminant, as the numerical dispersion error is added to the contaminant physical dispersion, with the consequential pollutant plume overestimation. For these reasons part of the work has been reserved to the model numerical dispersion error analysis and to the research of a criterion for the error containment.

In summary, given all these aspects, the general objective of the thesis is to make a first step towards the implementation of an integrated surface–subsurface hydrological model, CATchment Hydrology (*Camporese et al., 2010*), for practical management purposes in support of the water utility company *Alto Trevigiano Servizi* (ATS). To reach this aim and obtain a reliable decision support tool, some of the main scientific issues to be faced are related to the definition of the aquifers configuration, the characterization of the permeability distribution of the study area, the collection of the observed water level of the wells present in the domain, the definition of the atmospheric, initial and boundary conditions. Once elaborated the information and hydrogeologically characterized the study area, the calibration and validation of the model will be further necessary steps. The model thus built will be able to realistically quantify the current groundwater recharge and will give responses of the irrigation variation scenarios prescribed by the European Directives.

The work presented here is subdivided as follows. The chapter which comes after the introduction describes geographically and hydrogeologically the area of interest and includes a focus on the Italian law about the wells protection area and their definition criteria. A brief descriptive historical digression introduces the different irrigation techniques that constitute a focal point in the European Water Framework Directive in terms of water saving. However, water saving can lead to groundwater disequilibrium in areas where irrigation and aquifer recharge are strictly connected, as happens in the Veneto region.

The third chapter contains the CATHY model description and the model setup. Different domain mesh and boundary conditions configurations are presented, before the final one that leads to model setup that better reproduces the real available data. The water level observations were provided by the water utility companies whose wells fall within the study area.

The fourth chapter introduces two calibration algorithms employed: PEST (Parameter ESTimation), a non-linear inverse modeling code developed by John Doherty (Doherty, 2015) and SCE-UA (Shuffled Complex Evolution – University of Arizona), a global optimization method (*Duan et al., 1994*). PEST is applied through the use of FeFlow (Finite Element subsurface FLOW system), an advanced finite-element subsurface flow and transport modeling system. In this code PEST is already implemented (FePEST) and allows the user to obtain a calibrated heterogeneous field of hydraulic conductivity thanks to the pilot points method, not yet available in CATHY. After the FePEST calibration, a SCE-UA algorithm calibration will be performed with CATHY to refine the previously obtained parameters. Also in this case different trials were carried out before the best solution that consists of a "dialogue" with the FeFlow code. After the calibration, the model was validated and used to investigate a scenario of variation in irrigation management.

The fifth chapter consists of a detailed investigation of numerical dispersion in CATHY simulations of solute transport. This study, as mentioned above, is relevant for solute transport analysis, in order not to confuse numerical dispersion with physical dispersion.

The sixth chapter presents the overall conclusion of the Ph. D project work.

The Appendix constitutes the CATHY user guide.

2. The study area

The research activity I carried out during these three years is the continuation of the PhD thesis by Tommaso Trentin (*Trentin 2020*). The objective of his thesis was the realization of a model suitable as decision support tool for the managers of water resource in the Veneto region in the north-east of Italy. The present study represents a further step in the realization and the refinement of the decision support tool useful for the water utility company in the Water Safety Plans implementation.
As the title suggests, the area of study is delimited in the north-east by the Piave river, the west side is parallel to the Brenta river, the southern part includes the *risorgive* area -an artesian zone, from which the Sile river rises-, while in the Northern area, *Montello hill* and *Colli Asolani* close the domain. Its extension is around 900 km^2 (*Figure 3)*.

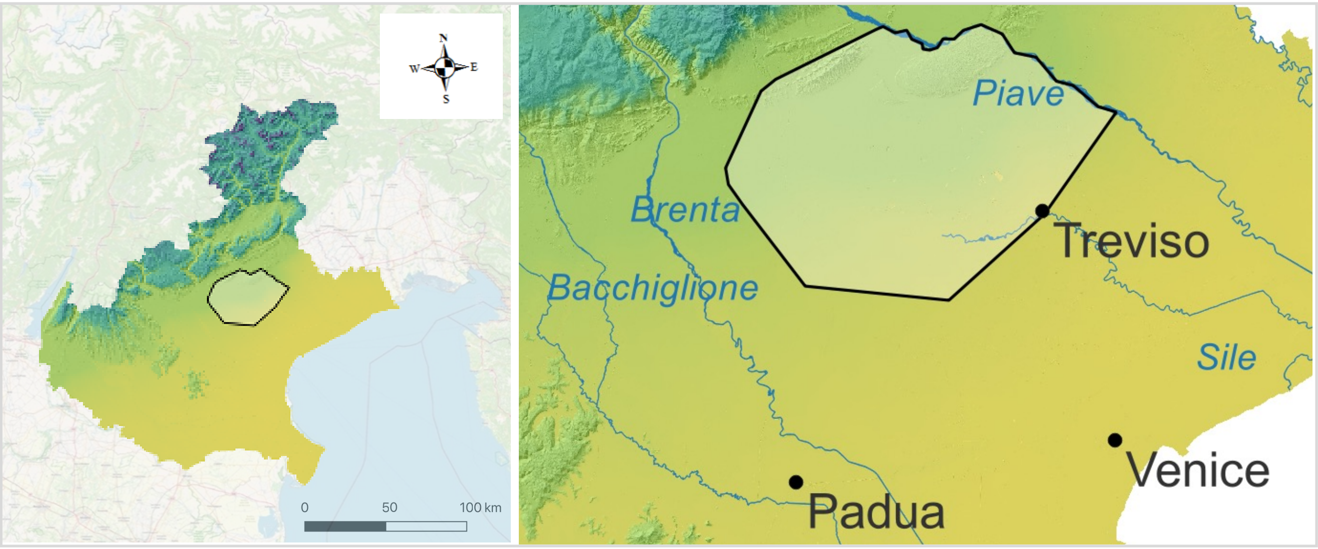

Figure 3: Veneto Region and study area position.

The hydrogeological structure of the Venetian plain is known since the '70s, thanks to deep studies performed by the Italian institution, Consiglio Nazionale delle Ricerche (CNR) (*IRSA-CNR, Gruppo di studio sulle falde acquifere profonde della pianura Padana, 1976*). The Venetian alluvial plain, that goes from the mountain to the sea, can be subdivided in three strips:

- *high plain strip*, also called *piedmont zone*, close to the mountainous area in the north-west of the region
- *middle plain strip,* also called *risorgive belt*, is positioned approximatively at the half of the red domain. This band subdivides the high and the low plain
- *low plain strip,* is nearby the sea.

The underground material from piedmont zone to *risorgive* belt is mainly constituted by granular material (gravel and sand) that forms a sort of natural "reservoir", whose thickness is hundred meters. This groundwater reservoir hosts a homogenous phreatic aquifer, that flow from the mountain (NW) to the sea (SE), with a mean velocity of order of magnitude of meters per day.

Figure 4: Sile river spring.

In the *risorgive* belt, part of the water of the unconfined aquifer exfiltrates, giving rise to groundwater-fed streams, the most significant being the Sile, whose spring is located in Casacorba, Treviso (*Figure 4*). Another part feeds the deep aquifers, constituted by granular materials, that become finer proceeding in the sea direction. In this part of the plain the aquifers are confined: the water is under pressure, and they are separated from each other by relatively impermeable layers. The recharge of the artesian aquifers occurs mainly due to irrigation infiltration and rainfall, in the piedmont area.

The subsurface of the low plain is characterized by a multilayer system of 8 confined aquifers. They are artesian, separated from each other by clayey and silty aquitards. This aquifer system is fed by the unconfined aquifer of the high plain. An unconfined aquifer is present in the shallow part of the low plain, but it is discontinuous, and with variable hydraulic conductivity. *Figure 4* shows a graphical schematization of the venetian hydrogeological structure section.

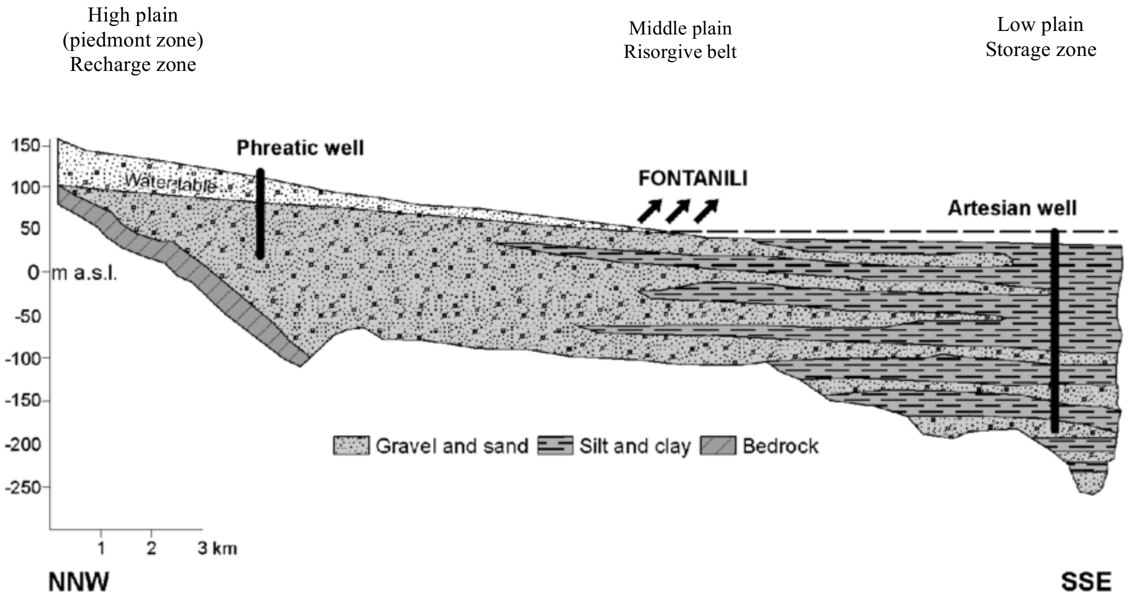

Figure 5: Venetian plain hydrogeological structure. Image taken from Piccinini et al., 2017.

The knowledge of this structure is important, among several other reasons, also for an efficient groundwater resources use management, which should be done by the water utility companies of the territory.

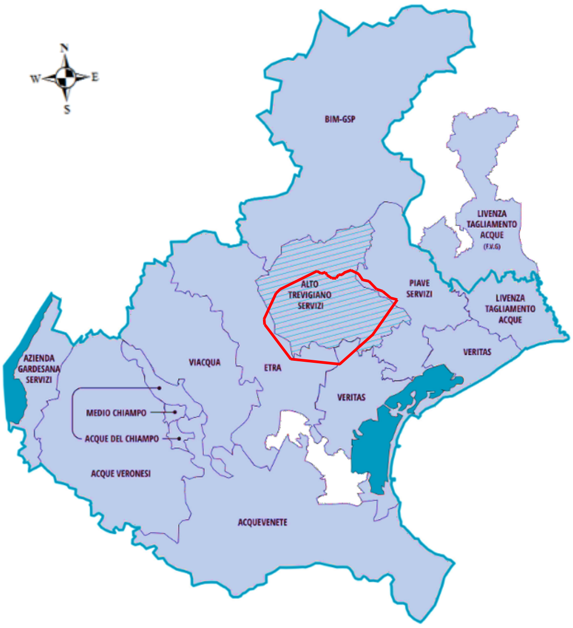

Figure 6: Veneto Region Water utility companies
https://altotrevigianoservizi.it/p/ats/chi-siamo.

Alto Trevigiano Servizi is a water utility company that manages the integrated water service of 52 municipalities, serving more than 500000 people in a territorial basin of 1374 km^2. Some of the municipalities are included in the study area. This company covers almost the whole domain of interest, as shown in *Figure 5.*

The company is required to implement the Water Safety Plans within 2025, as required by European Union Directive 2015/1787, to ensure good water quality, and the consumers health protection. To do that it will be useful to dispose of a hydrological model for the flow and transport simulation, in support for the decisions to be taken in the definition of the wells protection areas.

Besides ATS, also ETRA, VERITAS, ARPAV and SAN BENEDETTO (the last two are not present in the list of *Figure 5*) manage part of the water resources of the area of study, and they kindly provided some of the wells data, necessary for the realization of the model. The data collected are mainly related to the position of the wells, the withdrawn discharge from the pumping wells, the screening wells elevation and the time series water table position.

Other data used for the model building are rainfall, evapo-transpiration and irrigation, useful for the evaluation of the atmospheric boundary conditions. The rainfall data were downloaded from Agenzia Regionale per la Prevenzione e protezione Ambientale del Veneto (ARPAV) site. The evapotranspiration coefficients were evaluated using the Penman-Monteith equation, based on the soil use indicated by “Carta di copertura del suolo” of Veneto Region (2012).

Irrigation data were provided by *Consorzio di Bonifica Piave*. Particular attention will be paid on the irrigation since it is a variable that can be controlled, and it strongly affects the groundwater recharge.

The Water Framework Directive 2000/60/CE, implemented in Italy through the Deflussi Ecologici Decree 30/2017 (Decreto del Ministero dell’Ambiente e della Tutela e del Territorio e del Mare) aims to balance three important elements: i) the achievement of the good state of water bodies, ii) the continuous demand of water for civil and industrial uses and iii) the decrease in availability of water resources because of climate changes. This has however some problematic points that we will analyze later.

Veneto region, in compliance to this decree, and in particular the area of managed by *Consorzio di Bonifica Piave,* has planned a change on the irrigation techniques, moving from flood irrigation to sprinkler irrigation. Currently the irrigation interests 500km^2 of land, i.e., almost the 55 % of the area of study. One half of the area is irrigated through flood technique, the other half through sprinkler irrigation. The amount of water used is more or less 1.85 $\frac{l}{s*ha}$ and 0.60 $\frac{l}{s*ha}$ respectively. This switch will allow saving more to 50% of the water, in the areas where flood irrigation is currently used, in compliance with the withdrawal limits from rivers provided for by the Directive on Ecological Drain.

2.1 Irrigation practices and groundwater recharge

The irrigation practice is a 10000-years-old story. Archaeological findings confirm that already around 8000 BC, in Mesopotamia, irrigation systems were built to bring the waters of the Tigris and Euphrates few kilometers away from the rivers for the irrigation of plain for productive aims.

In Italy the Etruscans started the first important irrigation works along the Po valley, but the Romans were the real architects of the birth of a water and irrigation system: a network of canals and aqueducts carried water for tens of kilometers from the springs to the big cities and agricultural areas.

Their engineering skills spread not only throughout Italy, but also on the Mediterranean coasts, where large interior areas were made fertile (*Treccani encyclopedia*).

At the end of the XVIII century, the hydraulic and irrigation techniques started by the Romans reached a very high degree of technical performance. The water system structures have become more and more sophisticated over the centuries, and allowed the progressive development of the agricultural activities in Italy. The new hydraulic knowledge also allowed the Po valley to be reclaimed.

Until a thousand years ago this area could not be defined as a favorable environment for development: the land was inhospitable, swampy, full of woods and ponds. The cultivable areas were only those that bordered the Po River. After an incessant reclamation hydraulic work, that lasted for centuries, the Po Valley is nowadays one of the most productive environments in Italy: its territory offers resources and work for multiple activities (*Consorzio di Bonifica Bacchiglione, La storia*). The agriculture practiced is intensive, and in the low plain alone a big part of the agricultural products of Italy is produced (ISTAT, 2018).

After 10000 years, irrigation has remained an essential element for economic development, and today has also to face sustainability issues. The more popular irrigation techniques can be subdivided in four typologies.

1) *Irrigation by submersion*. Fields are completely submerged by water for a defined period. The water is introduced through channels or piping, and it is contained thanks to small embankments. This technique in not suitable for all the vegetation types, and it requires big amount of water, not always available.

Figure 7: Submersion irrigation.

2) *Flood irrigation*. The canalization network brings the water through channels or piping, and directly introduced it over the land surface, where it flows homogeneously thanks to an artificial slight slope, exploiting the gravity force. This technique beside being energetically convenient, also favors the groundwater recharge, but also in this case a large amount of water is employed.

Figure 8: Flood irrigation.

3) *Sprinkler irrigation*. Water is supplied to the vegetation through high pressure sprinklers, that allows for breaking the water jets into many droplets increasing the efficacy of the flow. In this way less amount of water is needed. This technique, beside wetting the land, can provide thermoregulatory, anti-frost, anti-parasitic and fertilizer functions.

Figure 9: Sprinkler irrigation.

4) *Drip irrigation* (*localized*). Small water quantities are supplied continuously, or during defined intervals, nearby the vegetation roots with a small pressure. The advantages are related to the meager amount of water use and in the better crops yield. Limitations can be found in the high installation and maintenance costs, because of the tendency of the pipes to clog. In the Po Valley, this irrigation system is not diffused.

Figure 10: Drip irrigation.

As already mentioned, in the area of study the techniques applied for irrigation are *flood* and *sprinkler*. For sustainability reasons, within a few years a planned switch to network under pressure will be carried out, to save water in accordance with the Deflussi Ecologici Decree 30/2017.

In June 2021 an article with worried tones has been published by an online provincial newspaper, TrevisoToday. Consorzio di Bonifica Piave and Enel Green Power, a reclamation consortium and an Italian energy company, respectively, referring to alarming data provided by their experimental study, state that an indiscriminate application of the decree will dramatically reduce water accumulations in mountain basins with serious repercussions for agriculture, the environment, the landscape and hydroelectric energy production. The study, presented on 4th June 2021 at Festival della Bonifica in San Donà di Piave, highlights the potentially critical points of the European Directive application, if the peculiarity of the territories and the complex interconnections of water networks are underestimated. The Nervesa della Battaglia hydraulic intake work was presented as an example: according to the two Institutions, the variation in release water volume imposed by the regulation will strongly and negatively impact the waterways network which innervates the Treviso province.

The president of Associazione Nazionale dei Consorzi per la Gestione e la Tutela del Territorio e delle Acque Irrigue (ANBI), waiting for a fruitful dialogue with Europe regarding the application and the rediscussion of the Ecological Drain Directive, proposed to suspend the irrigation technique switching: this would allow for reducing the impacts of water reduction availability on the rivers, biodiversity and ecosystems. A compensatory measure to limit the expected impacts in case of water reduction use, could be the allocation of the disused quarries to water collection basins.

Figure 11: Nervesa della Battaglia hydraulic intake work.

As underlined by the study carried out by Consorzio di Bonifica Piave and Enel Green Power, carefulness must be taken in the application of water balance modification not only in the Veneto region, but also in all the areas affected by the directive. The delicate equilibrium that in hundreds of years was created among the water and the ecosystems has to be considered in terms of sustainability, but without forgetting that the protection of biodiversity is part of the sustainability too. It will be necessary to provide the introduction of the water saving measure progressively, allowing also the nature to get used to the new regime, including groundwater recharge.

Groundwater recharge via leached irrigation water can be significant (*Sen, 2015*). Thus, groundwater decline or depletion is what could happen due to the reduction of groundwater recharge. This aspect is generally attributed to the extreme climate change and droughts, or to an excessive and unsustainable exploitation of the groundwater aquifer… but can it be related to sudden irrigation decrease too?

Some of the *serious repercussions* to which this study refers are related to lowering of the water table, land subsidence and deterioration of water quality.

In the first case, if groundwater levels decline too far, it could be necessary to deepen the wells, drill new ones, or attempt to lower the pump. The decline of the water level can also lead to a reduction in the water well rate.

The phenomenon of subsidence consists in the loss of ground support, related to the lowering of the ground level. Part of this support is furnished by the presence of the water in the soil, that fills its pores. If water is removed, the soil compacts and lowers, or even collapses.

The inflows reduction will unavoidably lead to a decreasing of the amount of water that infiltrates in the basin, with possible impact, beside on the water quantity, also on the water quality, because fixing the load of the contaminants, and decreasing the solvent amount, the concentration increases, and this can a problem in terms of water potabilization. Also the saltwater intrusion could be a problem to face nearby the coasts: this is generally linked to the sea level increase, but a lowering in the water table will cause similar issues (*Groundwater Decline and Depletion, 2018*).

3. Model description and setup

My research activity, focused on the aquifer system in the Venetian plain between the Brenta and Piave rivers, has begun with the reproduction in CATHY (CATchment Hydrology) of the model that Trentin built using the software FEFLOW (Finite Element subsurface FLOW system).

FEFLOW (*Diersch, 2013*) is an advanced finite-element subsurface flow and transport modeling system with functionalities that go from variably saturated flow to variable fluid density mass and heat transport, up to multispecies reactive transport, accessible via a comprehensive user interface. It is a proprietary code and not freely available. The program has been under development since 1979 by the Institute for Water Resources Planning and Systems Research Inc (*Trefry et at., 2007*).

CATHY is an open-source research code, written in Fortran, developed originally by C. Paniconi, University of Quebec and M. Putti, University of Padova in 1993, and on which many others have subsequently contributed. It is a physically based model that simulates the overland and the subsurface flow by coupling a finite element solver for the 3-D Richards equation for variably saturated porous media (1) with a finite difference solver of the 1-D diffusive wave equation for the surface flow (2) (*Camporese et al., 2010*; *Weill et al., 2011*; *Scudeler et al., 2016b*).

$$S_w S_s \frac{\partial \boldsymbol{\psi}}{\partial t} + \phi \frac{\partial S_w}{\partial t} = \vec{\nabla} \cdot \left[\boldsymbol{K_s} K_r\left(\vec{\nabla}\psi + \vec{\boldsymbol{\eta}}_{\boldsymbol{z}}\right)\right] + q_{ss} \qquad (1)$$

$$\frac{\partial Q}{\partial t} + c_k \frac{\partial Q}{\partial s} = D_h \frac{\partial^2 Q}{\partial s^2} + c_k q_s \qquad (2)$$

In equation (1), $S_w = \theta / \theta_s$ is the water saturation [/], θ being the volumetric moisture content [/] and θ_s the saturated moisture content (generally equal to the porosity ϕ) [/], S_s is the aquifer specific storage [L^{-1}], ψ is the pressure head [L], t is time [T], $\vec{\nabla}$ is the gradient operator [L^{-1}], K_s is the tensor of saturated hydraulic conductivity [LT^{-1}], $K_r(\psi)$ is the relative hydraulic conductivity [/], $\vec{\eta}_z$ = $(0,0,1)^T$, z being the vertical coordinate directed upward [L], and q_{ss} is a source (positive) or sink (negative) term [L^{3}L^{-3}T^{-1}] that generally represents exchange fluxes from the surface to the subsurface. In equation (2), s is the longitudinal coordinate system used to describe the overland/channel network [L], Q is the surface discharge [L^{3}T^{-1}], c_k is the kinematic celerity [LT^{-1}], D_h is the hydraulic diffusivity [L^{2}T^{-1}], and q_s is the inflow (positive) or outflow (negative) exchange rate from the subsurface to the surface [L^{3}L^{-1}T^{-1}].

Consistent with the flow module, solute transport in CATHY is modeled with a three-dimensional advection–dispersion equation and a one-dimensional advection–diffusion equation for the subsurface and the surface, respectively:

$$\frac{\partial \theta \boldsymbol{C}}{\partial t} = \vec{\nabla} \cdot \left(-\vec{\boldsymbol{U}} C + \boldsymbol{D} \vec{\nabla} C\right) + q_{tss} \qquad (3)$$

$$\frac{\partial Q_m}{\partial t} + c_t \frac{\partial Q_m}{\partial s} = D_c \frac{\partial^2 Q_m}{\partial s^2} + c_t q_{ts} \qquad (4)$$

where *C* $[ML^{-3}]$ is the solute concentration, $\vec{\boldsymbol{U}}$ $[LT^{-1}]$ is the Darcy velocity vector, $\boldsymbol{D}$ $[L^2T^{-1}]$ is the tensor that accounts for mechanical dispersion and molecular diffusion, q_{tss} $[ML^{-3}T^{-1}]$ is a solute mass source (positive) or sink (negative) term, Q_m $[MT^{-1}]$ is the solute mass discharge, c_t $[LT^{-1}]$ is the kinematic solute celerity, D_c $[L^2T^{-1}]$ is the surface solute diffusivity, and q_{ts} $[ML^{-1}T]$ is the solute mass inflow (positive) or outflow (negative) exchange rate from the subsurface to the surface.

A brief overview of the CATHY features more relevant to this research is now given.

Coupling between the surface and subsurface modules rely on a B*oundary Condition Switching* procedure, which is based on two thresholds of soil water pressure head, one, h_{min} [m], for the partitioning of rainfall into infiltration and surface runoff and another, ψ_{min} [m], to distinguish between atmosphere-controlled and soil-limited evapotranspiration. The latter, in particular, allows for a simple conversion of potential evapotranspiration into actual evapotranspiration. When the pressure head at the soil surface is larger than ψ_{min} the condition prescribed is flux, a Neumann condition and this flux coincides with the potential evapotraspiration rate, this is the case of atmosphere-controlled evapotranspiration. When the pressure head at the soil surface is equal to or less than ψ_{min} the condition prescribed from a flux becomes a constant value of pressure head, that coincides with the threshold ψ_{min} and the evaporation rate is back-calculated by the solver based on the solution and it is soil limited (*Camporese et al., 2015*). The choice of a proper value of ψ_{min} allows users to account in a simple and effective way for the impacts of shallow rooted vegetation on the catchment hydrological response (*Camporese et al., 2014*).

Another method, based on the root water uptake approach by Feddes, can be used to compute actual evapotranspiration in CATHY. The water removed from the soil by the vegetation roots is represented as a sink term q_{ss} in equation (1) and it depends on the potential transpiration, water content and root depth and density (*Muma et al., 2013*). The root density $\beta(z)$ is distributed along the depth as follow:

$$\beta(z) = \left[1 - \frac{z}{z_m}\right] e^{-\frac{p_z}{z_m} z} \qquad (5)$$

where z is depth (i.e., positive downward), z_m is the maximum rooting depth, and p_z is an empirical parameter (*Camporese et al., 2015*). The effect of soil moisture θ is modeled through the multiplication of the potential root water uptake and the Feddes reduction function (*Feddes et al., 1976*). The Feddes reduction function is a piecewise linear function that describes a root water uptake reduction factor, α(θ) that goes from 0 to 1. Five stages of water uptake are described bounded by four values of soil moisture ($\theta_s > \theta_{an} > \theta_d > \theta_{wp} > 0$). The Feddes reduction function is zero at saturation θ_s, this is a phase of complete aeration deficiency and null water uptake (anoxic phase). Decreasing the value of soil moisture between θ_s and θ_{an} the hypoxic phase took place, and the root water uptake increases linearly as air-filled porosity increases. In the range between θ_{an} and θ_d (constant rate phase), there is no water stress or aeration stress and the root water uptake equals the potential root water uptake. Between θ_d and θ_{wp} (falling rate phase), water uptake decreases linearly to zero. Below θ_{wp},, delimiting the permanent wilting phase, the root water uptake equals zero (*Camporese et al., 2015*; *de Melo et de Jong van Lier, 2021*). It should be noted that in CATHY the Feddes water stress function is implemented as a function of pressure head instead of soil moisture.

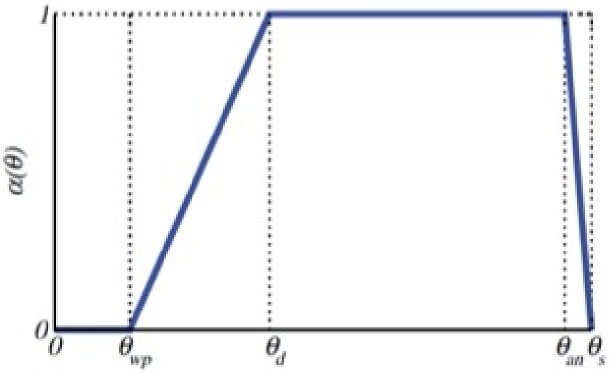

Figure 12: Feddes reduction function of root water uptake. In the horizontal axis the soil moisture is reported. Figure taken from Camporese et al., 2015.

In CATHY, the *van Genuchten soil water retention curve function* has been implemented to model the unsaturated soil. The equations were proposed by Van Genuchten in 1980 with the following expressions:

$$K_r = \left[\theta^{1/2} \int_0^{\theta} \frac{1}{h\,(x)}\, dx \Big/ \int_0^{1} \frac{1}{h\,(x)}\, dx \right]^2 \quad (6)$$

$$\theta = \theta_r + \frac{\theta_s - \theta_r}{[1 + |\alpha\, h|^n]^m} \qquad (7)$$

where θ is the soil water content ($cm^3 \cdot c\ m^{-3}$), θ_r is the soil residual water content ($cm^3 \cdot cm^{-3}$), θ_s is the soil saturated water content ($cm^3 \cdot cm^{-3}$), ψ is soil water potential (m), α is a scale parameter inversely proportional to mean pore diameter (cm^{-1}), n and m are the shape parameters of soil water characteristics with $m = (1 - 1/n)$ and $1 < n < 6$. Equation (6) allows to well predict the unsaturated hydraulic conductivity knowing the water retention curves parameters of the soils and the conductivity at saturation (*Van Genuchten 1980*; *Yang and You, 2013*).

The input values imposed in the model were obtained from *Carsel and Parrish 1988*.

In *Figure 13* some examples of retention curves are shown.

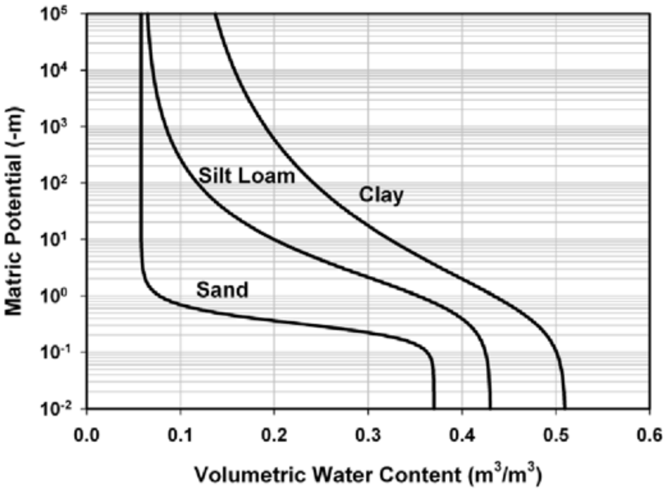

Figure 13: Example curve of the relationship between water content and matrix tension for different soils. Figure taken from Levizzari 2017.

The *time-splitting technique* is the algorithm implemented in CATHY for the solution of the solute transport in the subsurface. Advection is solved on the elements through a finite volume solver, while dispersion is solved on the nodes by means of a finite element scheme. This algorithm makes the solver numerically robust and computationally efficient. This can be obtained adapting the time step size to the local Courant–Friedrichs–Lewy (CFL) constraint. If taken alone the schemes are stable, but when advection and dispersion are coupled together, the continuous exchange of information between elements and nodes, through a linear interpolation, gives rise to a particular form of numerical dispersion (*Mazzia et al., 2000; Mazzia and Putti, 2005*) that has been analyzed and quantified. The results will be presented in the following chapters.
The reasons why we decided to move from FeFlow to CATHY are multifold:

- CATHY, differently to FEFLOW is an open-source code,
- in FEFLOW the recharge of the aquifers must be imposed as a boundary condition, while CATHY computes it internally based on the model solution,
- in CATHY is possible to integrate whatever automatic calibration algorithm, while with FeFlow the only possibility is to use PEST (*Doherty, 2015*), already implemented,
- CATHY is able to partition fluxes at the soil surface (rainfall, potential evapotranspiration) into infiltration (and eventually recharge), surface runoff, and actual evapotranspiration.

Overall, also based on the previous work by *Trentin (2021)*, the following modeling steps were performed in this thesis:

1. Definition of the problem
2. Conceptual model
3. Construction of the numerical model
4. Model calibration

A novel and further step of this research project is the simulation of future scenarios with irrigation management variations. The compliance with the European directives will impact the aquifers recharge both in term of quantity and in terms of quality, and this study try to assess these changes, which represent not only important information for the funder Alto Trevigiano Servizi, but also a relevant scientific question.

In the model building process, many configurations where realized. Different degrees of complexity were considered: number of layers, number of surface nodes, wells discretization. A first configuration was implemented in CATHY, as starting point, but then, after some trials and errors, a more suitable one was found, which could take into account in a proper way the spatial distribution of the hydraulic conductivity, as will be described in the following.

3.1 First model configuration

3.1.1 Mesh

The building of the model in CATHY started with the import of the 3D mesh from FeFlow. The initial mesh had 24 layers, each one a parallel replicate of the surface DEM layer that has 7793 nodes, for a total number of 187032 nodes (*Figure 14*). In *Figure 14* the elevation is exaggerated by a factor of 10: the lowest point elevation corresponds to -400 m, while the highest one is around 455 m, corresponding to the south *risorgive* area and Montello hill (the yellow area in the north-west).
The position of the wells is underlined by the finer discretization. The wells present in the area are approximately 300 and they belong to different agencies: ARPAV, ATS, ETRA, VERITAS, SAN BENEDETTO as already mentioned.

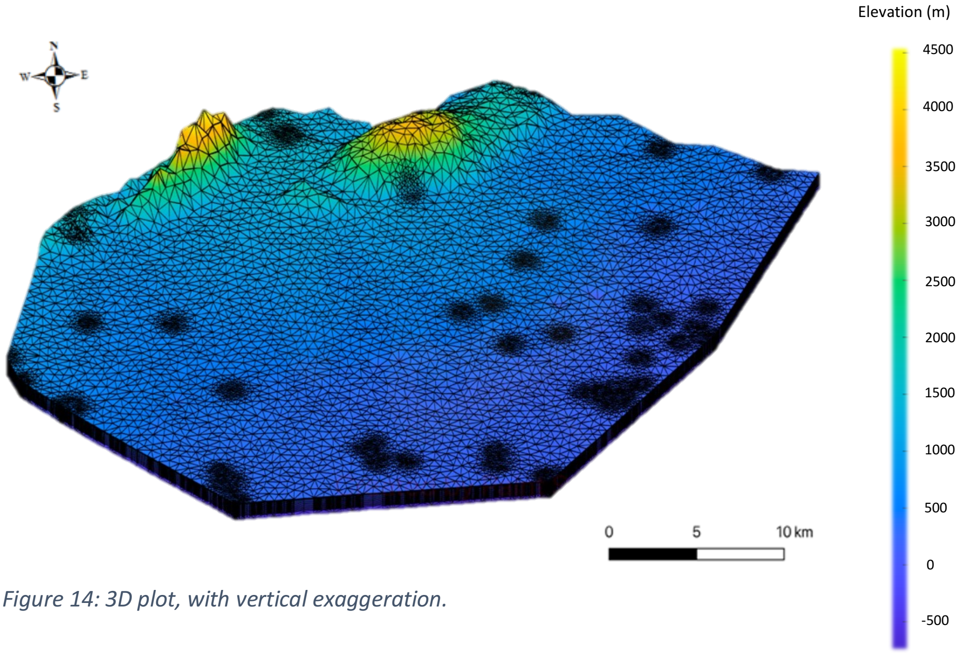

Figure 14: 3D plot, with vertical exaggeration.

3.1.2 Boundary conditions and initial conditions

After having implemented the 3D mesh in CATHY, the following step was the imposition of the Dirichlet and the Neumann boundary conditions. The Neumann boundary conditions are represented by the time series of the pumping wells, that extract water from the aquifers. The information available are daily data referred to years 2018 and 2019. The flow rate varies from well to well, with values that goes from 2.0^{-6} m^3/s to 4.30^{-2} m^3/s. In *Figure 16* an example of time series pumping flow rates, well ID 82026, 83003 and 84008 belonging respectively to the water utility company ATS, ETRA and VERITAS.

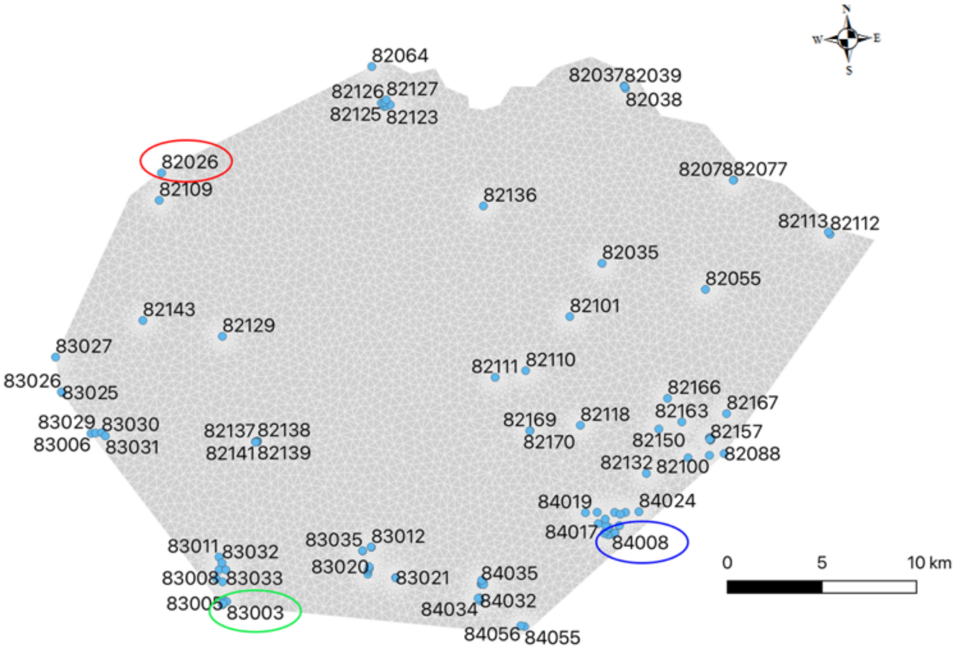

Figure 15: Surface nodes interested by the Neumann condition.

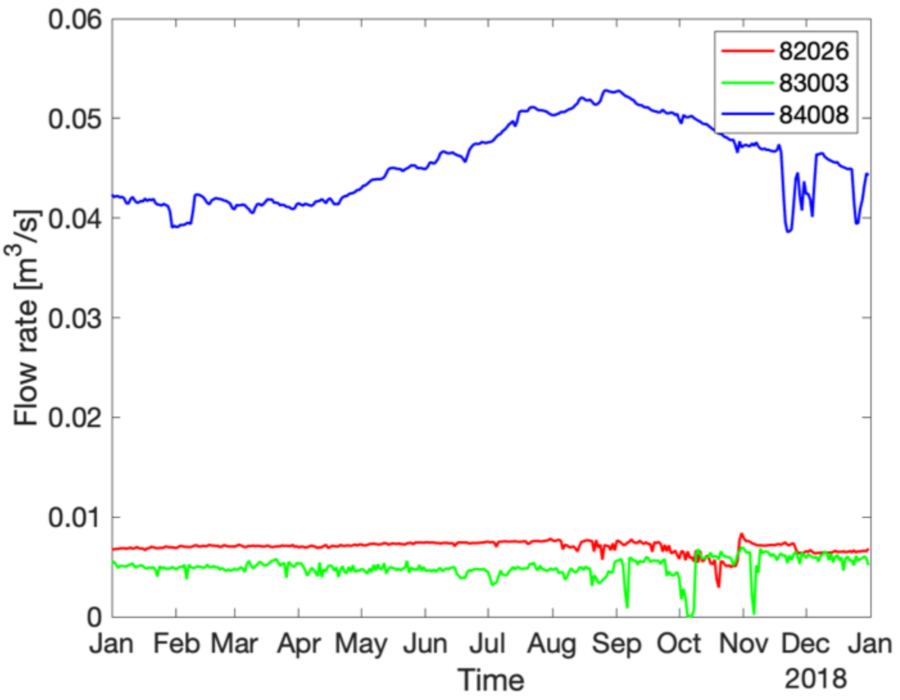

Figure 16: Example of pumping flow rate time series (wells 82026, 83003, 84008).

The lateral boundary conditions vary in time and along the perimeter of the domain.

In the first two layers of the domain:

- in the north, east and west, a phreatic boundary condition was imposed,
- in the southern part, corresponding to the *risorgive* area, a no flow boundary condition was imposed, due to the poor permeability of the shallow soils (*Figure 17*).

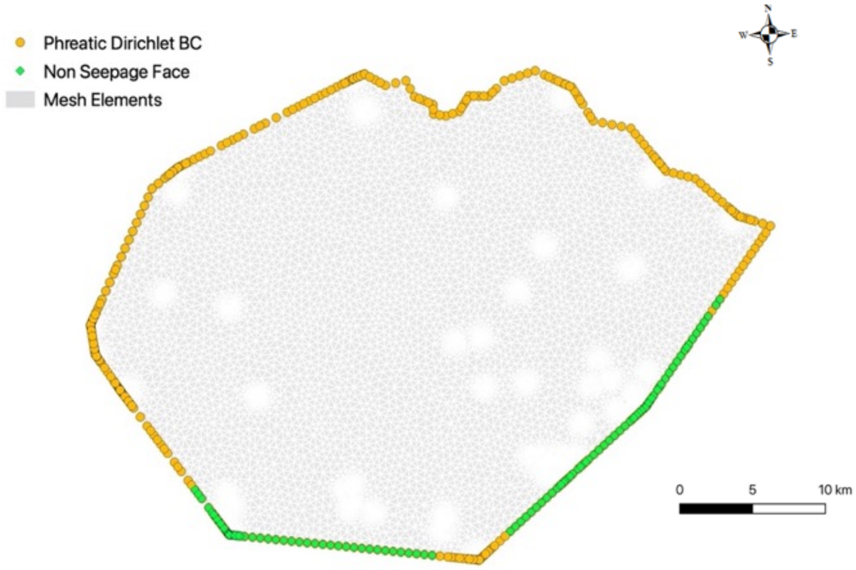

Figure 17: Boundary conditions in the nodes of the first and second slices.

In the deeper layers:

- in the north-east there is a no-flow boundary condition, because of symmetry under the Piave river,
- in the north-west and in the south-east sides, Dirichlet boundary conditions were imposed based on water table observations,
- in the south-west there is a no-flow boundary condition, because of the flow is assumed parallel to Brenta river,
- no-flow boundary conditions were also imposed at the bottom of the computational domain.

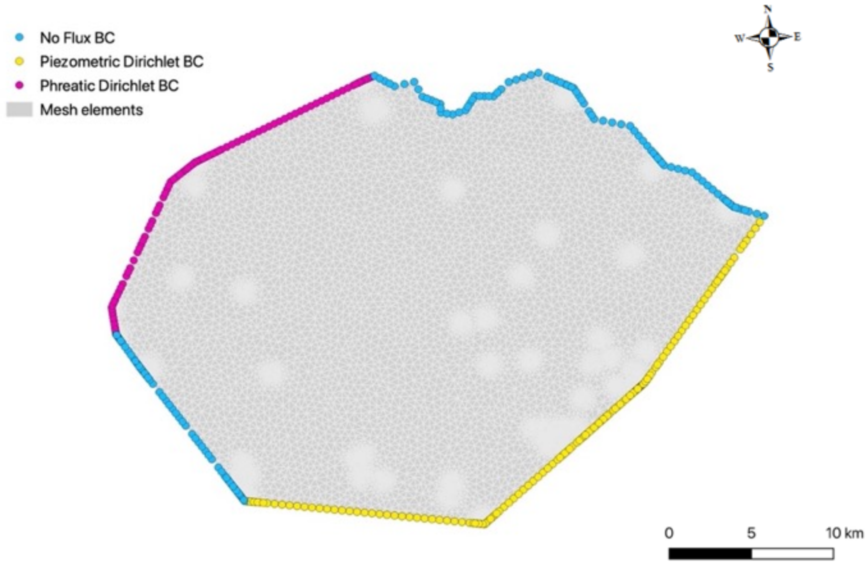

Figure 18: Deep boundary conditions, first mesh configuration.

Initial conditions were originally set as a pressure head distribution consistent with a uniform water table depth at 5 m depth. These will be adjusted case by case as described in the following sections.

3.1.3 Vertical and horizontal heterogeneity

The vertical heterogeneity is represented by the distribution of aquifers and aquitards. This can be roughly subdivided in three parts, visible in *Figure 19*: the northern white area, is characterized by an undifferentiated aquifer, the southern-east part, below the brown area, hosts a multilayer system with 8 confined aquifers, while the central part presumably hosts only portions of these aquifers (*Trentin, 2021*). The aquitards are 8 too, but in *Figure 19* is visible the configuration of only some of them.

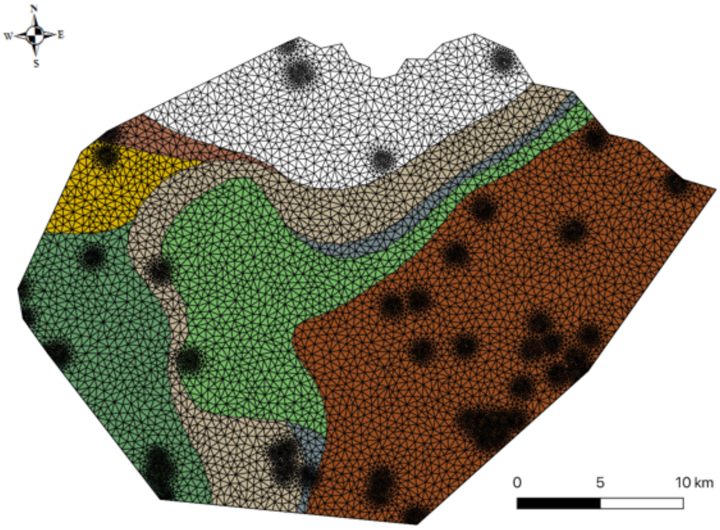

Figure 19: Aquitards extension.

Table 1: Soil use classes.

Macro-Classes	Legend
1	Urban centre
2	Arable Land
3	Orchards
4	Gardens
5	Deciduous forest
6	Wet fluvial environments

In addition to the vertical heterogeneity, also the horizontal heterogeneity, represented by the soil use distribution, was introduced thanks to the information furnished by the shape file of the "Carta di copertura del suolo" of Veneto Region. This map was realized by ARPAV, in 2012, through the "Unità Organizzativa Qualità del Suolo", which collected and elaborated available data, direct observation, physical-chemical sampling analyses. For a practical simplification, the original 34 classes were grouped in six macro-classes with similar land uses have been identified and implemented in the model. See Appendix (file *soil*) for the input parameters required by CATHY for each land use class.

The parameters allow to better implement and distinguish the different vegetation types in the model. From *Figure 20* and from a quantitative analysis is possible to know that the more diffuse land uses are *the arable land* (42%), followed by the *urban center* (29%). These data are in accordance with the economic Venetian traditions strongly based on agriculture, but also with the worrying trend of reducing the useful agricultural area, in favor of urban and industrial areas (*ARPAV, 2022*).

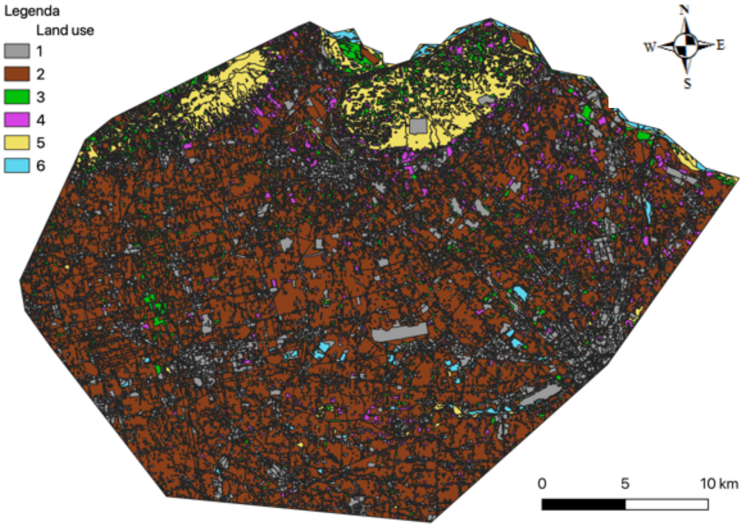

Figure 20: Land Use of the domain area.

3.1.4 Atmospheric boundary conditions

The land use indication is necessary, among other things, for the evapotranspiration quantification. Evapotranspiration is given by the sum of evaporation from the soil surface and transpiration from plants. Actual evapotranspiration depends on climatic factors but is limited by the amount of soil moisture. On the other hand, potential evapotranspiration, defined as the amount of water which would be lost from a surface completely covered with vegetation if there were sufficient water in the soil, depends on climate alone. When the precipitation exceeds the evapotranspiration, the surplus is partitioned between infiltration and surface runoff. When the precipitation is less than the evapotranspiration, the results is the drought (*Thornthwaite and Mather, 1951*).

Several are the models developed for the evapotranspiration estimation. Some of them are the *Penman–Monteith (Penman, 1948*; *Monteith 1965; McNaughton and Jarvis, 1984*), *Stanghellini (Stanghellini, 1980*; *Acquah et al., 2018)*, *Priestly–Taylor (Priestley and Taylor, 1972*; *Flint and Childs, 1991*), and *Hargreaves and Samani* (*Hargreaves and Samani, 1985*) models. They have different complexity, different assumptions and involve different parameters like aerodynamic resistance, stomatal resistance and intercepted radiation (*Ghiat et al., 2021*).

The model used in this project is the *FAO56 Penman–Monteith.* It has two formulations, the original one and the FAO56. The original Penman–Monteith equation estimates the potential evapotranspiration rate based on meteorological data and crop characteristics, combining the mass transfer and the surface energy balance. The FAO56 Penman–Monteith is considered as the standard method for estimating the crop evapotranspiration (Etc) linking the reference evapotranspiration (Eto) with a crop coefficient (Kc) related to the vegetation type and period of the year. The relation that links the crop coefficient with the potential and the reference evapotranspiration is given by:

$$ET_c = K_c\, ET_o$$

Whose meanings are:

ET_c crop potential evapotranspiration [mm d^{-1}],

K_c crop coefficient [dimensionless],

ET_o reference crop evapotranspiration [mm d^{-1}].

Once obtained the crop evapotranspiration it was possible to evaluate the atmospheric boundary conditions: rainfall + irrigation – **potential** evapotranspiration.

Atmospheric boundary conditions were assumed variable in space and time (with a daily resolution) and consist of the net sum of precipitation and irrigation minus potential evapotranspiration. Precipitation daily data were obtained from the ARPAV website (https://wwwold.arpa.veneto.it/bollettini/storico/Mappa_2018_PREC.htm?t=RG) and properly interpolated (*Trentin, 2020*), while irrigation rates were provided by Consorzio di Bonifica Piave and applied on the relevant areas.

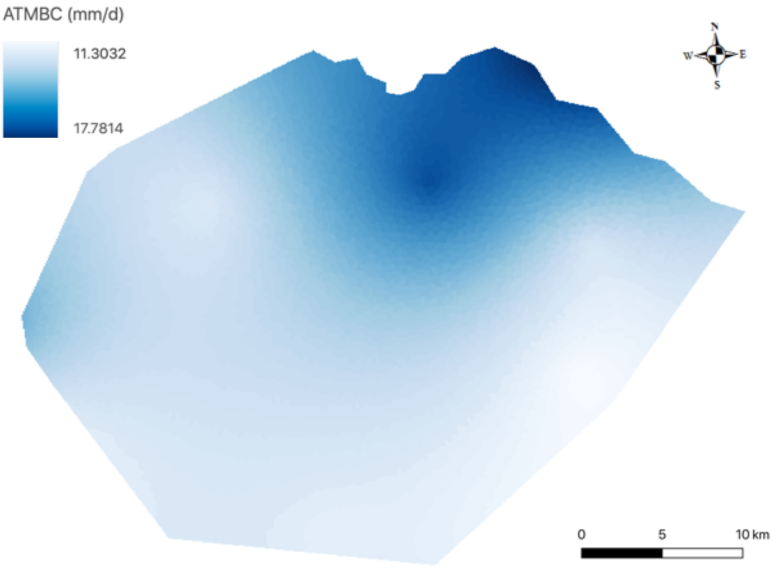

Figure 21: Example of atmospheric boundary conditions distribution (mm/d).

Figure 21 shows the distribution of the atmospheric boundary conditions on a day in winter 2018. In this case, the net atmospheric flux (rain + irrigation – evapotranspiration) was more intense in the north piedmont area, as we could expect: in the mountainous area precipitation are more intense and the temperature, being lower, reduces the evapotranspiration (*Barbi et al., 2011*).

3.1.5 Uncalibrated simulations

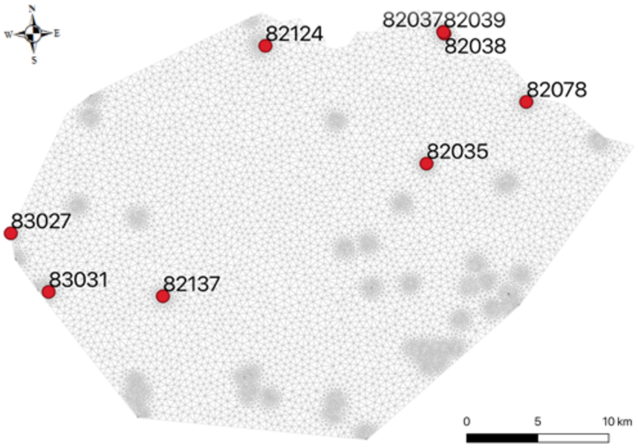

Figure 22: Location of wells for the comparison between real and simulated water table.

Once the model setup was complete some preliminary simulations were run to assess the model performance. The time period chosen for the simulations goes from 1st January 2018, up to 31st December 2018. The comparison between observed water table level and simulated water table level was done on 9 surface wells, whose location is indicated in *Figure 22*.

Figure 23a represents the observed water level time series during year 2018. Despite some data it can be noticed that the general trend of the water table does not change much over the year. *Figure 23b* shows the simulated water table in the same wells, which exhibit larger fluctuations compared to the observations, particularly at the beginning, when the effects of the initial conditions are not dissipated yet.

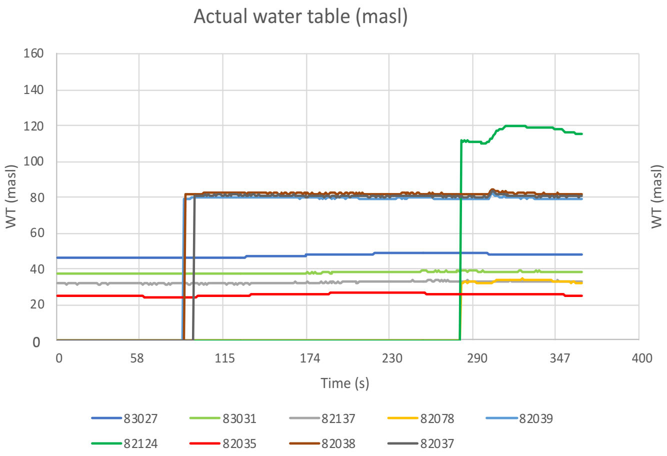

Figure 23a: Measuredl water table position.

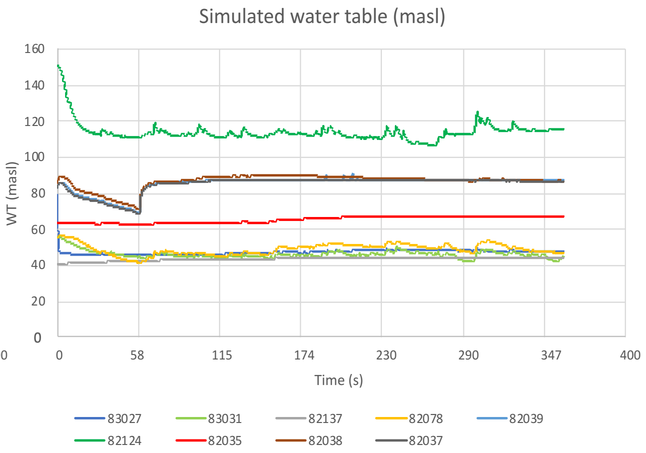

Figure 23b: Simulated water table position.

Overall, the correspondence between observed and simulated water table is acceptable, although this could be due to the proximity to the border, where the boundary conditions are imposed. In fact, well 82035, far from the boundary, shows a larger discrepancy between the observed value and the simulation result.

3.2 Second model configuration

After some trials a new version of the mesh was built, in which the degree of complexity was increased. Also this complex mesh was implemented in CATHY. The number of surface nodes and vertical layers were doubled: 16112 nodes on the surface, 43 layers, and a total number of nodes equal to 692816. This was done to increase the accuracy in the representation of the Sile River and the multi-aquifer system.

3.2.1 Mesh refining

A first important difference between the two meshes is the introduction of a finer discretization of the Sile river, an important watercourse that acts as a sink source in the domain, previously neglected (*Figure 24* and *25*). Sile river indicates the beginning of *risorgive* area in the south of the domain.

The size of the mesh requires the use of a high-end workstation for running the simulations, no more supported by a personal computer. I used a virtual machine in CloudVeneto. CloudVeneto is an OpenStack-based cloud. It allows the instantiation of Virtual Machines of the desired environments. It also provides storage volumes that can be attached to such virtual instances (*http://userguide.cloudveneto.it/en/latest/index.html*).

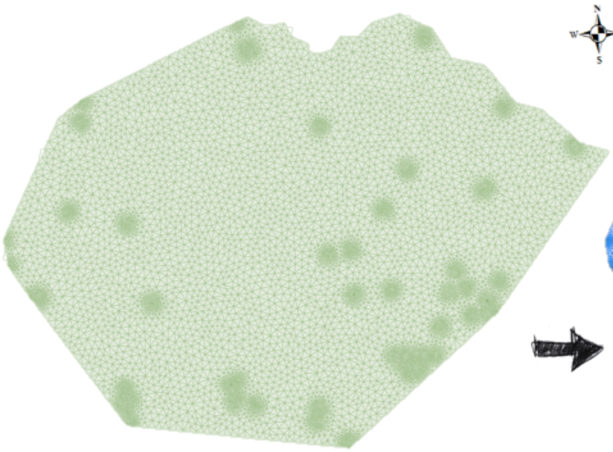
Figure 24: First surface mesh, 7793 nodes.

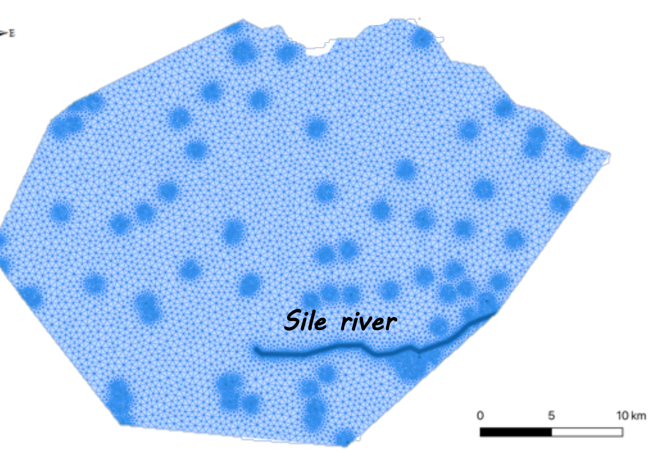

Figure 25: New surface mesh, 16112 nodes.

3.2.2 Boundary conditions and initial conditions

In the second mesh configuration the nodes interested by the Neumann condition are unchanged, and unchanged are also the initial conditions in which again a homogeneous water table with 5m of depth is imposed on the whole domain. Some modifications have been done on the surface Dirichlet boundary conditions, having introduced Sile river discretization. While in FeFlow it was necessary to impose a seepage face condition in the Sile nodes, CATHY is able to evaluate by itself the water exiting from the domain and remove it, thanks to its peculiar boundary-condition switching procedure. In the south nodes of the two shallowest slices, a no flux boundary condition was imposed (*Figure 26*), while in the deep layers boundary conditions are unchanged with respect to the first mesh configuration (*Figure 27*). We refer to *phreatic conditions* when the aquifer is unconfined, and to *piezometric conditions* when the aquifers are confined.

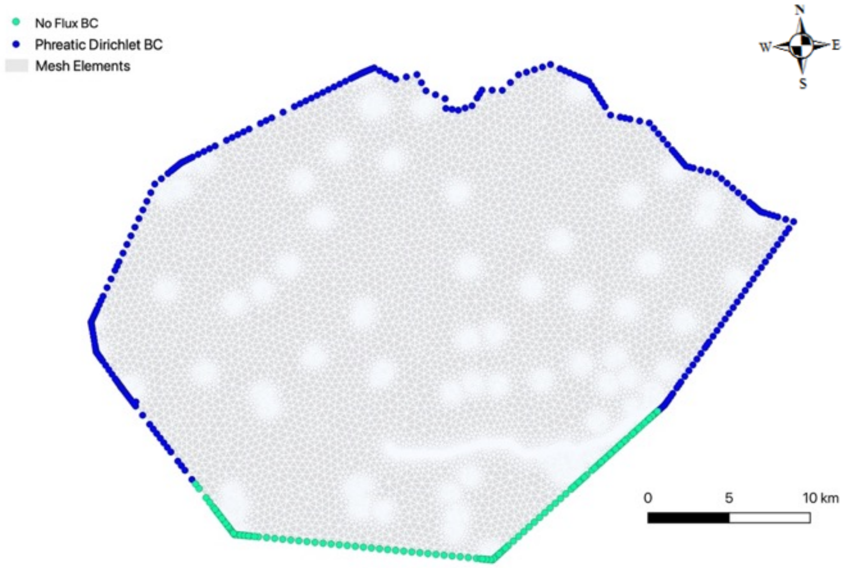

Figure 26: Top layers boundary conditions, second mesh configuration.

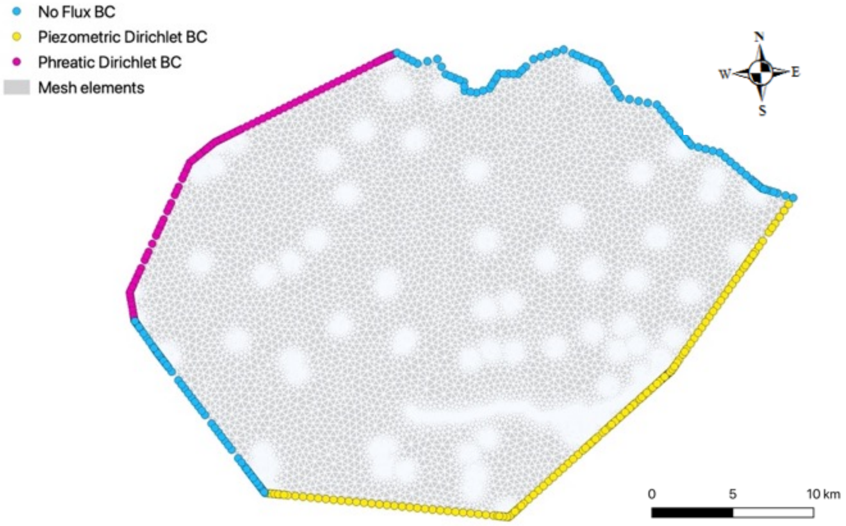

Figure 27: Deep layers boundary conditions, second mesh configuration.

3.2.3 Vertical heterogeneity

A modification was done also in the aquitards distribution. Their extension is quite different with respect to *Figure 19*. *Figure 28* shows the new aquitards configuration, which is in this case characterized by a less variable spatial distribution. The presence of a low conductivity area in the *risorgive* belt (South Sile) is another novelty: this allows for the representation of artesian conditions in the first shallow aquifer in that region.

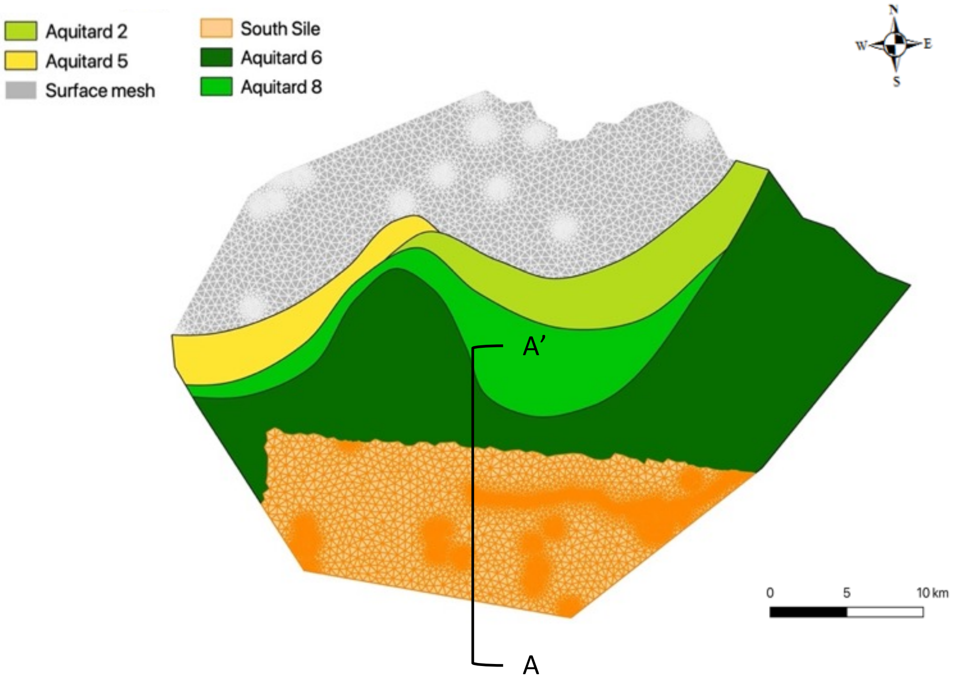

Figure 28: New aquitard configuration.

Compared to *Figure 19,* the size of the aquitards is slightly reduced, while the undifferentiated aquifer in the northern Piedmont area, has a bigger extension. The aquifers and aquitards layering is basically unchanged, except for the number of numerical layers that discretized each stratum (*Figure 29*).

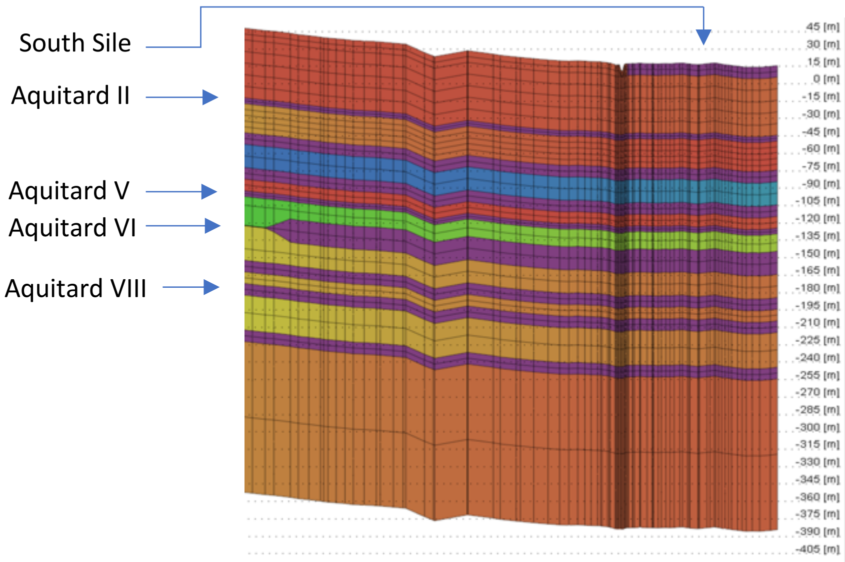

Figure29: Section A-A'. Aquifers and aquitards layering. Only aquitards appearing in figure 28 are highlighted.

3.2.4 Sensitivity analysis

A sensitivity analysis was performed before the proper calibration. *Figure 30* shows in red the wells that are withdrawing water from the unconfined aquifer, while the deep wells are indicated in green. Among the hundreds of wells present in the area, water table data for years 2018 and 2019, are available only for these 42 wells.

The first step in the sensitivity analyses was the definition of the aquifer, each well is extracting water from. *Table 2* shows that 21 wells are withdrawing water from the unconfined aquifer, while the other 21 wells are extracting water from the deeper aquifers.

Table 2: Well and correspondent aquifer.

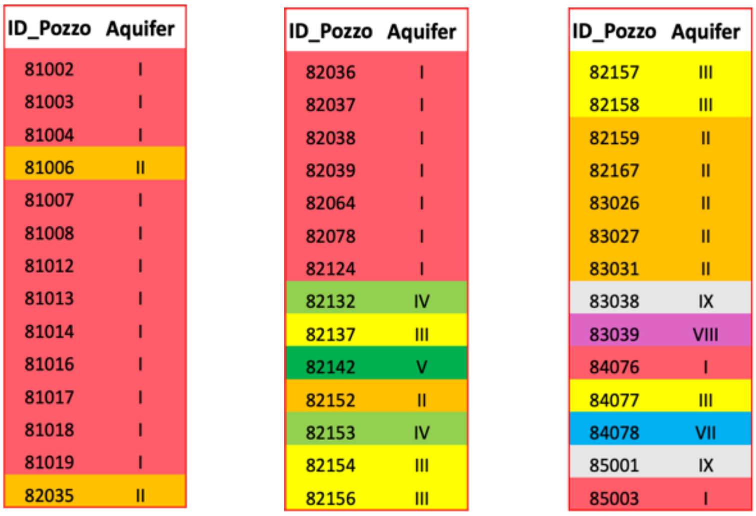

ID_Pozzo	Aquifer
81002	I
81003	I
81004	I
81006	II
81007	I
81008	I
81012	I
81013	I
81014	I
81016	I
81017	I
81018	I
81019	I
82035	II
82036	I
82037	I
82038	I
82039	I
82064	I
82078	I
82124	I
82132	IV
82137	III
82142	V
82152	II
82153	IV
82154	III
82156	III
82157	III
82158	III
82159	II
82167	II
83026	II
83027	II
83031	II
83038	IX
83039	VIII
84076	I
84077	III
84078	VII
85001	IX
85003	I

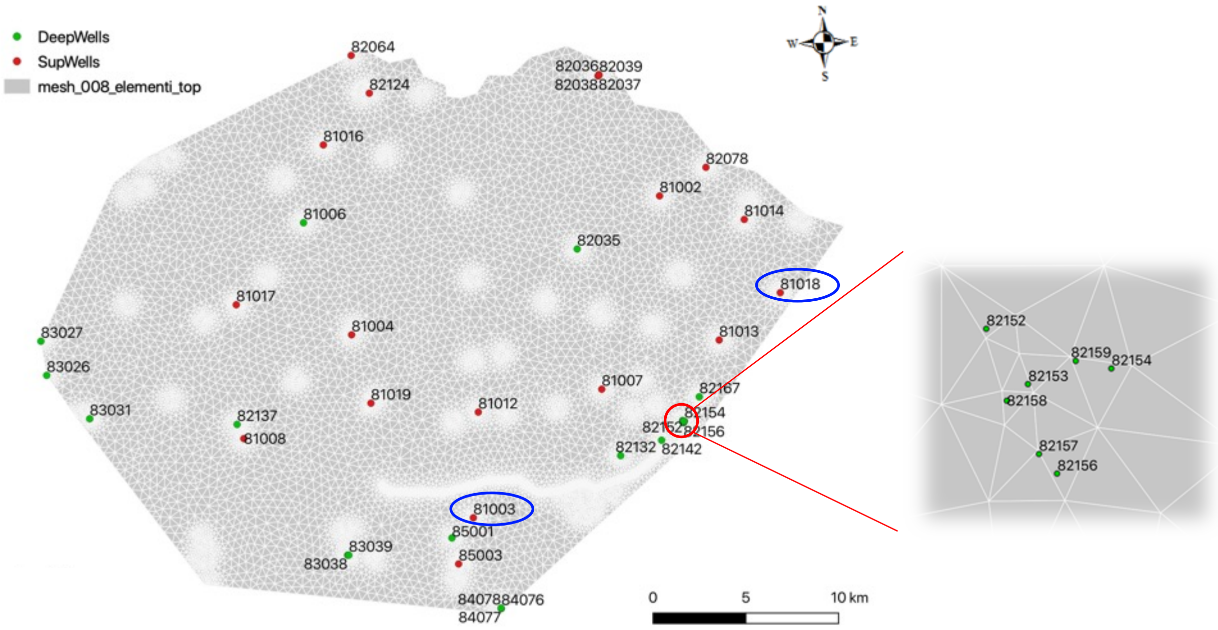

Figure 30: Location of 42 wells for which piezometric data are available. The two wells circled in blue are considered for a specific analysis reported below.

The next step was the definition of a *base* configuration, used as a reference for the comparison with the varied parameter sets (*Table 3*) for the model sensitivity to the aquifers and aquitards hydraulic conductivity (Ks_{aquifer} and Ks_{aquitard}), and the aquifer and aquitard specific storage (Ss_{aquifer} and Ss_{aquitard}).

Table 3: Range of parameter variations in the sensitivity analysis. The base configuration values are evidenced in pink, while the modified parameter, in the eight configurations, is indicated in red, and it gives the name to the simulation.

Sensitivity Analysis	**Ks_{aquifer} [m/s]**	**Ks_{aquitard} [m/s]**	**Ss_{aquifer} [1/m]**	**Ss_{aquitard} [1/m]**
Base	10^{-4}	10^{-7}	10^{-5}	10^{-5}
Aquifer_E-03	**10^{-3}**	10^{-7}	10^{-5}	10^{-5}
Aquifer_E-05	**10^{-5}**	10^{-7}	10^{-5}	10^{-5}
Aquitard_E-06	10^{-4}	**10^{-6}**	10^{-5}	10^{-5}
Aquitard_E-08	10^{-4}	**10^{-8}**	10^{-5}	10^{-5}
Storage_Aquifer_E-03	10^{-4}	10^{-7}	**10^{-3}**	10^{-5}
Storage_Aquifer_E-04	10^{-4}	10^{-7}	**10^{-4}**	10^{-5}
Storage_Aquitard_E-03	10^{-4}	10^{-7}	10^{-5}	**10^{-3}**
Storage_Aquitard_E-04	10^{-4}	10^{-7}	10^{-5}	**10^{-4}**

The values were changed one at a time within a reasonable range, and the best configuration was defined through the assessment of the model performance comparing the simulated and observed water table data in terms of *Coefficient of Determination* (R2), *Root Mean Square Error* (RMSE) and *Kling Gupta Efficiency* (KGE):

- the Coefficient of Determination is the square of the Correlation Coefficient, it goes from 0 to 1, and it represents the degree of similarity of the two values (*Chicco et al., 2021*),

- the Root Mean Square Error is a measure of the differences between values, in this case measured and simulated. A value of 0 would indicate a perfect fit of the data (*Chicco et al., 2021*),

- the Kling Gupta Efficiency combines the three components of Nash-Sutcliffe efficiency (NSE) of model errors: correlation, bias, coefficients of variation, and has been widely used for calibration of hydrological models in recent years (*Korben et al., 2019*), whereby the largest possible value is 1, indicating perfect match.

Comparing the metric results, the parameters that gave the better performances were grouped in a single configuration. *Table 4* reports the parameters values for each aquifer and each aquitard. This configuration is hereafter defined “best” set. The word *best* is in quotes because this configuration comes from a manual sensitivity analysis, whereas an automatic calibration procedure is likely to provide a better performance.

Table 4: Sensitivity analysis results, best set configuration.

Aquifer #	**$K_{S\ aquifer}$ [m/s]**	**$Ss_{aquifer}$ [1/m]**	**Aquitard #**	**$Ks_{aquitard}$ [m/s]**	**$S_{s\ aquitard}$ [1/m]**
I	10^{-3}	10^{-3}	**II**	10^{-6}	10^{-4}
II	10^{-4}	10^{-3}	**III**	10^{-6}	10^{-4}
III	10^{-4}	10^{-3}	**IV**	10^{-6}	10^{-4}
IV	10^{-4}	10^{-3}	**V**	10^{-6}	10^{-4}
V – VI – VII – VIII – IX	10^{-4}	10^{-5}	**VI – VII – VIII – IX**	10^{-6}	10^{-5}

Table 4 summarizes the best combination of parameters resulting from the sensitivity analysis. Note that the model is much more sensitive to the hydraulic conductivity than to the elastic specific storage.

Considering the set of parameters of *Table 4* an additional analysis was carry out: the initial condition of the input water table depth was initially assumed of 5 m, in a second simulation it was set at 20 m. This condition is assumed uniform over the whole domain and does not consider the different hydro-geomorphological characteristics of the area.

The metric performances were again evaluated (*Table 5* and *6*). In accordance with *Figure 31*, the red color indicates the wells that are drawing water from the unconfined aquifer, while the deep wells are indicated in green.

Table 5: Metric of performances, WT depth = 5 m.

ID	81002	81003	81004	81006	81007	81008	81012	81013	81014	81016	81017
R2	0.0094	0.6551	0.1499	0.0009	0.2706	0.0564	0.5305	0.1505	0.0338	0.0124	0.1040
RMSE	113.4941	2.3757	12.7925	31.0242	36.8561	109.6007	4.1163	124.3115	19.1159	42.6675	132.3111
KGE	-6.4488	-9.5585	-0.6772	-0.4413	-0.9522	-2.5827	0.0265	-6.3784	-0.4187	-0.5222	-18.5454

ID	81018	81019	82035	82036	82037	82038	82039	82064	82078	82124	82132
R2	0.0202	0.0098	0.0225	0.0419	0.0147	0.0192	0.0337	0.1607	0.6111	0.6936	0.0022
RMSE	3.8915	10.6571	29.2048	7.1091	7.6481	8.7558	6.9214	2.0777	30.8702	93.2603	8.5921
KGE	-0.1459	-0.2663	-0.4069	-9.3833	-9.5039	-12.5506	-11.3047	-0.9074	-1.3262	-1.3213	-1.5257

ID	82137	82142	82152	82153	82154	82156	82157	82158	82159	82167	83026
R2	0.0008	0.0062	0.2087	0.1124	0.0064	0.0116	0.0001	0.1257	0.0000	0.0260	0.3152
RMSE	16.3113	2.2032	37.0696	8.8684	125.5169	88.4177	52.7216	14.4106	24.0334	1.0393	21.1355
KGE	-1.0282	0.0152	-2.2004	-0.0237	-8.6119	-4.5951	-3.1532	-0.7854	-1.0012	0.1573	0.2771

ID	83027	83031	83038	83039	84076	84077	84078	85001	85003
R2	0.0679	0.0633	0.0463	0.0849	0.1950	0.0000	0.0019	0.0732	0.0010
RMSE	32.9089	23.9182	1.4270	48.2503	2.5647	18.0249	17.4291	45.4741	2.1195
KGE	-0.0576	-0.0108	-0.4192	-2.1796	0.3758	-0.5203	-0.4313	-2.3728	-0.0325

Table 6: Metric of performances, WT depth = 20m.

ID	81002	81003	81004	81006	81007	81008	81012	81013	81014	81016	81017
R2	0.0006	0.2498	0.1152	0.0031	0.0372	0.0563	0.0171	0.1394	0.3329	0.0070	0.0979
RMSE	11.0686	16.0256	25.9557	30.5000	7.4194	8.7177	2.6996	10.8045	13.2936	63.7179	51.1738
KGE	-1.9150	-13.8688	-0.8446	-0.4852	-0.2779	0.1402	-1.6119	-0.5106	-0.8255	-0.4427	-6.4558

ID	81018	81019	82035	82036	82037	82038	82039	82064	82078	82124	82132
R2	0.0868	0.3038	0.0224	0.0217	0.0206	0.0275	0.0283	0.4246	0.5087	0.3949	0.0235
RMSE	4.1408	2.3557	15.2052	6.4144	6.8845	8.1524	6.1185	1.7219	31.9198	110.4873	4.6547
KGE	-12.4802	-2.4068	-0.2860	-7.1696	-7.1266	-9.8109	-8.5933	0.1763	-2.2980	-1.8348	-11.6621

ID	82137	82142	82152	82153	82154	82156	82157	82158	82159	82167	83026
R2	0.0791	0.0056	0.3020	0.0700	0.0975	0.0323	0.0870	0.5551	0.1320	0.3835	0.7603
RMSE	3.3818	5.3572	32.5047	7.9796	124.3463	76.7659	37.6494	8.1453	9.0544	5.8731	30.3069
KGE	0.0089	-3.5182	-2.4909	0.0324	-7.8990	-4.2443	-1.9324	0.0748	-4.0501	-3.2071	-3.2654

ID	83027	83031	83038	83039	84076	84077	84078	85001	85003
R2	0.8143	0.8000	0.3542	0.0808	0.0936	0.0000	0.0004	0.0293	0.5408
RMSE	37.3783	28.9548	5.4406	46.7855	2.4463	18.2044	17.6518	44.2279	13.3688
KGE	-3.5401	-6.4756	-5.1547	-1.5057	-3.5697	-0.9818	-0.8961	-1.5735	-26.8655

From the results presented in *Table 5* and *6* it is clear how a simple sensitivity analysis cannot provide an optimum fit between observed and simulated data: the coefficient of determination and the Kling Gupta efficiency are small, while the root mean square error is high. It would be hard to define which of the two configurations shows overall the better performance. In *Figure 21* two wells water table depth time series are presented. Blue circles of *Figure 20* indicate the position on the map of well 81003 and 81018.

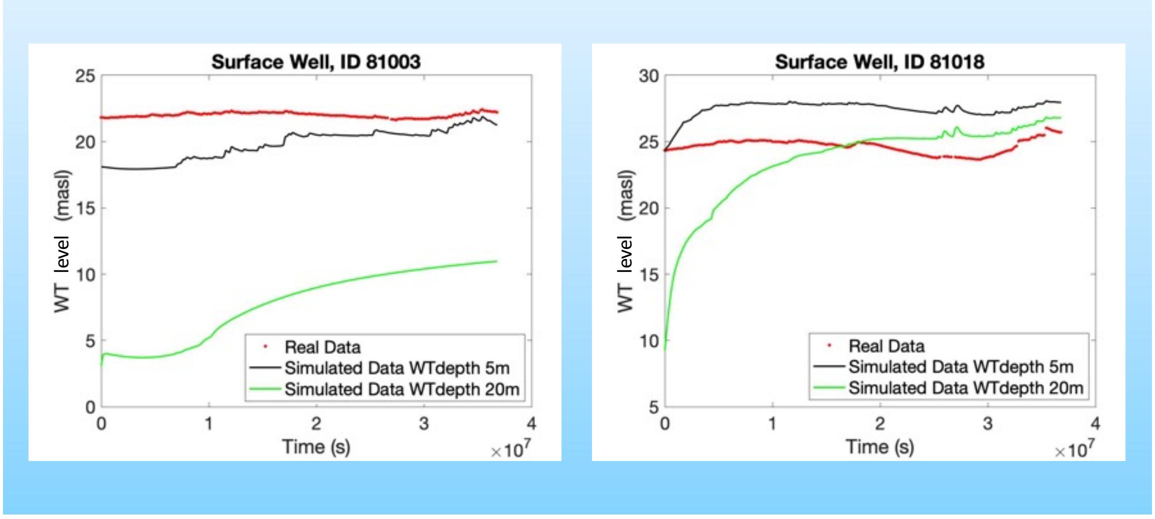

Figure 31: Water table depth time series in two observation wells. Period of simulation 15/04/2018 - 15/06/2019 (426 days).

Figure 31 shows in red the real water table time series, in black the simulated time series with input water table depth at 5 m, and in green the simulated time series with input water table depth at 20 m. Considering only the wells of the figure, the 5 m input data seem to better follow the real water table behavior, but looking at the metric performance results of the other available wells, this doesn't happens in all the cases.
Prior to the calibration process, to improve the hydraulic conductivity value, a further step in the model complexity was introduced in the domain configuration.

3.2.5 Hydraulic Conductivity

To increase the precision of the hydraulic conductivity (*ks*) parameter selection, the information contained in *Carta della permeabilità dei suoli* (published in 2016), downloaded from Veneto Region geoportal (https://gaia.arpa.veneto.it/maps/294), were implemented in the model. This is a map that subdivides Veneto region in four hydraulic conductivity macro-areas. Each macro-area has an indication of the *ks* range in that specific location:

- low = $10^{-8} – 10^{-7}$ m/s
- moderately low = $10^{-7} – 10^{-6}$ m/s
- moderately high = $10^{-6} – 10^{-5}$ m/s
- high = $10^{-5} – 10^{-4}$ m/s

Figure 32a shows the hydraulic conductivity map distribution of the domain of study: *low*, *moderately low*, m*oderately high* and *high ks.* These *ks* apply only the surface layers up to the first aquitard.

In accordance with the initial description of the domain area, in the northern part, characterized by granular materials, a zone of *high* hydraulic conductivity is present, underlined in green. A blue *low* hydraulic conductivity strip seems to indicate the height at which *risorgive* area begins. In correspondence with Montello hill and Colli Asolani on the north, and in correspondence with *risorgive* area on the south, a hydraulic conductivity in the *moderately low* range, is indicated in magenta. *Moderately high ks*, in orange, characterize the rest of the whole area. This surface differentiation was superposed to the original vertical layering (distinction between aquifers and aquitards), resulting in 3D distribution of *ks* as shown in *Figure 32b*.

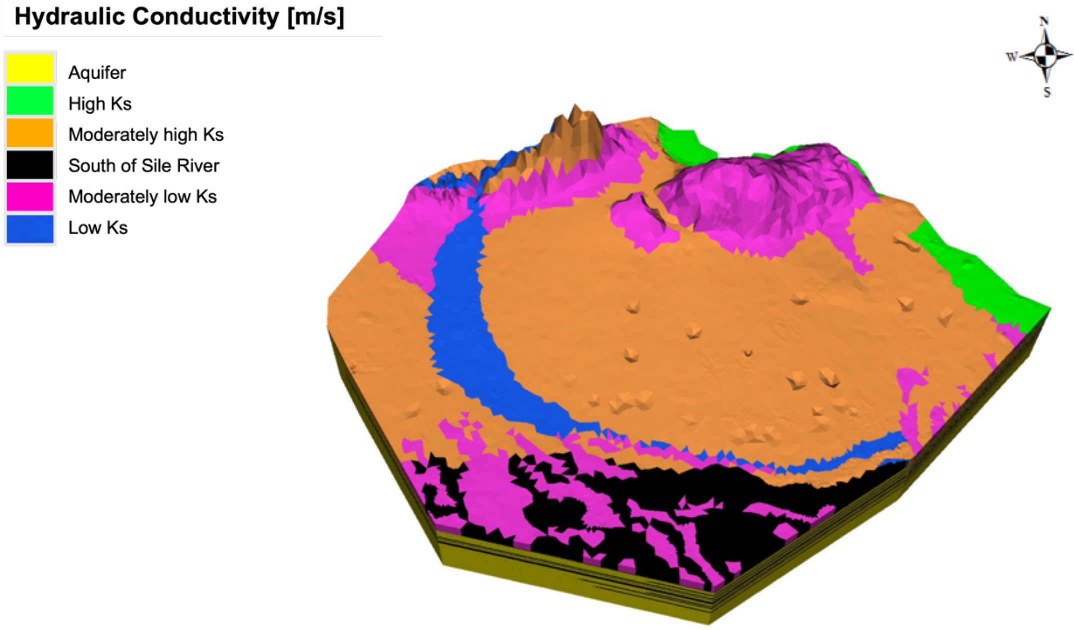

Figure 32a): Hydraulic conductivity zones of the study area. Planar view.

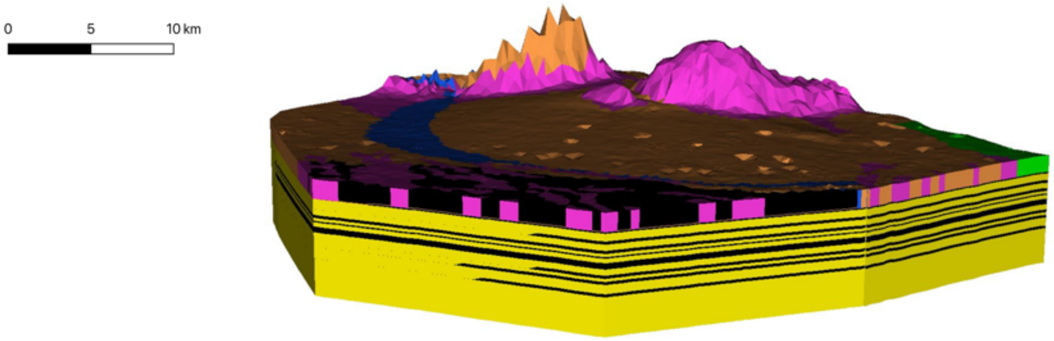

Figure 32b): Hydraulic conductivity zones of the study area. East side view.

In *Carta della permeabilità dei suoli* a *ks* range of variability is indicated, but the model requires a precise input value, so the mean value was chosen, as indicated in the legend. The range is an important indication for the calibration process, presented in the next chapter.

3.3 Third model configuration

3.3.1 Mesh

This model configuration is a modification of the second mesh. It has been chosen with the purpose of optimizing both the time for calibration and the physical configuration of the domain. The previous mesh, having a huge number of nodes, would have required a too long time for the calibration. Moreover, it was built with the bottom parallel to the surface, while in this case a flat horizontal base was imposed, with a minimum thickness of 25m with respect to the lower node of the DEM. The new mesh, with a number of layers equal to 13, aims to reproduce the undifferentiated aquifer only, neglecting the aquitards and the confined aquifers. Also the layers thickness was changed, refining the superficial ones, that in the second mesh was too coarse. These are the percentages of the layers thickness: 0.005, 0.005, 0.01, 0.01, 0.02, 0.03, 0.04, 0.05, 0.06, 0.12, 0.12, 0.2, 0.28.

3.3.2 Dirichlet boundary conditions

Before proceeding with the calibration, some more adjustments have been done to the model with respect to the "second mesh configuration". First, on the nodes of the boundary touched by Piave river, interpolated values of pressure head were applied, obtained from the elaboration of river level data provided by the ARPAV official site, *ARPAV – Dipartimento Regionale per la Sicurezza de l Territorio Servizio Idrologico*.

Table 7: Piave hydrometric levels [m], in 3 stations: Segusino, Nervesa della Battaglia and Ponte di Piave.

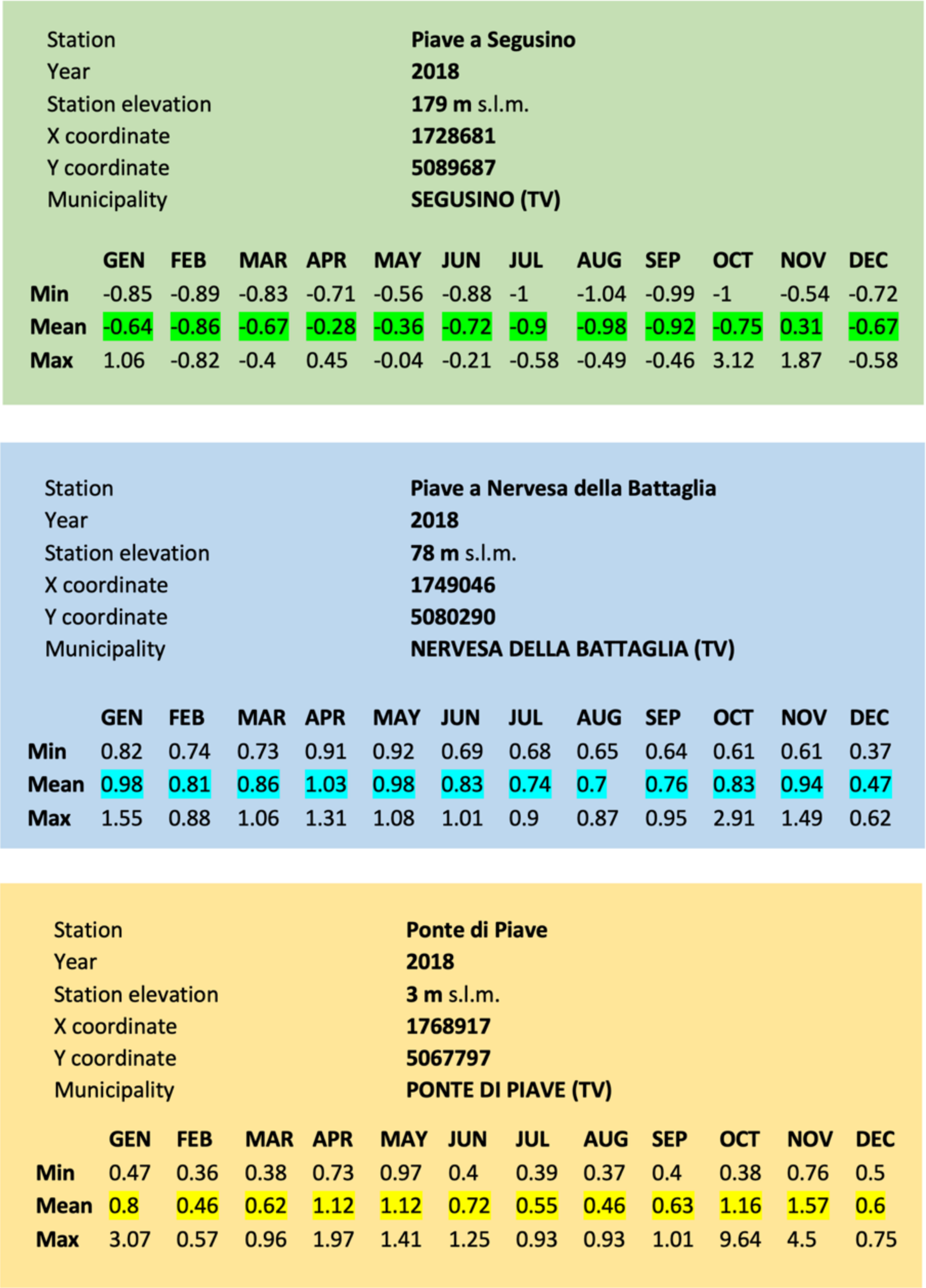

Station	**Piave a Segusino**
Year	**2018**
Station elevation	**179 m** s.l.m.
X coordinate	**1728681**
Y coordinate	**5089687**
Municipality	**SEGUSINO (TV)**

	GEN	**FEB**	**MAR**	**APR**	**MAY**	**JUN**	**JUL**	**AUG**	**SEP**	**OCT**	**NOV**	**DEC**
Min	-0.85	-0.89	-0.83	-0.71	-0.56	-0.88	-1	-1.04	-0.99	-1	-0.54	-0.72
Mean	-0.64	-0.86	-0.67	-0.28	-0.36	-0.72	-0.9	-0.98	-0.92	-0.75	0.31	-0.67
Max	1.06	-0.82	-0.4	0.45	-0.04	-0.21	-0.58	-0.49	-0.46	3.12	1.87	-0.58

Station	**Piave a Nervesa della Battaglia**
Year	**2018**
Station elevation	**78 m** s.l.m.
X coordinate	**1749046**
Y coordinate	**5080290**
Municipality	**NERVESA DELLA BATTAGLIA (TV)**

	GEN	**FEB**	**MAR**	**APR**	**MAY**	**JUN**	**JUL**	**AUG**	**SEP**	**OCT**	**NOV**	**DEC**
Min	0.82	0.74	0.73	0.91	0.92	0.69	0.68	0.65	0.64	0.61	0.61	0.37
Mean	0.98	0.81	0.86	1.03	0.98	0.83	0.74	0.7	0.76	0.83	0.94	0.47
Max	1.55	0.88	1.06	1.31	1.08	1.01	0.9	0.87	0.95	2.91	1.49	0.62

Station	**Ponte di Piave**
Year	**2018**
Station elevation	**3 m** s.l.m.
X coordinate	**1768917**
Y coordinate	**5067797**
Municipality	**PONTE DI PIAVE (TV)**

	GEN	**FEB**	**MAR**	**APR**	**MAY**	**JUN**	**JUL**	**AUG**	**SEP**	**OCT**	**NOV**	**DEC**
Min	0.47	0.36	0.38	0.73	0.97	0.4	0.39	0.37	0.4	0.38	0.76	0.5
Mean	0.8	0.46	0.62	1.12	1.12	0.72	0.55	0.46	0.63	1.16	1.57	0.6
Max	3.07	0.57	0.96	1.97	1.41	1.25	0.93	0.93	1.01	9.64	4.5	0.75

The hydrometric values, available also for year 2019 and 2020, have been registered in the stations whose positions are indicated in *Figure 33*. The pressure head value, obtained through the subtraction of the node elevation from the hydrometric value, after a linear interpolation in time and space, was applied to the northeast boundary, evidenced in light blue in *Figure 34*. This value was applied to the nodes of the slices that have a maximum distance from the surface slice of maximum 2.5m (talweg).

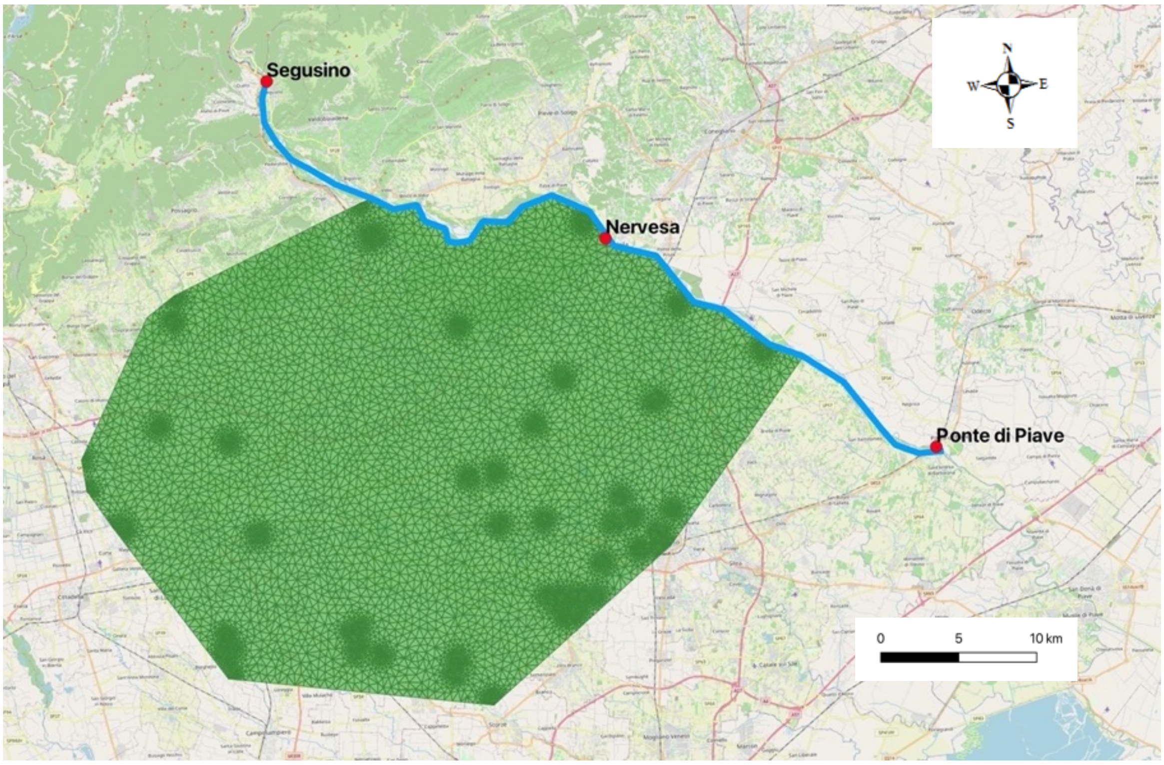

Figure 33: Piave stations position.

A new Dirichlet boundary condition was imposed also in the north-west boundary, evidenced in yellow in *Figure 34*. The same water table time series depth of well 82064 has been imposed to all the north-west border to improve the water table simulation behavior in that side of the domain.

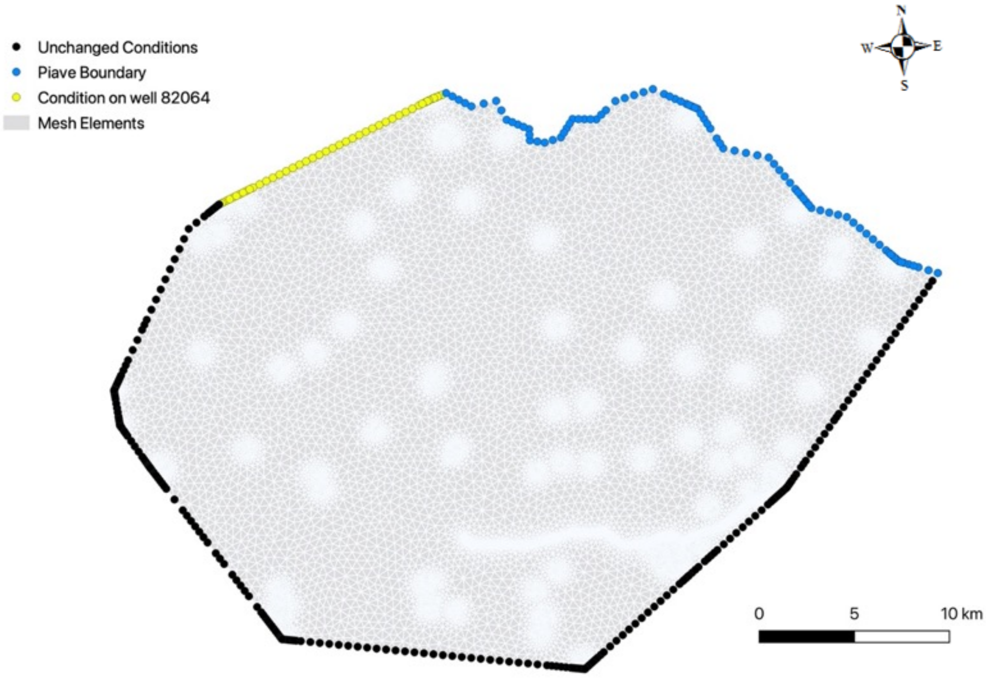

Figure 34: New Dirichlet boundary conditions.

3.3.3 Neumann boundary conditions

Having cut the lower part of the domain, the number of nodes with pumping is decreased with respect to the previous domain configurations. The wells appearing in *Figure 35* are wells that extracts water from the unconfined aquifer only.

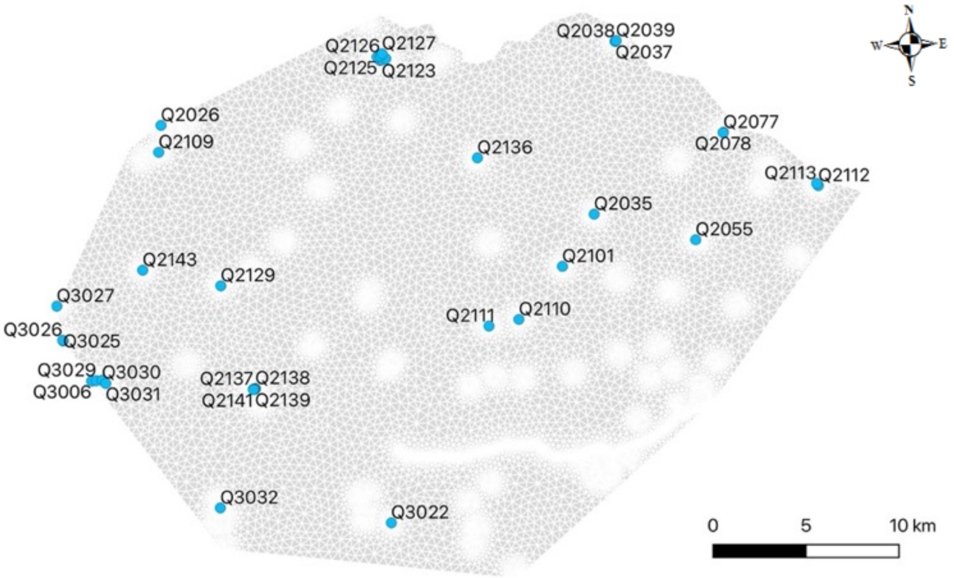

Figure 35: Nodes interested by Neumann condition, third mesh configuration.

3.3.4 Initial conditions

In the simulations performed up to now, the initial condition imposed consist of a homogeneous water table depth of 5 m over the whole domain. To obtain a more realistic initial condition, a spin-up simulation was run with the homogeneous water table depth as initial condition, and the pressure distribution obtained in each node of the 3D mesh was then imposed as new initial condition of the new set of simulation for the calibration process. *Figure 36* shows pressure head distribution of the surface nodes layer

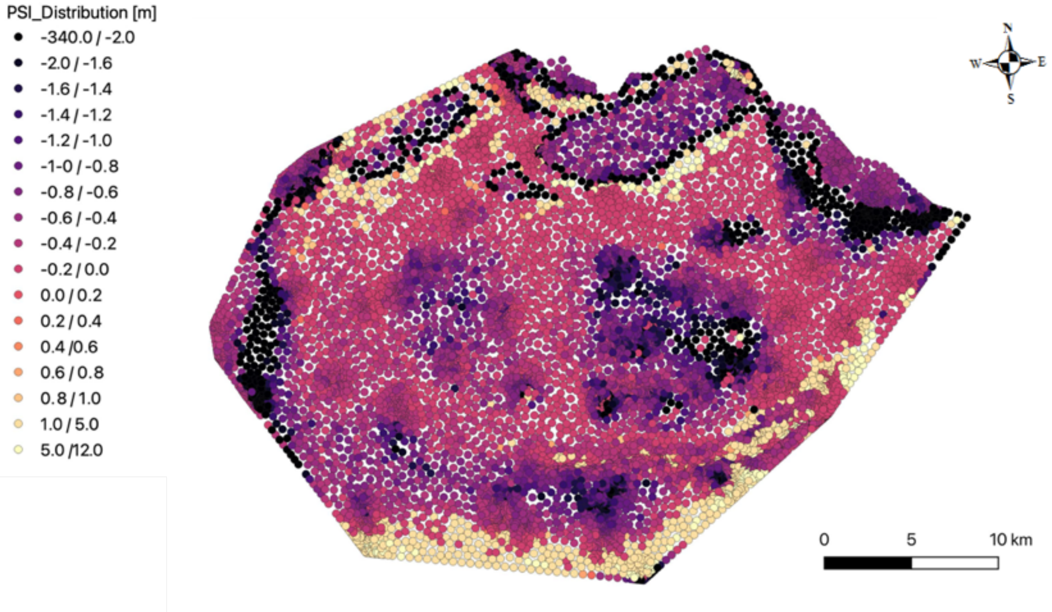

Figure 36: Superficial pressure head distribution, imposed as initial condition for the calibration process.

3.3.5 Porosity

Before starting with the calibration process, some modifications were implemented. Values of porosity were up to now unrealistically assumed as homogeneous for all the types of soils.

Starting from the six classes indicated in *Figure 32* and according to their hydraulic conductivity values, for each of them a porosity value was defined based on the literature (e.g. *Carsel and Parrish, 1988*). Only for the deep *aquifer* zone the value of porosity was left equal to 0.30.

Table 8: Permeability and porosity values. Orange = Zone 1, Black = Zone 2, Blu = Zone 3, Magenta = Zone 4, Green = Zone 5.

	Permeability [m/s]		**Porosity [/]**
Coarse Gravel	1.00E-01		0.28
Medium Gravel	1.00E-02	1.00E-04	0.32
Fine Gravel	1.00E-03	1.00E-05	0.34
Coarse Sand	1.00E-03	1.00E-05	0.39
Medium Sand	1.00E-04	1.00E-06	0.39
Fine Sand			**0.43**
Silt	1.00E-06	1.00E-08	0.46
Clay	1.00E-09		0.42

4. Model calibration

Even if the performances of groundwater models and their simulation speed have rapidly increased over the years, their calibration remains an open challenge. The aim of a calibration process is to reduce the discrepancy between the measured and the simulated data, by finding the suitable parameters among a physical range furnished by the modeler. The misfit between the observations and the simulations comes from the simplifications introduced for the model building, the unknown boundary conditions, and from the big number of input parameters whose value is uncertain. These parameters are generally not directly measurable in the field, and so they must be estimated through calibration (*Duan et al., 1994*; *Shoarinezhad et al., 2020*). The degree of fitting between observed and simulated data is called *calibration criterion* or *objective function*. The calibration algorithm will look for that parameter value able to minimize or maximize the objective function. During the study two calibration algorithms were considered: Parameter ESTimation (PEST) and Shuffled Complex Evolution – University of Arizona (SCE-UA).

4.1 PEST algorithm

PEST, Parameter ESTimation, is a non-linear inverse modeling code developed by John Doherty in 2015 (*Doherty, 2015*). It is generally used in the decision support modeling and environmental decision making like groundwater, surface water, land use, etc... In these fields is often easier to measure physical quantities like heads, fluxes, or concentrations, than parameters like hydraulic conductivity, specific storage, or porosity. This is why in calibration is necessary to proceeds through the inverse problem, i.e., the system input parameters are inferred from the outputs optimization. PEST try to find the minimum of the objective function, defined as:

$$\varphi = \sum (w_i r_i)^2$$

Where r_i, the residual, is defined as $r_i = h_{calculated} - h_{observed}$, while w_i are the weights that are applied to the measurements.

Gauss-Levenberg-Marquardt algorithm (GLMA) is the algorithm used for the research of the minimum. The GLMA proceeds iteratively in the model input optimization, changing the input values within the parameter range suggested by the modeler, until the best fitting between the calculated quantities ($h_{calculated}$) and the observed ones ($h_{observed}$) is reached (*Doherty, 2015; FePEST 7.1 Documentation)*.

A functionality offered by PEST, is the parallelization of the calibration. This allows to run multiple simulations at the same time, to reduce the computational time.

4.2 SCE-UA algorithm

SCE-UA, Shuffled Complex Evolution – University of Arizona, is a global optimization method realized for the conceptual watershed models calibration, based on the synthesis of three existing approaches and a new one: the Simplex method of *Nelder and Mead (1965),* the concepts of controlled random search (*Price, 1987*), competitive evolution (*Holland, 1975*) and the new concept of complex shuffling, developed by *Duan et al. (1994).*

A brief explanation of this algorithm can be as follows. An initial population of points is sampled randomly in the space of research. These points are then subdivided in communities, called complexes. Each complex is evolved according to the competitive complex evolution algorithm, recombined and sorted in the same population, where the convergence is checked. The initial set of random points represents a potential location of the global optimum of the objective function. The worst point in the ranked population is substituted through statistical processes (reflection, contraction of mutation), and the process is repeated with the choice of others subcomplexes. When the points population individuate the location of the minimum of the objective function, the convergence is reached (*Duan et al., 1994*).

According to the number of parameters to be calibrated, the modeler has the possibility to set some input variables to increase the performance of the calibration: initial number of complexes, number of points in each complex, maximum relative objective function change over the iterations, etc..

The first trial of SCE-UA parallel calibration was done using the version implemented in PEST, but than it was decided to use a Matlab script to run the calibration in series. Only these results will be considered. As already mentioned, only the mesh cut at the unconfined aquifer has been used for this purpose.

4.3 Calibration with FeFlow and CATHY

After many calibrations attempts it was decided to use FeFlow as a support for the CATHY model. The main reason of this choice is that FeFlow, having already implemented PEST (FePEST) allows users to easily implement the pilot points methods, which in CATHY would have required too much time.

Figure 37 shows the location of the 28 wells used for the calibration process.

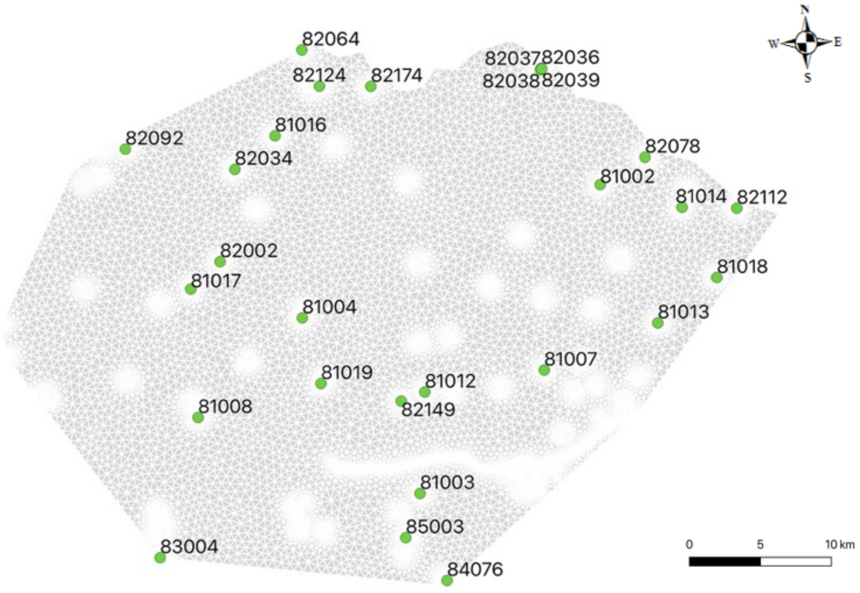

Figure 37: Location of the wells used for the calibration process.

Figure 38 shows the scatter plot obtained by the domain cut below the unconfined aquifer, with flat bottom and non-calibrated field of hydraulic conductivity. It is possible to see that more than half of the wells water head is overestimated, and for more or less 1/3 or simulated data are quite far from the observed data. The resulting RMSE is equal to 27.02 m.

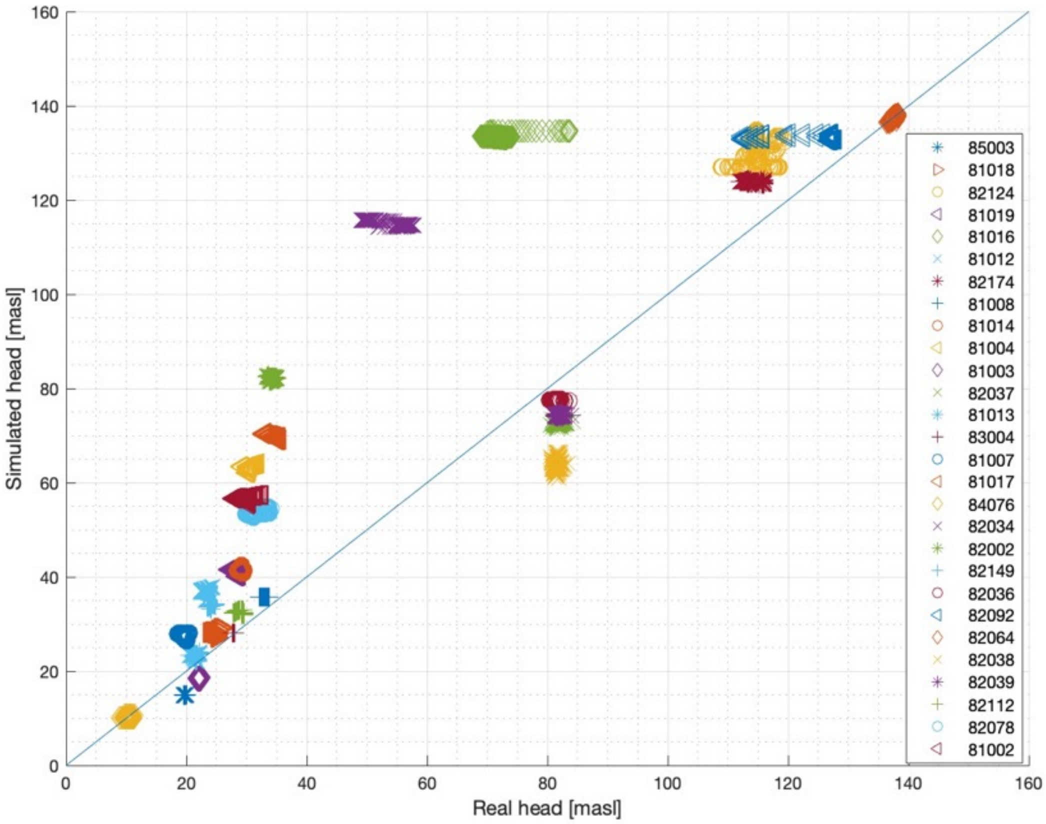

Figure 38: Scatter plot observed vs simulated hydraulic head for the configuration with non-calibrated Ks and flat bottom. RMSE = 27.02 [m].

4.3.1 First FePEST calibration: bottom and homogeneous *ks*

The first calibration step was performed in FeFlow. To obtain a more realistic domain configuration it was decided to calibrate the bottom of the domain, i.e. the bottom of the unconfined aquifer. Up to now two different bottom configurations were used: i) bottom parallel to the surface and ii) flat bottom. A first bottom calibration, using FePEST (PEST algorithm implemented in FeFlow), was performed, with the following characteristics:

- 2D steady state model in non-irrigation period (i.e., the average atmospheric flux consisted of rainfall minus potential evapotranspiration, with time-averaged boundary conditions and equally time-averaged water table levels in the objective function);
- homogeneous mean *ks* field equal to 10^{-3} m/s
- minimum bottom elevation imposed -300 m a.s.l.

Since the maximum depth of the unconfined aquifer in the southern part of the study area, is around -40 m a.s.l. according to ISPRA stratigraphical data (*Dati provenienti dall'Archivio nazionale delle indagini nel sottosuolo ai sensi della Legge 464/84, ISPRA – Dipartimento per il Servizio Geologico D'Italia- Servizio GEO_APP, Roma*) a second calibration was performed with this minimum bottom elevation imposed. Again, a homogeneous *ks* was set, equal to 10^{-3} m/s.

The bottom of domain used for the next step comes from a mix of the two calibrations: in the northern part the bottom coming from the – 300 m a.s.l. bounded calibration was considered, while in the southern part the one coming from the -40 m a.s.l. bounded calibration was assumed. The line where the two bottoms intersect constitutes the line of transition from one to the other (*Figure 39*).

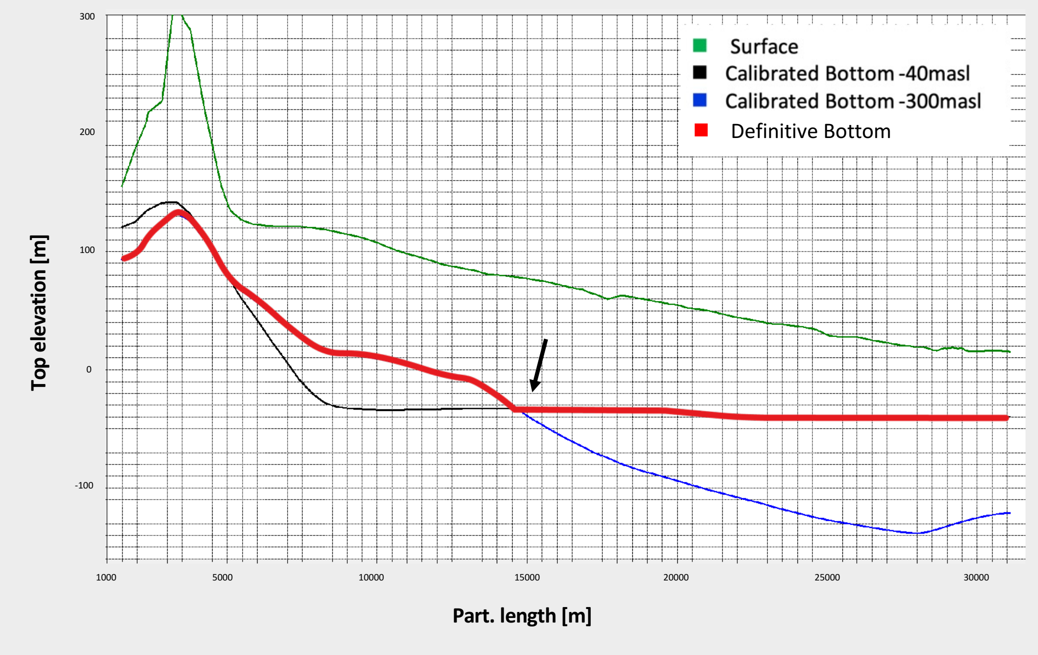

Figure 39: Calibrated bottoms and domain surface section.

Figure 39 shows how the model in the north-western side, tries to "disengage" from the boundary conditions imposed nearby, increasing the bottom level over the hydraulic head level. In the southern part, the bottom "leans" toward the imposed lower bound of -300 m a.s.l.

The spatial distribution of the aquifer bottom resulting from the FePEST calibration is shown in *Figure 40.* Consistent with available geological information, albeit qualitative, the aquifer bottom tends to increase while going from south to north, i.e., from the lowest elevations toward the high plain and the piedmont zone. Between the *risorgive* belt and the southern boundary, the elevation of the bottom is constrained to the -40 m a.s.l. bound, the average estimated elevation for the top of the first aquitard.

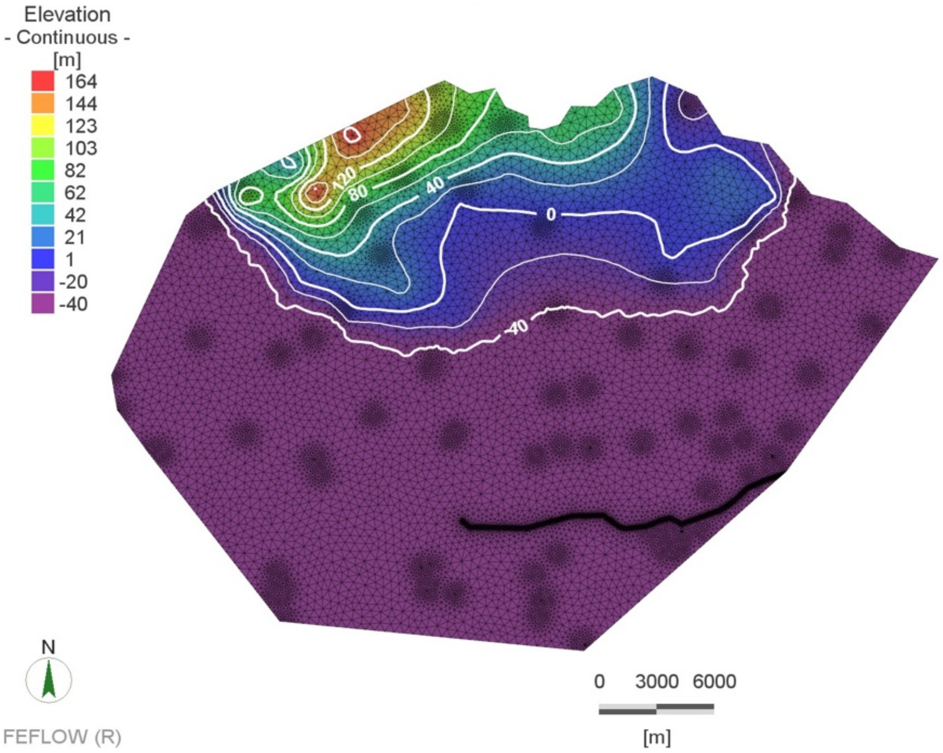

Figure 40: 3D domain with calibrated bottom.

After the bottom calibration, a first homogeneous ks calibration was performed. The output value resulting from FePest (7.18 10^{-3} m/s) was then implemented in CATHY as the aquifer hydraulic conductivity for the next step of the calibration process.

4.3.2 CATHY sensitivity analysis

The ks value obtained from the FeFlow calibration was used as a reference value for the unconfined aquifer, i.e., the whole domain except for the shallow soil (topmost three layers). Using this calibrated hydraulic conductivity in the deeper strata, a sensitivity analysis was performed in CATHY to evaluate the best value of *della permeabilità dei suoli,* from ARPAV site, gives a range of permeability (see paragraph 3.2.5). Up to now the middle value for each class was used, but to improve the simulations is necessary to choose the more suitable value. According to *Carta della permeabilità dei suoli* Zone 2 is characterized by the same soil of Zone 1 (see *Figure 22*), for this reason in the sensitivity analysis they are coupled and considered as a unique zone.

Table 9: Description of the simulation performed.

Base	Middle value of the range (deep ks = 1.0 10^{-3})
Soil_1	Minimum for Zone 1 and 2 (deep ks = 7.18 10^{-3})
Soil_2	Minimum for Zone 3 (deep ks = 7.18 10^{-3})
Soil_3	Minimum for Zone 4 (deep ks = 7.18 10^{-3})
Soil_4	Minimum for Zone 5 (deep ks = 7.18 10^{-3})
Soil_5	Maximum for Zone 1 and 2 (deep ks = 7.18 10^{-3})
Soil_6	Maximum for Zone 3 (deep ks = 7.18 10^{-3})
Soil_7	Maximum for Zone 4 (deep ks = 7.18 10^{-3})
Soil_8	Maximum for Zone 5 (deep ks = 7.18 10^{-3})

Evaluating the RMSE of each well for the nine simulations, it was possible to identify the best *ks* value of the permeability zones. In *Table 10* reports the RMSE values obtained.

Table 10: RMSE of the sensitivity analysis. In green the smallest RMSE of each well.

	Base	**Soil_1**	**Soil_2**	**Soil_3**	**Soil_4**	**Soil_5**	**Soil_6**	**Soil_7**	**Soil_8**
85003	0.507	0.180	0.507	0.495	0.507	0.620	0.507	0.522	0.506
81018	1.893	2.126	1.893	1.894	1.893	1.776	1.893	1.892	1.893
82124	4.423	4.416	4.423	4.417	4.422	4.425	4.423	4.425	4.423
81019	11.040	12.617	11.042	11.042	11.042	10.410	11.040	11.041	11.042
81016	11.915	11.829	11.915	11.814	11.916	11.938	11.916	11.943	11.915
81012	10.309	11.554	10.309	10.310	10.309	9.831	10.309	10.308	10.310
82174	4.714	4.713	4.714	4.712	4.712	4.714	4.714	4.715	4.714
81008	7.764	7.764	7.764	7.764	7.764	7.764	7.764	7.764	7.764
81014	12.128	12.555	12.128	12.128	12.128	11.933	12.128	12.126	12.128
81004	21.972	22.461	21.968	21.970	21.972	21.793	21.972	21.973	21.972
81003	1.134	0.512	1.134	1.129	1.134	1.344	1.135	1.141	1.134
82037	4.672	4.706	4.671	4.672	4.821	4.660	4.674	4.670	4.579
81013	3.545	4.345	3.544	3.551	3.545	3.337	3.545	3.539	3.545
83004	2.966	2.985	2.931	2.864	2.944	2.945	2.952	2.995	2.945
81007	8.503	9.731	8.504	8.506	8.504	8.070	8.503	8.503	8.505
81017	27.225	27.429	27.195	27.216	27.224	27.145	27.231	27.226	27.224
84076	1.362	1.378	1.363	1.364	1.363	1.357	1.364	1.362	1.363
82034	22.492	22.507	22.488	22.433	22.493	22.472	22.493	22.510	22.492
82002	29.006	29.169	28.985	28.997	29.006	28.937	29.011	29.009	29.006
82149	8.159	9.851	8.161	8.161	8.160	7.455	8.160	8.159	8.161
82036	5.023	5.044	5.020	5.020	5.084	5.014	5.024	5.021	4.994
82092	4.459	4.476	4.460	4.460	4.460	4.484	4.460	4.460	4.460
82064	0.108	0.108	0.107	0.105	0.107	0.107	0.107	0.107	0.107
82038	5.352	5.392	5.351	5.353	5.655	5.337	5.353	5.350	5.246
82039	4.381	4.404	4.379	4.379	4.444	4.372	4.383	4.379	4.318
82112	3.656	3.724	3.656	3.656	3.658	3.625	3.656	3.656	3.656
82078	22.888	23.019	22.888	22.888	22.890	22.839	22.888	22.887	22.886
81002	23.532	23.984	23.532	23.537	23.534	23.383	23.532	23.526	23.531
		Min	Min	Min	Min	Max	Max	Max	Max

After the manual sensitivity analysis, it was decided to impose in the shallow layers the “best” combination of hydraulic conductivity indicated in *Table 11* The scatter plot obtained with the calibrated bottom implementation and the data of the manual sensitivity analysis gave an improvement of the simulated results.

In *Figure 41* it is possible to see that the overestimation of the wells is still present but has been reduced, and the RMSE is equal to 23.53 m.

Table 11: Description of the permeability values.

	Base [m/s]	Minimum [m/s]	Maximum [m/s]	Best [m/s]
Aquifer	1.00E-04	-	-	7.18E-03
Moderately high	5.00E-06	1.00E-06	1.00E-05	1.00E-05
South of Sile River	5.00E-06	1.00E-06	1.00E-05	1.00E-06
Low	5.00E-08	1.00E-08	1.00E-07	5.00E-08
Moderately low	5.00E-07	1.00E-07	1.00E-06	1.00E-07
High	5.00E-05	1.00E-05	1.00E-04	1.00E-04

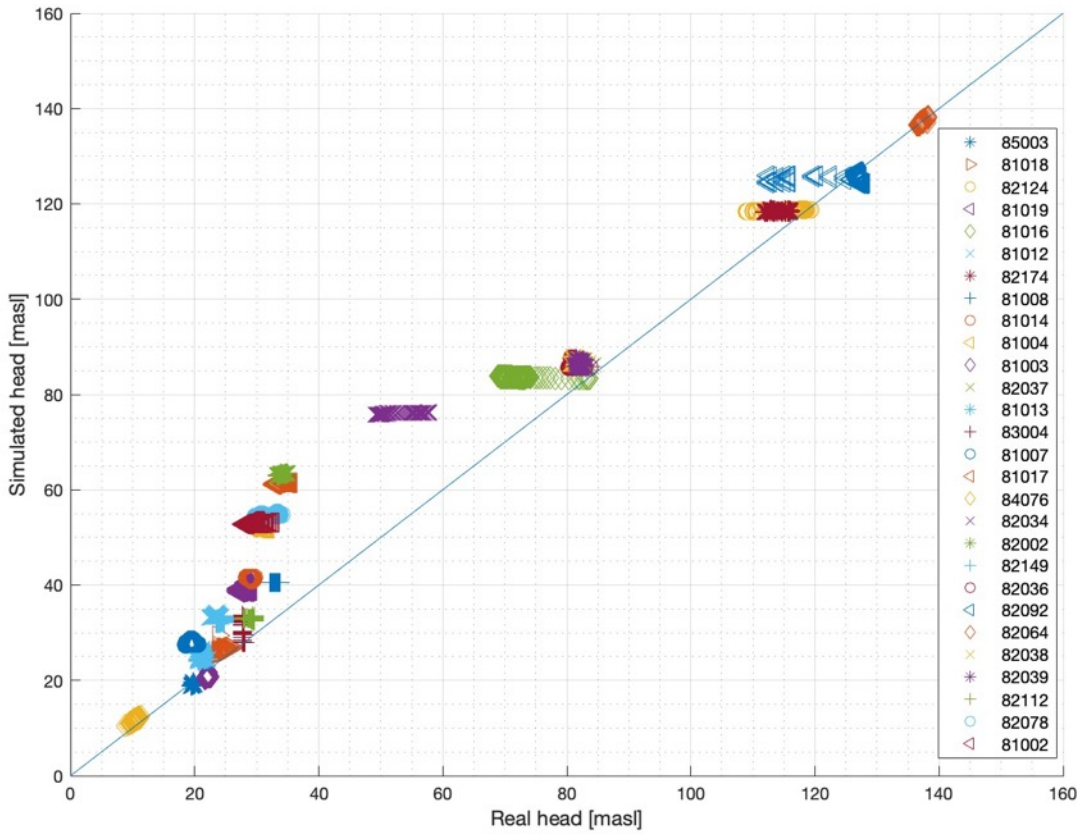

Figure 41: Scatter plot observed vs simulated hydraulic head for the configuration with sensitivity analysis Ks and calibrated bottom. RMSE = 23.53 [m].

4.3.3 Second FePEST calibration: heterogeneous *ks*

After the sensitivity analysis in CATHY, a new calibration was performed in FeFlow to further improve the match between simulated and observed water table levels, and to obtain a more realistic heterogeneous hydraulic conductivity field for the aquifer formation. Some of the Low permeability *ks* obtained from the sensitivity analysis were kept fixed in the shallowest first meter of soil, in particular the one of south of Sile River soil, low and moderately low *ks*, evidenced in yellow in *Table 11*.

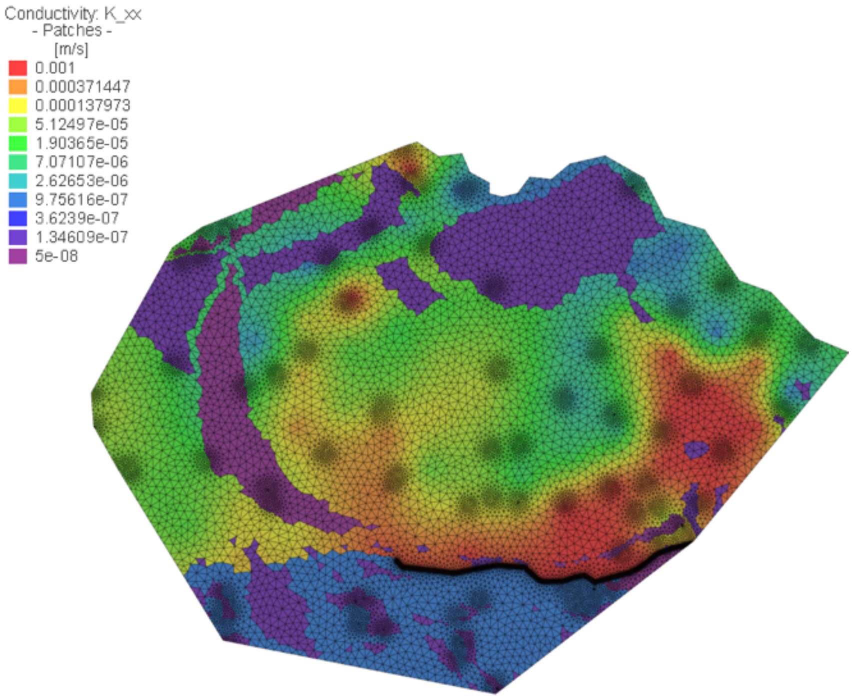

Figure 42a: Hydraulic conductivity distribution of the shallow layers (approximately first meter of soil).

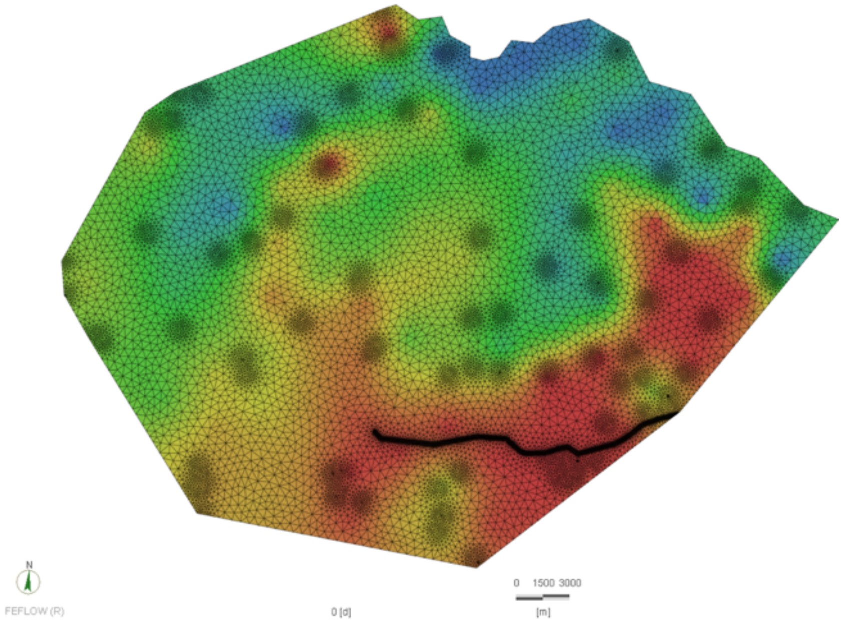

Figure 42b: Hydraulic conductivity distribution of the deep layers (below the first meter of soil).

Also in this case the calibration was performed for a 2D steady state model in non-irrigation period.

Figure 42 a and *b* represent the calibrated *ks* of the first three strata of the mesh, and the deeper layers. In red are evidenced the area with high conductivity, which covers a large fraction of the southeast of the shallow and deep domain, areas indicated in green have a conductivity in the order of magnitude of 10^{-5}, while light blue areas, in the northern part of the domain indicate lower conductivity soils.

The 3D nodal pressure head field obtained with FeFlow at the end of calibration was imposed as initial condition in CATHY.

Figure 43 shows the scatter plot of the simulation with the hydraulic conductivity field obtained by FePEST calibration, and the calibrated bottom. A reduction of the RMSE to 1/3 of the initial RMSE value in case of uncalibrated model can be appreciated. Some well's water level is still overestimated, some is underestimated but overall the differences have been strongly reduced and the model performance is satisfactory.

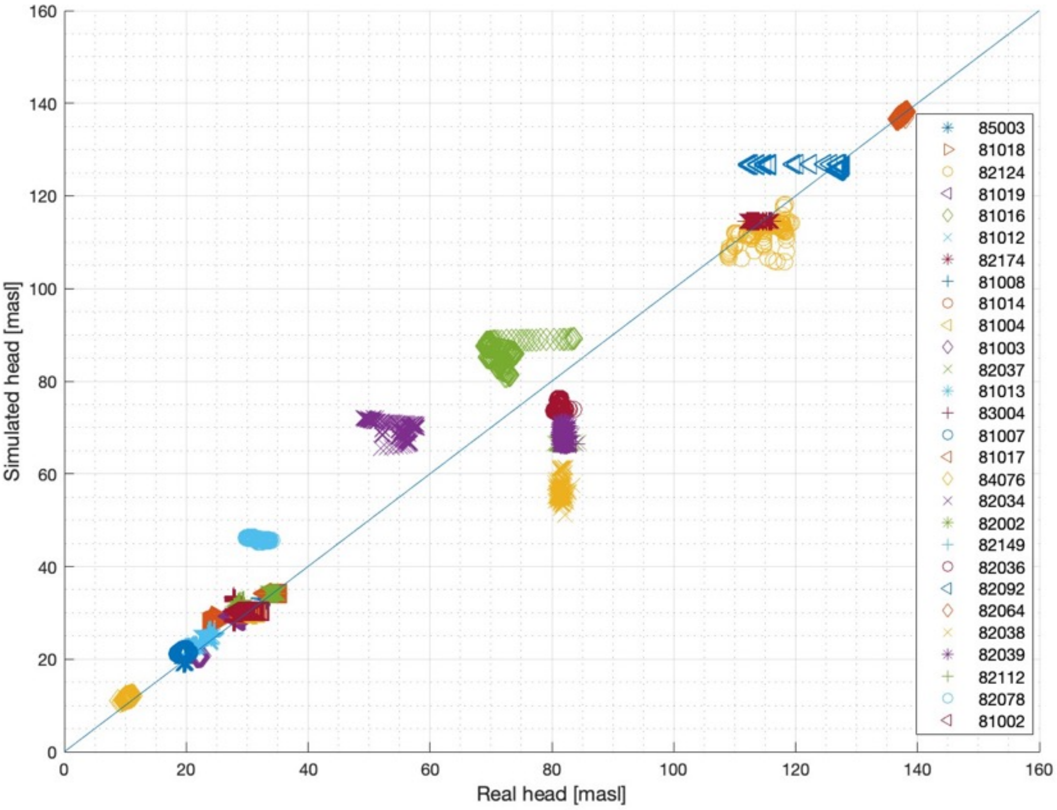

Figure 43: Scatter plot observed vs simulated hydraulic head for the configuration with FePEST ks field. RMSE = 8.18 [m].

4.3.4 CATHY SCE-UA calibration

The last step of the model calibration was performed in CATHY using the SCE-UA algorithm (*Duan et al., 1994*). This step was carried out to further improve the model and to consider transient state in the calibration, which was performed on six multiplicative parameters, α_i, for each of the soil conductivity classes from the previous FePest calibration. Note that a uniform multiplicative parameter was considered for the heterogeneous aquifer formation. The parameters were allowed to vary from 0.2 to 5. An additional multiplicative parameter was considered for anisotropy $\alpha_{\mathrm{ANISOTROPY}}$, allowed to vary from 0.1 to 1.

Table 12: Description of the permeability values.

Hydraulic conductivity	Porosity [/]	Parameter to be calibrated	Parameter calibrated
Aquifer	**0.30**	**α1**	**1.73**
Moderately high	**0.34**	**α2**	**3.15**
South of Sile River	**0.43**	**α3**	**3.14**
Low	**0.46**	**α4**	**2.60**
Moderately low	**0.39**	**α5**	**4.29**
High	**0.32**	**α6**	**2.18**
		+ $\alpha_{\mathrm{ANISOTROPY}}$	**0.24**

Figure 44 shows the scatter plot of the simulation in which the SCE-UA hydraulic conductivity field has been implemented. As for the FePEST *ks* field simulation there is a strong improvement of the results. Some of the wells also in this case have a slight under or overestimation but the overall result is rather good. The RMSE value is slightly smaller with respect to the previous simulation, with the value of 7.78 m.

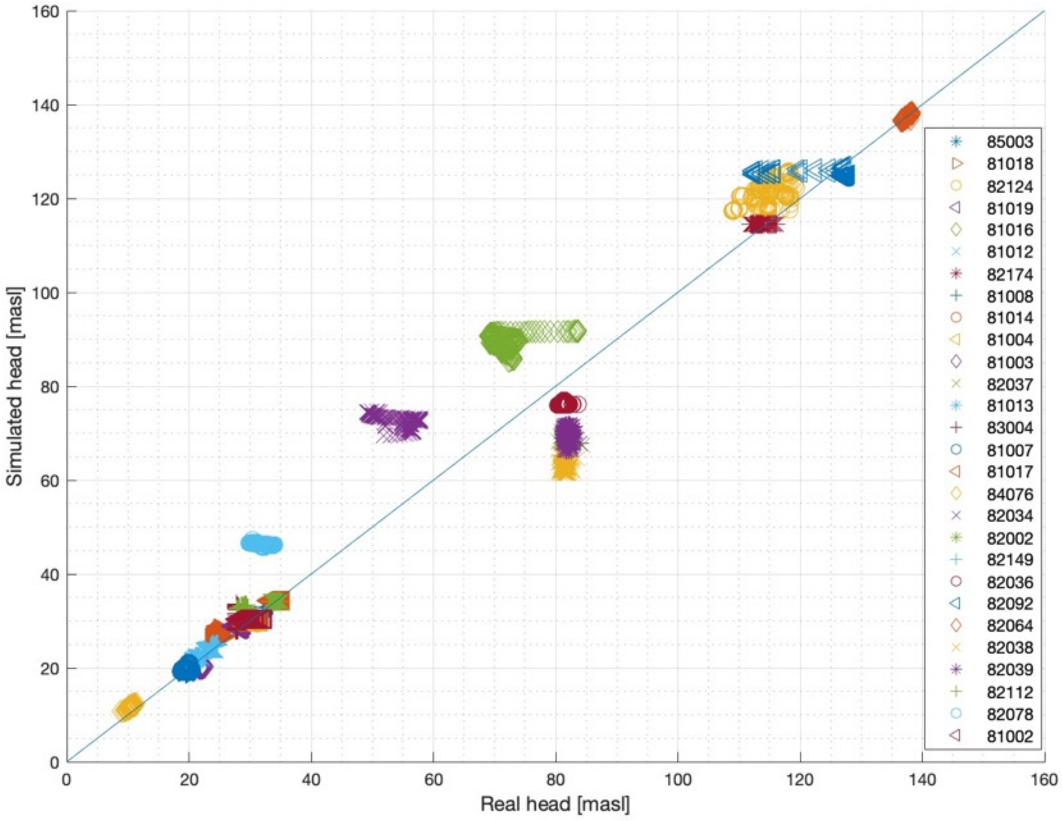

Figure 44: Scatter plot observed vs simulated hydraulic head for the configuration with SCE-UA ks field. RMSE = 7.78 [m].

4.4 Model validation and future scenario of irrigation management

After the calibration, a validation run was performed using a data set that covers a period of time that goes from the mid–- June 2019 to the end of August 2020, immediately after the period of time used for the calibration. This simulation was run using:

- calibrated bottom,
- field of hydraulic conductivity form the SCE-UA calibration,
- updated boundary conditions,
- initial conditions of pressure head coming from the end of the previous simulation,
- same 28 wells considered.

The results were evaluated again through the scatter plot and the total RMSE.

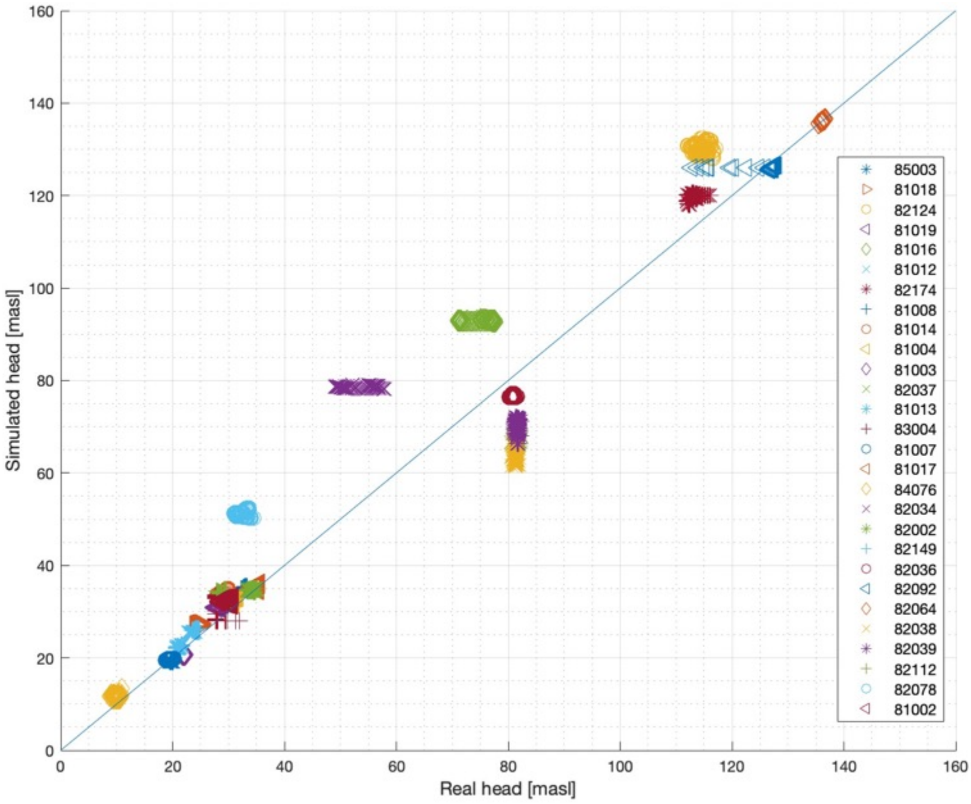

Figure 45: Scatter plot observed vs simulated hydraulic head for the validation simulation. RMSE = 9.38 [m].

In *Figure 45 it* is possible to see that the general trend of the wells water head is maintained. The RMSE slightly increases but still remains far from the non-calibrated values. Wells 81016 has a better performance, while 82174 and 82124 are a bit overestimated compared to *Figure 44*.

Having now a calibrated and validated model it was possible to perform a simulation scenario with varied irrigation. As already explained in the introduction, to fulfill the European directives the water consumptions related to the agriculture need to be reduced, for example updating the irrigation techniques. A large fraction of the study area is actually characterized by flood irrigation, which requires a large amount of water, in the particular case withdrawn from the Piave river. Since this technique is considered no more sustainable, within some years in these areas there will be a switch from flood irrigation to sprinkler irrigation. In an integrated surface–subsurface perspective it is interesting to evaluate and assess the quantitative impact that land management balance variation could have on the groundwater recharge.

The analysis started building the rating curve of the Piave river, with the data of flow rate and water head in the station of Segusino, available from the ARPAV site (https://wwwold.arpa.veneto.it/bollettini/storico/2020/0327_2020_PORT.htm), shown in *Figure 46*.

In this figure, the mean flow rate of June is highlighted, from which the irrigation demand was assumed as already derived from the Piave river.

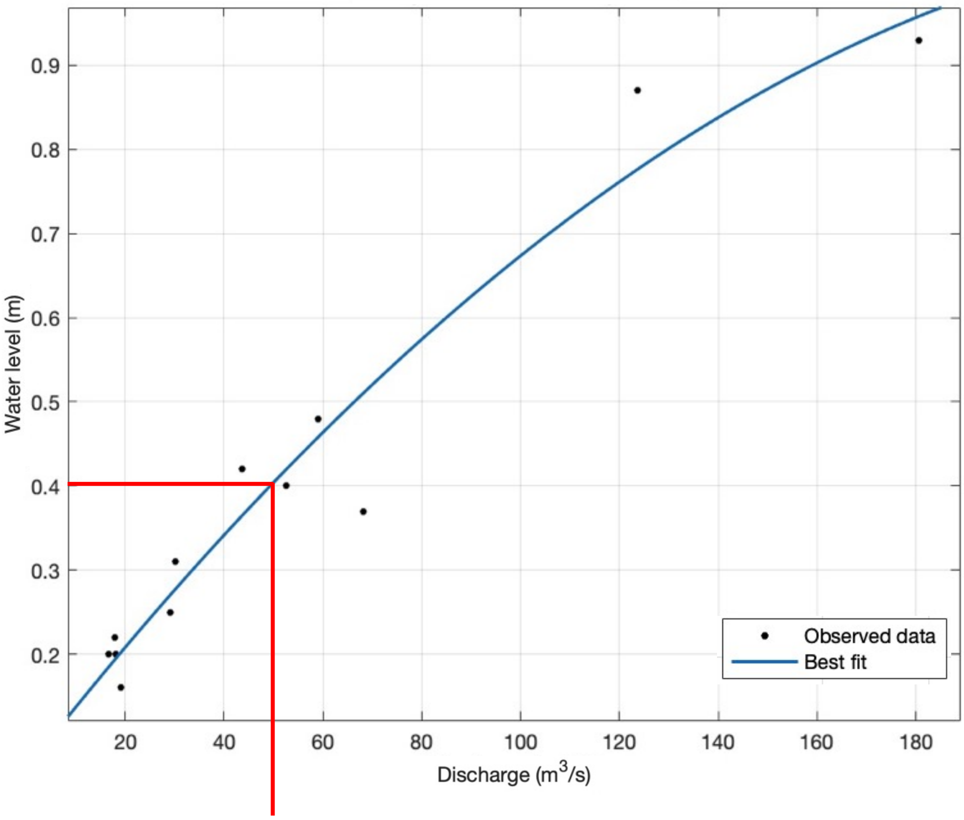

52.7 m^3/s = mean flow rate of June

Figure 46: Piave rating curve. Data from Segusino station.

The next step was the quantification of the difference between the flood irrigation discharge and the sprinkler irrigation discharge. The values of discharge were furnished by *Consorzio di Bonifica Piave.*

Flood irrigation discharge: 1.86 l/s * ha

Sprinkler irrigation discharge: 0.62 l/s * ha

1.86 l/s * ha – 0.62 l/s * ha = 1.24 l/s * ha

1.24 l/s *ha * 25000 ha = 31 m^3/s

The difference between the two discharges was then multiplied by the area at the moment interested by flood irrigation, to obtain a flow rate value that corresponds to the flow rate that would not be derived from Piave in case of sprinkler irrigation only. This value, 31 m^3/s, was used to find an estimation of the Piave water head increase, as shown in *Figure 47*.

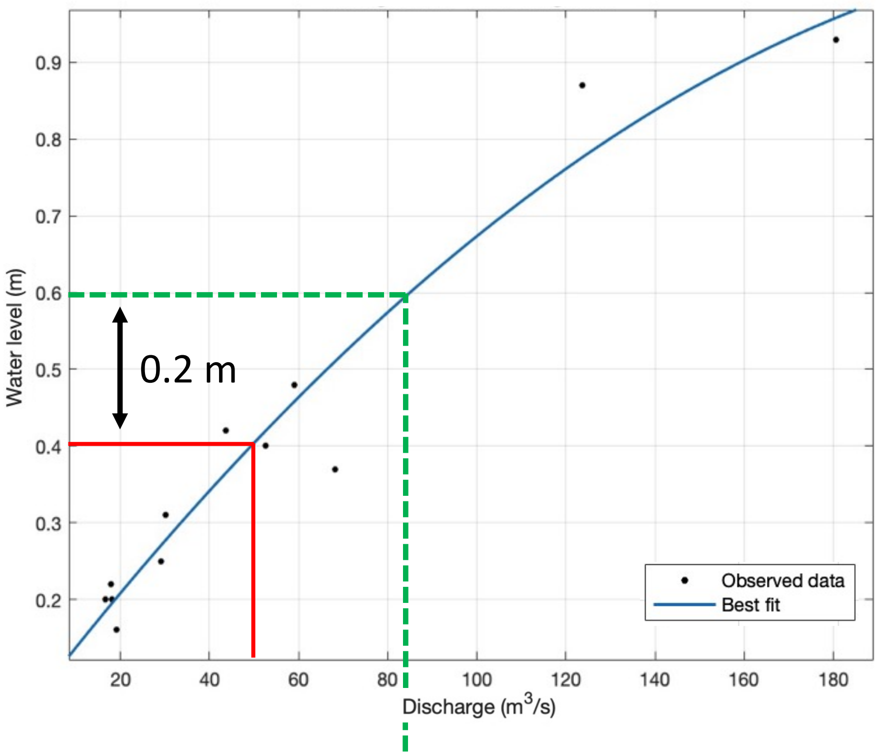

52.7 + 31 = 83.7 m^3/s

Figure 47: Rating curve – Piave Segusino station. Water head increase, due to the irrigation variation technique.

The Piave level increase together with the irrigation fluxes, were used to modify the model boundary conditions, to run the new simulation.

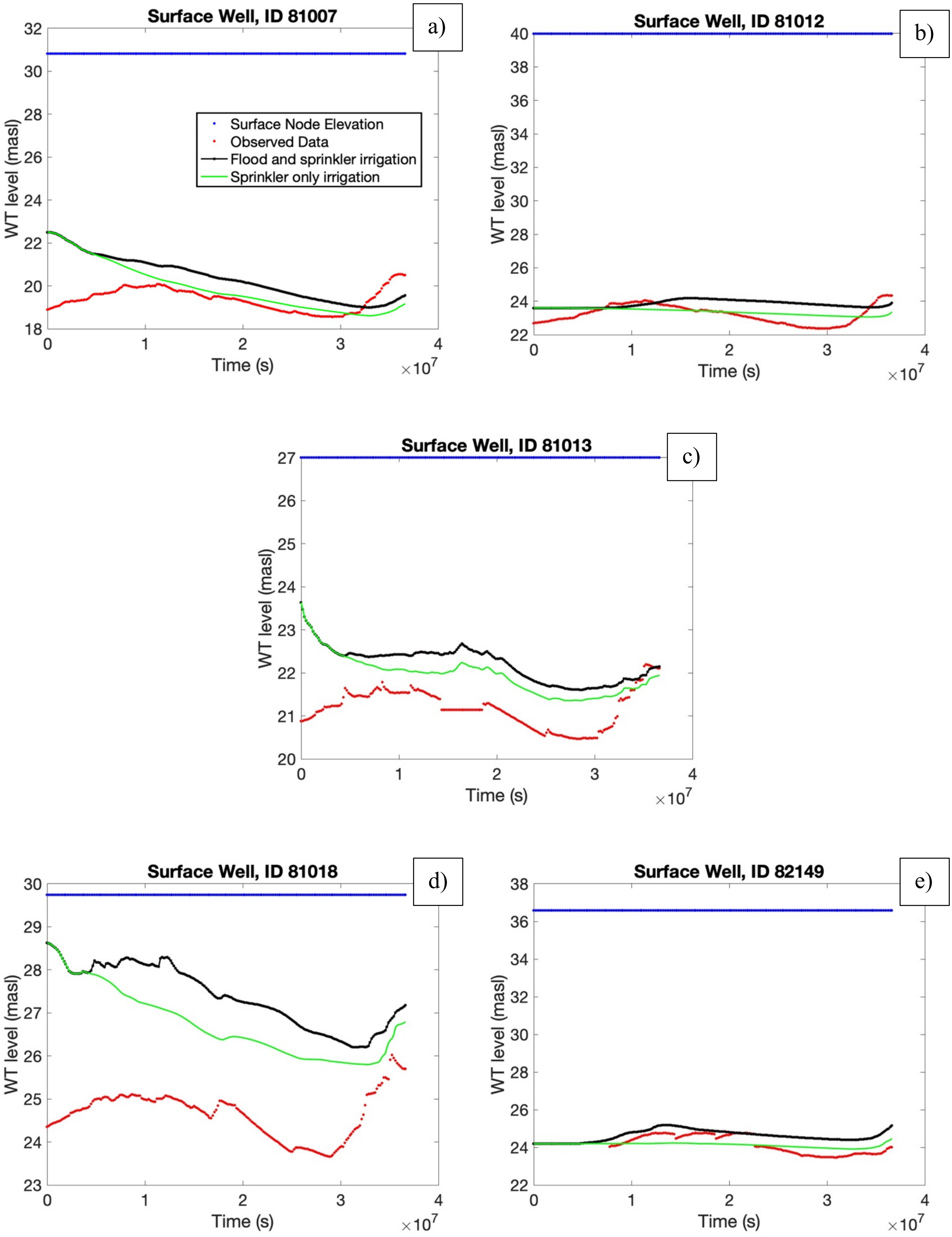

Figure 48: Water level of the irrigation variation scenario.

From the panels of *Figure 48* it is possible to see the water level difference of the wells most affected by the irrigation technique variation. The red line indicates the time series of the observed data, in black the time series of the simulation with sprinkler and flood irrigation, while in green the time series of sprinkler irrigation only simulation. These five observation wells, all located within the region affected by the irrigation management change, show a marked decrease of water table during the irrigation season compared to the reference simulation, as it was expected. Water table levels in observation wells 81003 and 81019, at the west border and south of the current flood irrigation area, respectively, were also affected (not shown), but much less than the other five.

Figure 49 shows the irrigation map. In light blue the areas where currently sprinkler irrigation is applied, while in red the areas where flood irrigation is applied. The wells with detectable variations in the water table level are highlight with a circle.

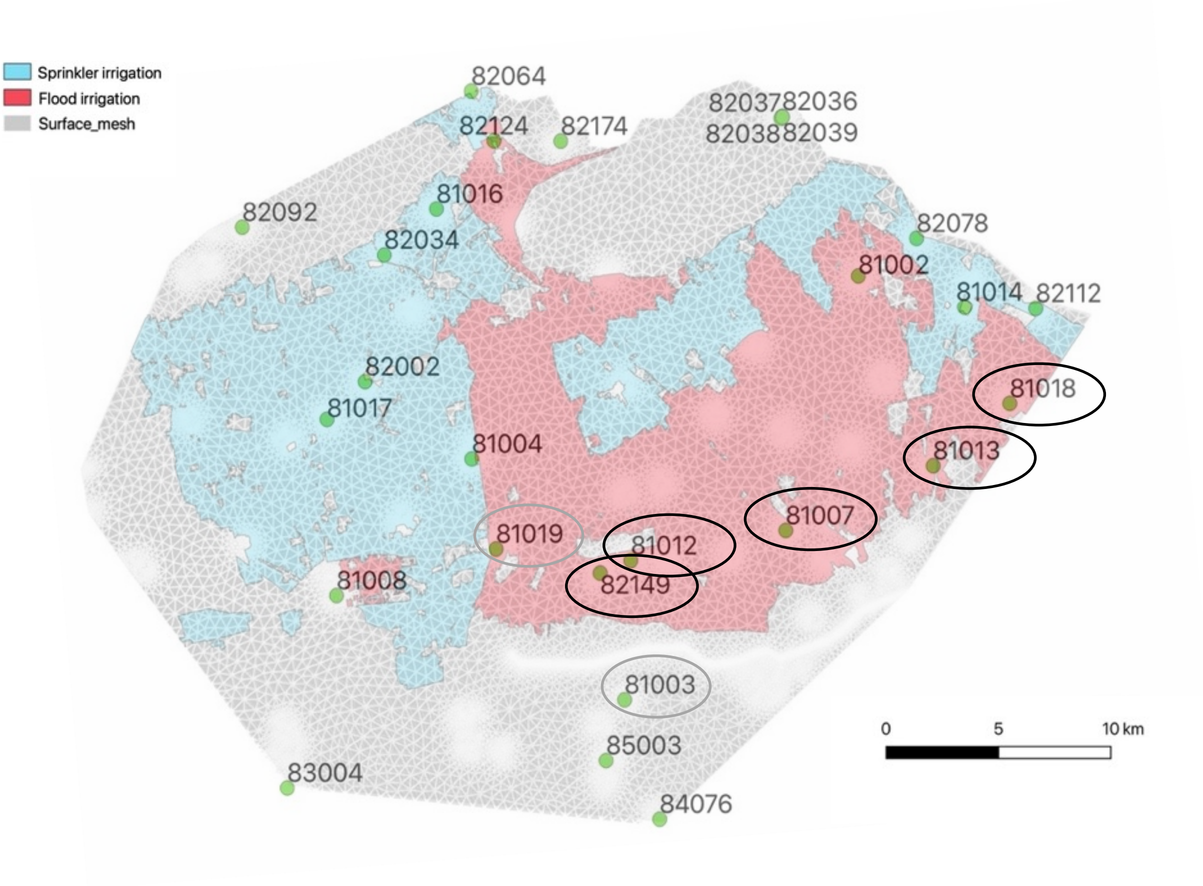

Figure 49: Location of the wells interested by the water level variation.

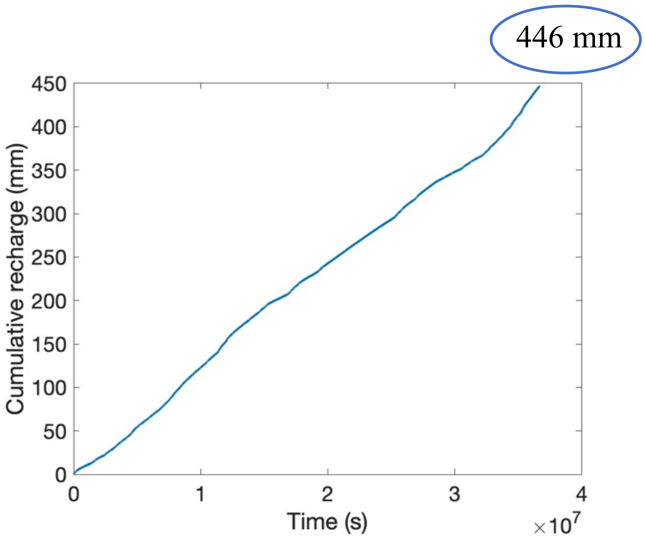

Figure 50: Total cumulative recharge (mm). Sprinkler and flood irrigation simulation.

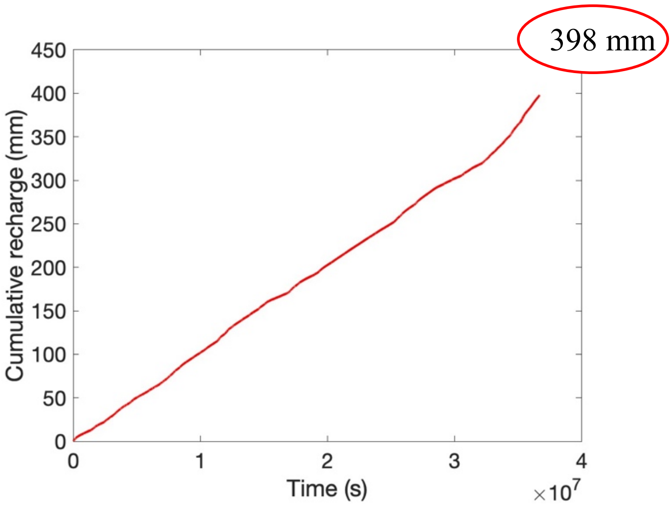

Figure 51: Total cumulative recharge (mm). Sprinkler irrigation only simulation.

The relative difference in the cumulative recharge between the two simulations (in *Figure 50 and 51*) is about 10%. This result, although preliminary, suggests that significant savings in irrigation water are not associated to substantial decreases in groundwater recharge, at least in the short term. This result can be explained by the map of the mean spatial recharge over the domain (*Figure 52*). The areas characterized by the higher recharge are not the ones where flood irrigation is applied, but the ones with a higher hydraulic conductivity.

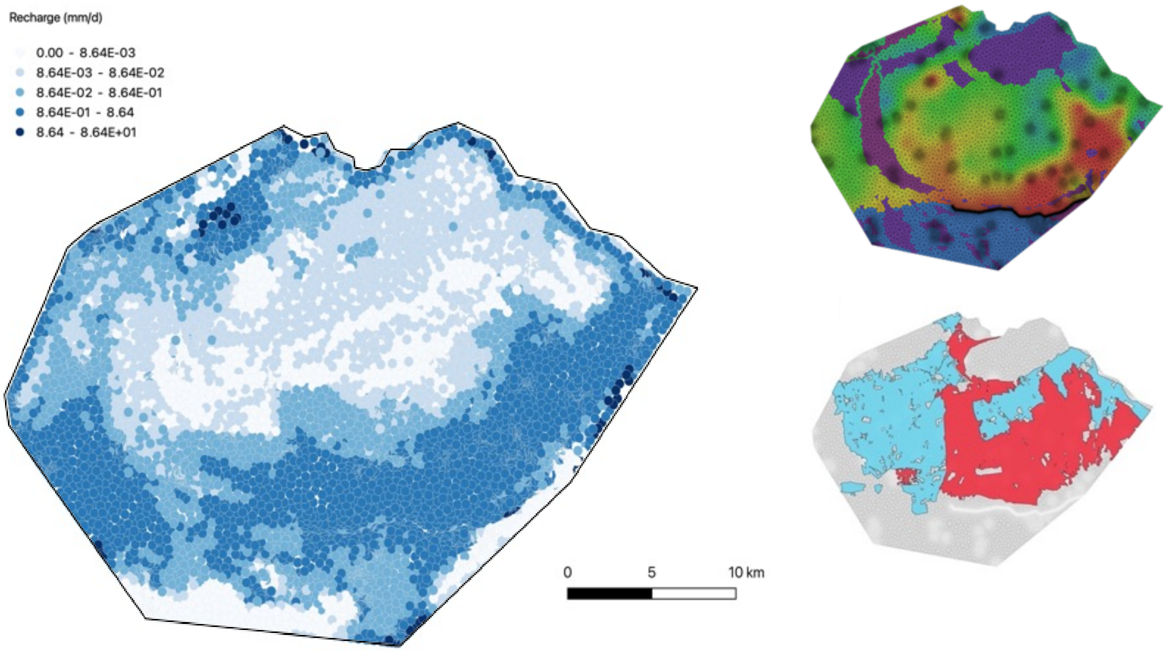

Figure 52: Mean spatial recharge [mm/d], time interval 2018/04/15 - 2019/06/15.

The simulations run up to now were characterized by a capillary water curves' parameters homogeneous for all the hydraulic conductivity classes and along the vertical direction (in *Table 13* "Initial homogeneous values"). This was done to speed up the simulations. To understand if this assumption was not appropriate a simulation was performed assigning proper Van Genuchten values to each *ks* class, starting from the porosity value, obtained from *Carsel and Parrish (1988)*.

Table 13: Description of the permeability values.

Hydraulic conductivity	Porosity [/]	Capillary retention curve exponent	Residual water content	Water retention parameter 1/α [m]	
Initial homogeneous values	**-**	**1.88**	**0.065**	**0.1429**	
Aquifer	**0.30**	**1.88**	**0.065**	**0.1429**	
Moderately high	**0.34**	**1.89**	**0.065**	**0.13**	Sandy loam
High	**0.32**	**1.89**	**0.065**	**0.13**	
South of Sile River	**0.43**	**1.56**	**0.078**	**0.28**	Loam
Low	**0.46**	**1.31**	**0.095**	**0.53**	Clay loam
Moderately low	**0.39**	**1.31**	**0.095**	**0.53**	

The introduction of these Van Genuchten parameters has almost no impacts on the simulation results. The total cumulative recharge from 446 mm of the homogeneous case becomes 445 mm, *Figure 53*, and also the mean spatial recharge map remains unchanged, *Figure 54*.

The main difference between the two cases is that the time of the simulation considerably increases, being six time longer (8 hours vs 48 hours).

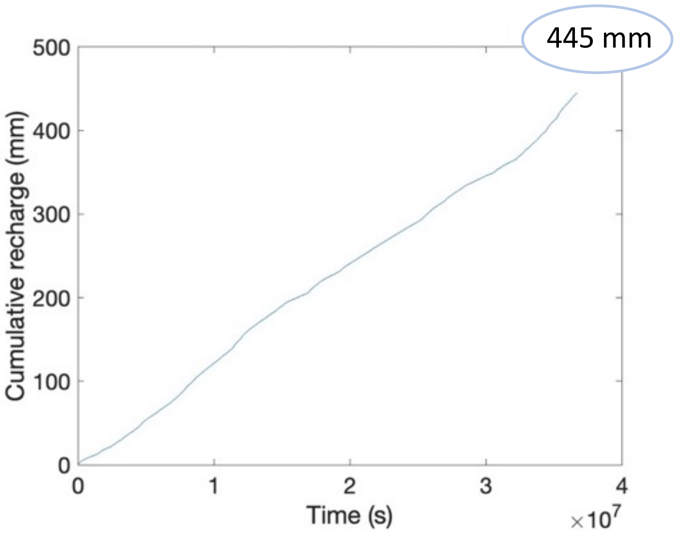

Figure 53: Total cumulative recharge (mm). Sprinkler and flood irrigation simulation, with modified Van Genuchten parameters.

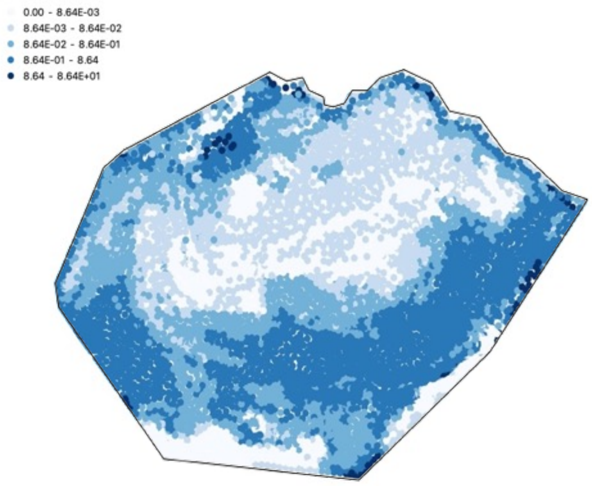

Figure 54: Mean spatial recharge [mm/d], time interval 2018/04/15 - 2019/06/15, with modified Van Genuchten

5. CATHY numerical dispersion error analysis

This section of the thesis presents a study performed on CATHY to quantify the numerical errors affecting the simulation of solute transport. This preliminary investigation is a necessary step in view of future solute transport simulations in the study area.

In fact, due to lack of time, it was not possible to proceed with studies of vulnerability to contamination. This investigation provides important indications for future applications of the model for the delineation of wellhead protection areas, where even small errors due to numerical dispersion can result in large overestimations of the contaminant plume. Moreover, this study resulted in a publication in Advances in Water Resources (*Gatto et al., 2021*). In the following, the study is reported as published.

5.1 Abstract

Integrated surface–subsurface hydrological models (ISSHMs) are increasingly being used for the assessment of contaminant transport in the environment, in addition to their more common use in water flow applications. However, the subsurface solute transport solvers in these models are prone to numerical dispersion errors. Numerical dispersion is a well-known issue in groundwater modeling, but its impacts on the results of ISSHM simulations are still poorly understood. In this study, the CATchment HYdrology (CATHY) model is used to assess the potential impacts of numerical dispersion on the simulation of coupled surface–subsurface solute transport. We first simulate the subsurface transport of a nonreactive tracer in two soil column test cases (1D and 3D) with known analytical solutions. The subsurface solute transport solver in CATHY adopts a computationally efficient time-splitting technique whereby the advection component of the governing equation is solved on elements and the hydrodynamic dispersion component is solved on nodes. Comparison between simulation results and analytical solutions with different mesh discretizations and different values for the hydrodynamic dispersion coefficients allows for accurate quantification of the numerical dispersion error and yields insights into the parameters and other factors that control it. It is shown that, taken alone, the advection and dispersion solvers are very robust, but their combination can result in significant numerical dispersion, stemming from the exchange of concentration information from elements to nodes and vice versa in the time-splitting procedure. The tests also show that these errors can be kept under control by ensuring that the grid Péclet number is in the range 0.5-1.0 or smaller. We then apply CATHY in a third test case involving two synthetic hillslopes (concave and convex) in fully coupled surface–subsurface mode, in order to examine the impact of this subsurface numerical dispersion on simulated streamflow hydrographs, in particular with reference to pre-event water contributions to runoff. Here as well the results show that the effect of numerical dispersion can be controlled by keeping the grid Péclet number sufficiently small. This work provides a new set of benchmark test cases for integrated surface–subsurface hydrological models, extending to solute transport the flow-only suite of benchmarks recently published in two intercomparison studies.

5.2 Introduction

Contaminant transport in aquifers is a relevant environmental issue, given that most of the Earth's readily available freshwater is found in the subsurface (*Poeter et al., 2020*). Numerical models of groundwater flow and solute transport are thus fundamental tools for sustainable water resources management, thanks to their ability to simulate the spatiotemporal evolution of contaminant plumes in a broad range of scenarios with variable external forcing, including climate change and land use change. However, numerical models can be affected by significant uncertainties, typically due to an imperfect knowledge of model parameters and initial and boundary conditions, as well as errors, due to their inherent spatiotemporal approximations. One type of numerical error that can have a large impact on the accuracy of a model is numerical dispersion. This is a well-known problem (*e.g., Noye and Hayman, 1985; Gresho and Sani, 1998; Woods et al., 2003*) that potentially leads to erroneous transport equation solutions that are characterized by a degree of solute spreading greater than that ascribable to the hydrodynamic dispersion coefficients. In the case of reactive contaminants, numerical dispersion can also lead to an overprediction of the degradation process because of artificial mixing of the considered pollutants (*Bause and Schwegler, 2012*).

Numerical dispersion is generally introduced into a model through stabilization techniques such as upwind schemes, whose aim is to reduce sharp-front oscillations in the solution, at the expense however of added mass spreading. This issue has been investigated in detail in several studies that assess the numerical dispersion arising from different discretization methods (e.g., *Radu et al., 2011)* or that propose techniques to alleviate this error (e.g., *Suciu et al., 2013; Wu et al., 2019; Pathania et al., 2020).* Despite its recognized importance, however, numerical dispersion in groundwater solute transport modeling has received little attention in the water resources literature, and it is seldom discussed as a potential source of error in modeling applications (*Watson and Barry, 2001; Woods et al., 2003*).

Recently developed integrated surface–subsurface hydrological models (ISSHMs), such as CATchment HYdrology (CATHY; *Camporese et al., 2010*), HydroGeoSphere (HGS; *Brunner and Simmons 2012*), and MIKE SHE (*Long et al., 2015*), are being increasingly used not only for catchment-scale flow applications but also for coupled simulations of solute transport in the surface–subsurface continuum (e.g., *Liggett et al., 2015; Scudeler et al., 2016b; Daneshmand et al., 2019; Gatel et al., 2019*). ISSHMs typically simulate subsurface flow by means of the 3D Richards equation or a combination of 1D Richards and 3D saturated groundwater flow equations, coupled with some approximation of the shallow water equations for surface runoff and channel flow. The computed subsurface and surface velocity fields are then applied to solve the advection–dispersion (and sometimes reaction) equations in the corresponding domains, thereby providing a holistic approach to flow and solute transport modeling at the catchment or hillslope scale. MIKE SHE, for instance, was recently applied to a semi-arid catchment in southwestern Victoria, Australia, for studying salinity issues and their possible future evolution due to climate change (*Daneshmand et al., 2019*); HGS was applied to the wetlands of the Lehstenbach catchment, in southeast Germany, characterized by high concentrations of dissolved organic carbon (*Liggett et al., 2015*); and CATHY was applied to reproduce and interpret a laboratory experiment involving the transport of both reactive solutes and conservative tracers (*Gatel et al.,* *2019)* and an experiment conducted at the Landscape Evolution Observatory (LEO) in Arizona, USA, using deuterium as a tracer *(Scudeler et al., 2016b)*. These applications demonstrate the great potential of ISSHMs as powerful tools for the simulation and analysis of real-world solute transport processes in the surface and subsurface. However, none of these studies has addressed the possible impacts that numerical dispersion may have on solute transport simulated by ISSHMs. In CATHY, for example, numerical dispersion is created not only by the model discretization, but also by the use of a time-splitting technique for the solution of solute transport in the subsurface, whereby advection is solved on the elements and dispersion on the nodes (*Mazzia and Putti, 2005*). This scheme makes the solver numerically robust and computationally efficient, but passing the computed concentration distribution back and forth between elements and nodes causes a numerical artifact that, as we will demonstrate, manifests as a particular form of numerical dispersion. For this reason, with the exception of *Scudeler et al. (2016b)*, in all previous studies of solute transport with CATHY (*Weill et al., 2011*; *Scudeler et al., 2016a*; *Gatel et al., 2019, 2020*), either the dispersion coefficients were assigned negligible values or the dispersion module was switched off.

The goals of this study are: i) to accurately quantify the numerical dispersion affecting the solute transport subsurface solver of CATHY and relate this dispersion to grid and flow characteristics; ii) to evaluate how the numerical dispersion may affect the simulation of coupled solute transport in the surface-subsurface continuum. First, the CATHY model is used to simulate two soil column test cases with known analytical solutions. The first test case represents a one-dimensional solute transport process, while the second takes into account fully three-dimensional solute plume dynamics. The comparison between numerical results and analytical solutions in a number of runs with different grid resolutions and coefficients of hydrodynamic dispersion provides a comprehensive range of conditions for the evaluation of the possible impacts of numerical dispersion in CATHY, which can by extension be applicable to other ISSHMs. In a third test case, CATHY is used to simulate the two idealized hillslopes presented in *Liggett et al. (2014)*, one with a concave profile and the other convex, in a series of coupled surface–subsurface solute transport runs. These simulations are used to compute the amount of pre-event water at the discharge outlet and to assess the impact of numerical dispersion on this runoff. The simulations are run for a scenario of no surface–subsurface mixing, i.e., with advection-only exchange of solute between the surface and subsurface, and for a scenario of perfect mixing, in which diffusive surface–subsurface solute exchange is also activated. In both scenarios, different combinations of subsurface transport parameters are analyzed.

5.3 Methods

5.3.1 Soil column test cases

The first two test cases involve water flow and solute transport in the subsurface only. The computational domain is meant to represent Darcy's experiment, i.e., a column packed with a saturated homogeneous granular medium. Two types of simulation are run: in the first test case a one-dimensional process of advection–dispersion is reproduced, while the second test case is focused on a fully three-dimensional process.

Different domain discretizations are used in the runs: a fine discretization (*mesh 0*), an intermediate one (*mesh 1*), and a coarse one (*mesh 2*). In the 1D analyses (*Table 14)*, the size of the column domain is kept fixed and equal to 0.2 [L] × 0.2 [L] for the square base and 1.0 [L] for the height. In the 3D analyses (*Table 15*), the height of the colum domain is kept fixed, together with the mesh resolutions, while the size of the square base is increased to avoid the solute plume reaching the lateral boundaries. The surface of *mesh 0* consists of square cells of size 0.01 [L] in the *x* and *y* directions, each subdivided into two triangles and then replicated vertically into 100 layers of constant thickness equal to 0.01 [L] to generate three-dimensional tetrahedral grids such as the one shown in *Figure 55*. Similarly, *mesh 1* consists of square cells of size 0.02 [L] in the *x* and *y* directions, with triangles replicated vertically into 50 layers of constant thickness equal to 0.02 [L], and *mesh 2* is formed by cells of 0.04 [L] in the *x* and *y* directions, with triangles replicated vertically into 25 layers of constant thickness equal to 0.04 [L]. Dimensionless units are used throughout these simulations for the sake of generality.

Table 14: Domain configuration for the 1D soil column test case.

Mesh	*Resolution*	*N. of vertical layers*	*Base size*	*N. of surface cells*
Simulations with advection only - Flow rate = 0.5, 1, 2 [LT^{-1}]				
Mesh 0	0.01	100	0.2 × 0.2	20 × 20
Mesh 1	0.02	50	0.2 × 0.2	10 × 10
Mesh 2	0.04	25	0.2 × 0.2	5 × 5
Simulations with advection–dispersion - Flow rate = 1 [LT^{-1}]; D_L = 0.001, 0.05, 0.1, 0.2 [L^2T^{-1}]				
Mesh 0	0.01	100	0.2 × 0.2	20 × 20
Mesh 1	0.02	50	0.2 × 0.2	10 × 10
Mesh 2	0.04	25	0.2 × 0.2	5 × 5

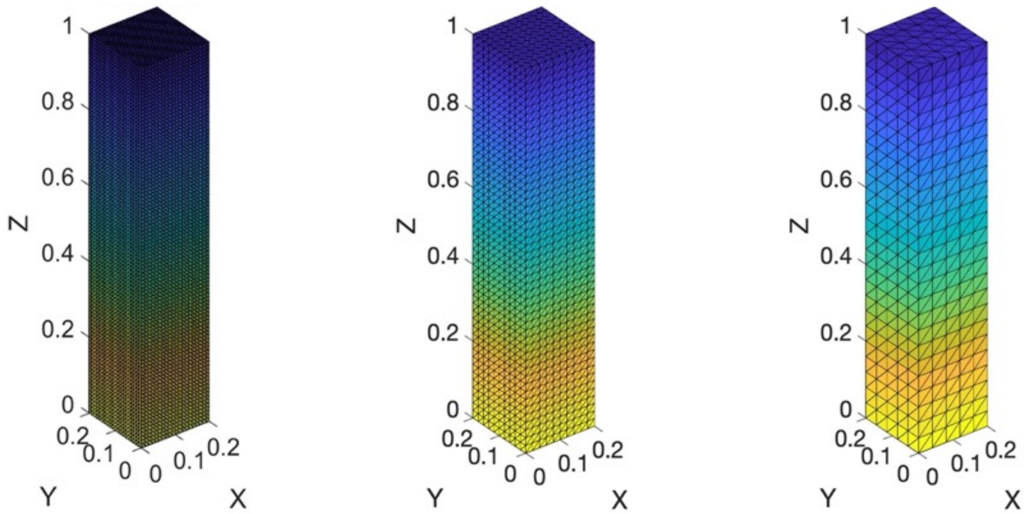

Figure 55: Different domain discretizations for the 1D soil column test case. From left to right: mesh 0, mesh 1, and mesh 2. The color scale indicates elevation, from blue (z=1) to yellow (z=0).

The time step size for the dispersion solver is kept fixed for all the simulations, with a value of 0.001 [T], while the time step size for the explicit advection solver changes according to the Courant–Friedrichs–Lewy condition, whereby a Courant number not exceeding 0.3 is prescribed (*Mazzia and Putti, 2005*). This is a core feature of the time-splitting technique implemented in CATHY to ensure numerical stability. The Courant number is expressed as $\frac{\bar{U}\,\Delta t}{\Delta x}$, where $\bar{U}$ is the Darcy flux, Δt is the advective time step size, and Δx is the characteristic element spatial scale, equal to the element volume divided by its surface area.

5.3.1.1 1D simulations

In this test case a conservative tracer with concentration $C_0 = 1$ is introduced continuously over the entire top surface of the domain, the initial concentration is zero everywhere, and a steady-state saturated flow from the top to the bottom is enforced through appropriate boundary conditions (spatially uniform inflow on the top, constant pressure head at the bottom, and no flow across the lateral sides). The resulting breakthrough curve (concentration vs time) at the column outflow is compared with the following analytical solution (*Freeze and Cherry, 1979*):

$$\frac{C}{C_0} = \frac{1}{2}\left[\operatorname{erfc}\left(\frac{L-\bar{v}t}{2\sqrt{D_L t}}\right) + \exp\left(\frac{\bar{v}L}{D_L}\right)\operatorname{erfc}\left(\frac{L+\bar{v}t}{2\sqrt{D_L t}}\right)\right] \qquad (5)$$

where erfc is the complementary error function, L is the height of the column, $\bar{v}$ is the average linear velocity (i.e., Darcy's flux divided by the porosity of the porous medium, here equal to 0.58), and D_L is the coefficient of hydrodynamic dispersion along the flow path.

In a first series of 1D simulations, only the advective part of the CATHY solver is activated. In theory, the solution in this case would be represented by a step function (plug flow); in reality, some spreading of the breakthrough curve is expected, due to numerical dispersion. In order to quantify this error, the best fit between equation (5) and the output concentration of CATHY is used to obtain the model-estimated, or apparent, dispersion coefficient $D_L{}'$ (*Radu et al., 2011*). This is done with the three meshes and, for each mesh, for three values of the Darcy flux, equal to 0.5, 1.0, and 2.0 [LT^{-1}]. In this series of runs, since there is no hydrodynamic (physical) dispersion, the apparent coefficient $D_L{}'$ is entirely attributable to numerical dispersion.

In a second series of 1D simulations, the dispersion part of the CATHY subsurface transport equation is activated. For each mesh, four simulations are performed with a unitary input flow and different values of the hydrodynamic dispersion coefficient D_L, equal to 0.001, 0.05, 0.1, and 0.2 [L^{2}T^{-1}], corresponding to grid Péclet numbers, $Pe = \frac{\bar{v}\,\lambda}{D_L}$, that range from 68.97 to 0.09, where λ is the element size. High values of *Pe* generally lead to high numerical dispersion. Simulations with *Pe* > 2 are purposefully considered here to test and quantify the numerical dispersion in CATHY. Once again, equation (5) is fitted with the output concentration of CATHY, in order to estimate the apparent dispersion coefficient $D_L{}'$.

5.3.1.2 3D simulations

In this test case a slug of tracer mass equal to 0.01 [M] is introduced over a single time step (0.001 [T]) at the central node of the surface layer, to approximate an instantaneous pulse injection. Compared with the 1D simulations, the 3D analyses require a modification of the computational domain, because for an accurate assessment of the transverse dispersion it is necessary to keep the solute far from the lateral boundaries. For this reason, the height of the soil column is kept fixed at 1.0 [L], while the square base is increased as reported in *Table 15*. The cell resolution (0.01 [L], 0.02 [L], and 0.04 [L] for *mesh 0*, *1*, and *2*, respectively) as well as the vertical discretization are the same as in the first test case.

As in the 1D test case, the mass of solute is carried away from the point of injection by transport in a steady-state uniform flow field moving in the z-direction. However, the concentration distribution is now fully 3D and can be expressed analytically by the following equation (*Freeze and Cherry, 1979*):

$$C\,(x, y, z, t) = \left(\frac{M}{8(\pi t)^{3/2}\sqrt{D_x D_y D_z}}\right)\exp\left(-\frac{X^2}{4D_x t} - \frac{Y^2}{4D_y t} - \frac{Z^2}{4D_z t}\right) \qquad (6)$$

where M is the mass of the tracer introduced at the central node of the surface and D_x, D_y, and D_z are the coefficients of hydrodynamic dispersion in the x, y, and z directions, respectively. The center of gravity of the tracer cloud lies at $X = 0$, $Y = 0$, and $Z = 0$, where $X = x - x_0$ and $Y = y - y_0$, with x_0 and y_0 being the x and y coordinates of the node at which the mass is introduced, and $Z = z - \bar{v}t$, with $\bar{v}$ the average linear velocity as defined for the 1D test case. In the 3D test case, the Darcy flux is 10 times larger than in the 1D case, in order to achieve a significant spreading of the solute plume within a short simulation of duration 0.025 [T]. The apparent dispersion coefficients D_L' are again estimated by fitting the analytical solution to the numerical results. To estimate these dispersion coefficients in the three directions, it is sufficient to quantify the concentration distribution standard deviations, σ_x, σ_y, and σ_z, as these are related to (generic) dispersion coefficients D_x, D_y, and D_z according to: $\sigma_x = \sqrt{2D_x t}$, $\sigma_y = \sqrt{2D_y t}$, $\sigma_z = \sqrt{2D_z t}$ (*Freeze and Cherry, 1979*).

The first series of 3D simulations is carried out with the dispersion solver activated, but using a negligible value for the coefficients of hydrodynamic dispersion (1.0×10^{-9} [L^2T^{-1}]), equal in the three directions. This is done in order to highlight the particular influence of the element-to-node and node-to-element exchange of information, which only takes place when the dispersion module is switched on. For each mesh, three values of Darcy flux are investigated, equal to 5.0, 10.0, and 20.0 [LT^{-1}].

In the second series of 3D simulations, the input longitudinal (z direction) hydrodynamic dispersion values are 0.05, 0.1, 0.2 and 0.5 [L^2T^{-1}], with a fixed anisotropy ratio $D_z/D_{x,y}$ equal to 5. The Darcy flux for these simulations is 10 [LT^{-1}].

Table 15: Domain configuration for the 3D soil column test case.

Mesh	***Resolution***	***N. of vertical layers***	***Base size***	***N. of surface cells***
Simulations with negligible physical dispersion **Flow rate = 5, 10, 20 [LT^{-1}]**				
Mesh 0	0.01	100	0.2 × 0.2	20 × 20
Mesh 1	0.02	50	0.4 × 0.4	20 × 20
Mesh 2	0.04	25	0.8 × 0.8	20 × 20
Simulations with advection–dispersion **Flow rate = 10 [LT^{-1}]; D_L = 0.05, 0.1, 0.2, 0.5 [L^2T^{-1}]**				
Mesh 0	0.01	100	0.4 × 0.4	40 × 40
Mesh 1	0.02	50	0.8 × 0.8	40 × 40
Mesh 2	0.04	25	1.6 × 1.6	40 × 40

5.3.2 Hillslope simulations

The third test case aims to simulate fully coupled surface–subsurface processes in the two idealized hillslopes of *Liggett et al. (2014),* the first with a concave surface and the second convex (*Figure 56*). The length of the domain is 20 m, the width is equal to 1 m, and the height ranges from 8 m to approximately 10 m. In both hillslopes, the surface is discretized into 5 × 100 grid cells (i.e., cells of size 0.2 m in the horizontal directions), while the subsurface is discretized vertically into 40 layers, with thicknesses ranging from 0.04 m at the top to about 2 m at the bottom. The layers are parallel to the surface except for the last one, which has a flat base (*Figure 56*). In these simulations we use real metric units in order to be consistent with *Liggett et al. (2014)*. Moreover, we intentionally use a coarser grid, to keep the computation time small and highlight the high CPU efficiency of the time-splitting technique implemented in CATHY.

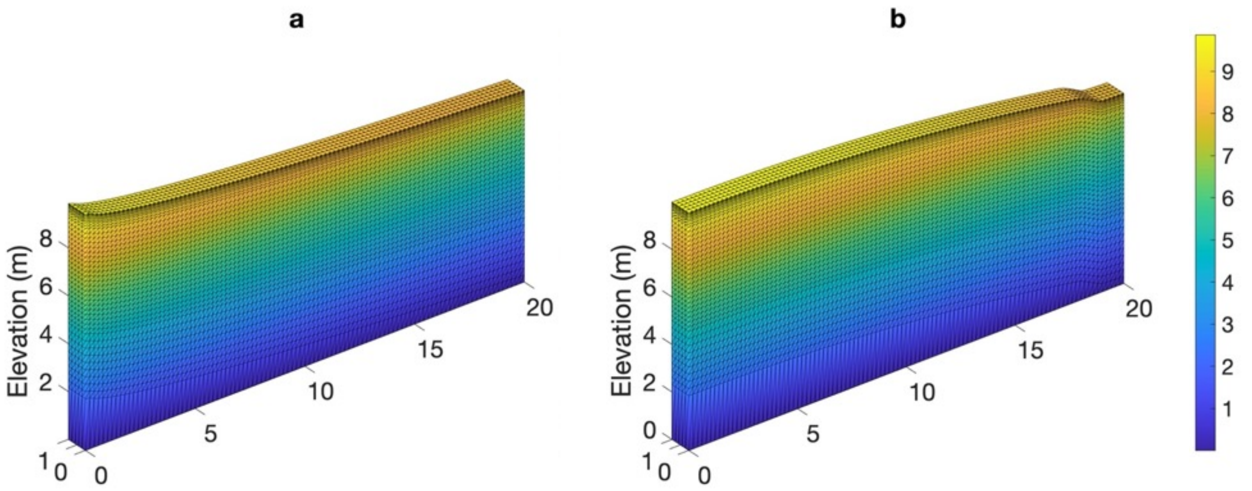

Figure 56: Three-dimensional finite element grids for a) the concave hillslope and b) the convex hillslope. The color bar indicates elevation in m.

No-flow boundary conditions are applied for both hillslopes at the bottom and sides of the domain, while the initial hydraulic head distributions were determined by running each hillslope model to steady state under a constant precipitation rate of 1 mm year^{-1}. Then, a 1-h long rainfall event with precipitation rate equal to 20.8 mm h^{-1} is applied over the hillslopes, followed by a 1.4-h long recession phase. The soil is homogeneous and isotropic, with hydraulic properties as reported in *Table 16.*

Table 16: Model parameters for the hillslope test case.

<table>
<tr><td colspan="5"><i>Fixed parameters</i></td></tr>
<tr><td><i>Porosity</i></td><td colspan="4">0.41</td></tr>
<tr><td><i>Saturated hydraulic conductivity</i></td><td colspan="4">1.23×10^{-5} m s^{-1} (44.2 mm h^{-1})</td></tr>
<tr><td><i>van Genuchten α</i></td><td colspan="4">7.5 m^{-1}</td></tr>
<tr><td><i>van Genuchten n</i></td><td colspan="4">1.89</td></tr>
<tr><td><i>Residual water content</i></td><td colspan="4">0.159</td></tr>
<tr><td><i>Specific storage</i></td><td colspan="4">1.0×10^{-4} m^{-1}</td></tr>
<tr><td><i>Manning roughness coefficient</i></td><td colspan="4">0.05 s m $^{-1/3}$</td></tr>
<tr><td colspan="5"><i>Scenario parameters</i></td></tr>
<tr><td><i>Level of physical dispersion</i></td><td><i>Very low</i></td><td><i>Low</i></td><td><i>Intermediate</i></td><td><i>High</i></td></tr>
<tr><td><i>Longitudinal dispersivity α_L</i></td><td>0.1 m</td><td>0.1 m</td><td>1.0 m</td><td>10 m</td></tr>
<tr><td><i>Transverse dispersivity α_T</i></td><td>0.01 m</td><td>0.01 m</td><td>0.1 m</td><td>1.0 m</td></tr>
<tr><td><i>Diffusion coefficient D*</i></td><td>10 $^{-10}$ m^2 s^{-1}</td><td>10 $^{-9}$ m^2 s^{-1}</td><td>10 $^{-9}$ m^2 s^{-1}</td><td>10 $^{-9}$ m^2 s^{-1}</td></tr>
</table>

The main scope of this test case is to assess the impact of numerical dispersion on the simulated contribution of pre-event water to the streamflow hydrograph for different combinations of subsurface transport parameters (*Table 16*). To this aim, the rainfall water concentration is set to 1 kg m^{-3}, while the initial solute concentration in the soil is 0 kg m^{-3}. Under these conditions, the solute mass discharge at the outlet represents the contribution of event water, while the pre-event water fraction is simply assumed as its complement to the total discharge, as in *Weill et al. (2011).* Two series of simulations are run for both hillslopes, wherein two different solute exchange mechanisms between the surface and subsurface are considered. In the first series, that of no surface–subsurface mixing, solute exchange between the surface and subsurface can only occur via advection. In the second series, perfect surface–subsurface mixing*,* it is assumed that, at every time step, there is complete mixing between solute mass in the surface water and in the first computational layer of the subsurface, as described in *Gatel et al. (2020).* Theoretically, this corresponds to an "instantaneous" (i.e., occurring at a time scale on the order of the time step size) diffusive transport between the surface and subsurface.

5.4 Results

5.4.1 1D simulations

5.4.1.1 Advection-only

Figure 57 shows the analytical and model-simulated breakthrough curves for the three meshes, for the runs where Darcy's flux is equal to one and the dispersion module is not activated. Since no dispersion is introduced as a model input, any spreading out of the simulated breakthrough curves is entirely attributable to numerical dispersion, which, as expected, is larger for the coarse mesh (*mesh 2*) and decreases as the grid is refined. It can be noted as well that the finite volume advection solver does not cause numerical oscillations at the solution front.

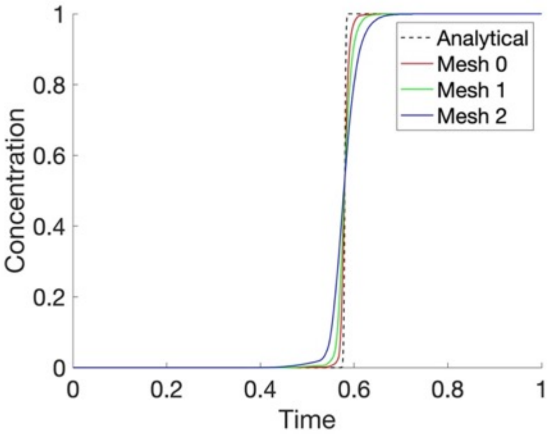

Figure 57: Comparison between analytical and numerical breakthrough curves in the 1D soil column test case with advection only and with Darcy's flux equal to one.

Figure 58 shows the apparent dispersion coefficients *D_L'* obtained through the best fit of equation (5) to the simulated data, as a function of the Darcy flux and the element surface area. The latter is a more suitable measure of grid size than a characteristic length, since for the advection solver implemented in CATHY the element faces are the fundamental support for the computation of fluxes (*Mazzia and Putti, 2005*). Numerical dispersion, in this case entirely captured by D_L', increases linearly with element size, and it also increases with flow rate. The corresponding "apparent dispersivities", computed as $\alpha_L' = D_L'/\bar{v}$ [L], i.e., the longitudinal dispersivities that would be required to obtain an equivalent physical dispersion, are always about two orders of magnitude smaller than the grid resolution, indicating that advection-only simulations in CATHY are affected by a very small numerical dispersion.

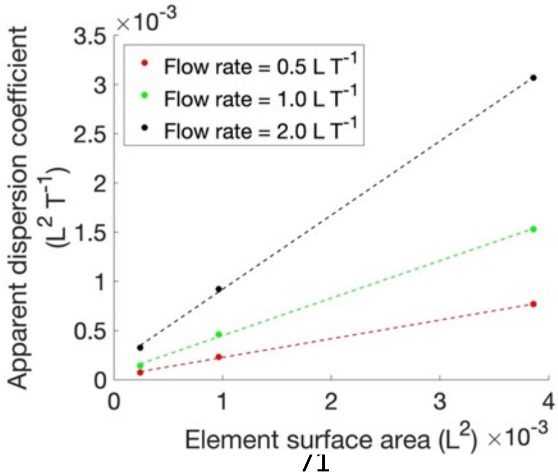

Figure 58: Correlation between apparent dispersion coefficients and the surface area of the single grid element for the three meshes and for three Darcy fluxes for the 1D soil column test case with advection only.

5.4.1.2 Advection and dispersion

The second series of 1D simulations involves activation of the subsurface transport dispersion module in CATHY. *Figure 59* shows the breakthrough curves simulated with the three meshes and four values of the physical dispersion coefficient, compared with the corresponding analytical solutions. Similar to the advection-only simulations, the finest grid exhibits the breakthrough curve that best matches the analytical solution, for all the dispersion coefficients. However, as the physical dispersion coefficient increases, the simulated curves tend to be closer to each other, indicating an increasingly marginal effect of numerical dispersion with respect to the physical dispersion introduced as model input. The best-fit coefficients of apparent dispersion, D_L'', are reported in *Table 17*, for comparison with the physical input values.

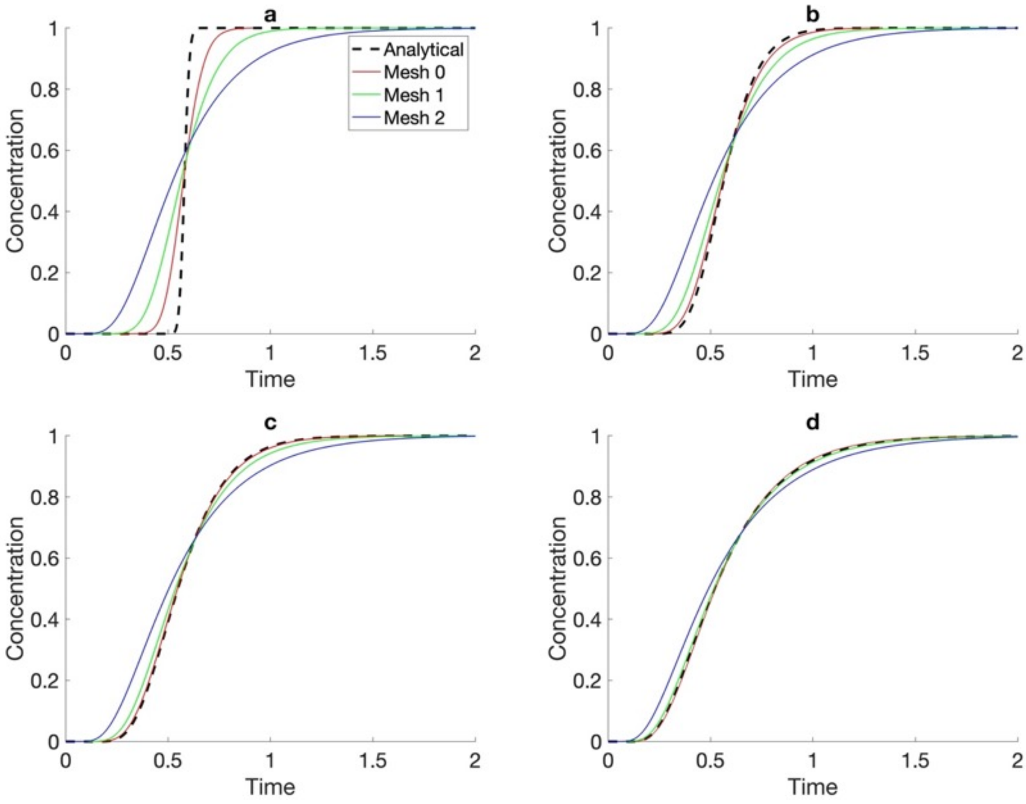

Figure 59: Comparison between analytical and numerical breakthrough curves for the three mesh discretizations, with input dispersion coefficients equal to a) 0.001, b) 0.05, c) 0.1, and d) 0.2 [L^2/T] and flow rate = 1[L/T], for the 1D soil column test case with advection and dispersion.

The decreasing impact of numerical dispersion with increasing values of the hydrodynamic dispersion coefficients is especially apparent for *mesh 1*, as shown by the analysis of the average absolute error (AAE) of the simulated concentrations with respect to the analytical solution (*Table 17)*. In particular, *mesh 1* gives an AAE that is more than three times larger than in *mesh 0* for $D_L = 0.05$ [L^2T^{-1}], but less than twice for $D_L = 0.2$ [L^2T^{-1}]. Analyzing how the errors change with the theoretical grid Péclet numbers, i.e., computed with the physical dispersion coefficient (D_L), associated to the three meshes in *Table 17*, it can be noted that the numerical dispersion in this case remains at an acceptable level (i.e., best-fit D_L' close to input D_L and low AAE values) for *Pe* values smaller than approximately 0.5.

Table 17: Theoretical grid Péclet number, best-fit apparent dispersion coefficient, and concentration average absolute error for the 1D soil column test case with advection and dispersion.

Input D_L [L^2T^{-1}]	***Mesh 0***			***Mesh 1***			***Mesh 2***		
	Pe	**D_L'**	**AAE**	***Pe***	**D_L'**	**AAE**	***Pe***	**D_L'**	**AAE**
0.001	17.24	0.02	0.016	34.48	0.05	0.033	68.97	0.22	0.065
0.05	0.34	0.06	0.007	0.69	0.10	0.022	1.38	0.23	0.039
0.1	0.17	0.11	0.003	0.34	0.14	0.014	0.69	0.26	0.029
0.2	0.09	0.19	0.003	0.17	0.22	0.005	0.34	0.33	0.017

5.4.2 3D simulations

5.4.2.1 Negligible physical dispersion

The 3D simulations with negligible input dispersion exhibit a significant spreading out of the solute plume, larger than we could expect with such a small dispersion coefficient, due to the time-splitting numerical scheme, which continuously transfers concentration information from elements to nodes and vice versa through a simple linear interpolation consistent with the finite element basis functions. A first analysis of the concentration profiles along the three Cartesian axes at the end of the simulation (0.025 [T]) reveals that they well approach a Gaussian function (*Figure 60*).

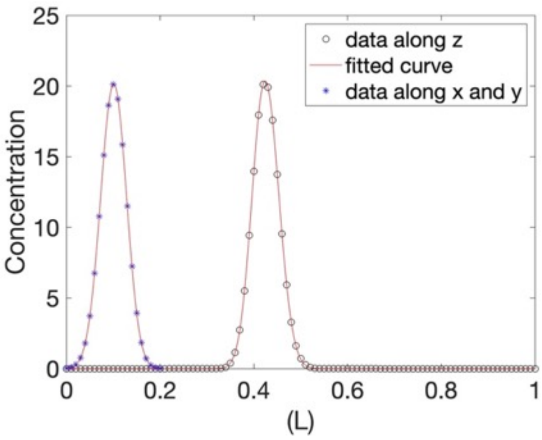

Figure 60: Example of concentration distributions along the Cartesian axes x, y, and z (mesh 0, final time of the simulation 0.025), fitted with Gaussian curves, for the 3D soil column test case with negligible physical dispersion.

The standard deviations of the fitted Gaussian functions provide the best estimate of the apparent dispersion coefficients, whose values (averaged over the three directions *x*, *y*, and *z*) are shown in *Figure 61*, as a function of the element size.

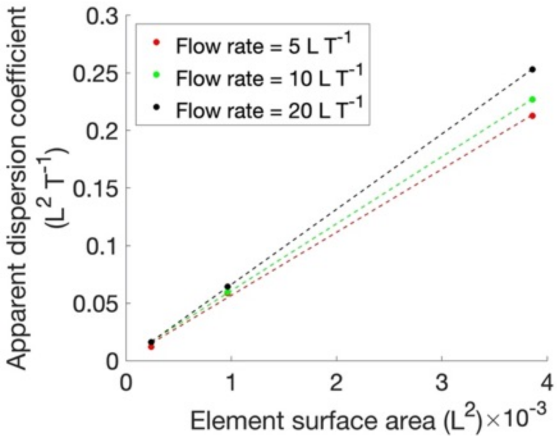

Figure 61: Apparent dispersion coefficient as a function of flow rate and element surface area for the 3D soil column test case with negligible physical dispersion.

As expected, the apparent dispersion coefficient is much lower in the finer mesh 0 and increases with element size. *Figure 61* also shows the impact of flow velocity on the numerical dispersion. As in the 1D simulations, the apparent dispersion coefficients increase with flux. The corresponding apparent dispersivities result in values that are approximately equal to 0.1, 0.2, and 0.3 times the grid resolution for mesh 0, mesh 1, and mesh 2, respectively, i.e., about one order of magnitude larger than in the 1D advection-only simulations, highlighting the stronger numerical dispersion resulting from the use of the node-based dispersion module in combination with the element-based advection solver.

5.4.2.2 Advection and dispersion

The second series of simulations for the 3D column test case is designed to assess at which point the numerical dispersion is no longer dominant compared to the physical dispersion. *Figure 62* shows the relation between the grid Péclet numbers evaluated using the theoretical dispersion coefficient and those computed with the apparent dispersion coefficient along the *z* direction using the simulated solute plume at time equal to 0.025 [T]. The 45-degree dashed line represents the ideal case in which theoretical and apparent dispersion coefficients coincide (i.e., zero numerical dispersion). The closer the dots are to this line, the more accurate the results of the simulations are. Examining the figure, we see that the simulation results remain accurate as long as $Pe_{Theoretical} < 1$. In particular, while model runs with *mesh 0* exhibit a slight deviation from the dashed line starting from about $Pe_{Theoretical} = 2$, both *mesh 1* and *mesh 2* show more significant deviations from the analytical solution, suggesting that numerical experiments should be designed to keep the grid Péclet number smaller than one, in order to keep numerical dispersion under control.

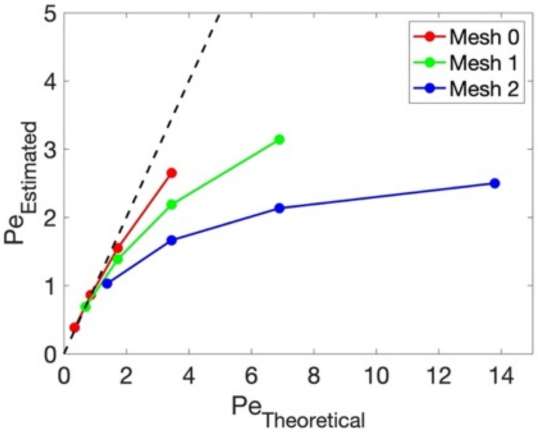

Figure 62: Péclet number evaluated using the theoretical values of dispersion coefficient vs Péclet number evaluated using the apparent values of dispersion coefficient, at time 0.025 [T] and along the z direction for the 3D soil column test case with advection and dispersion.

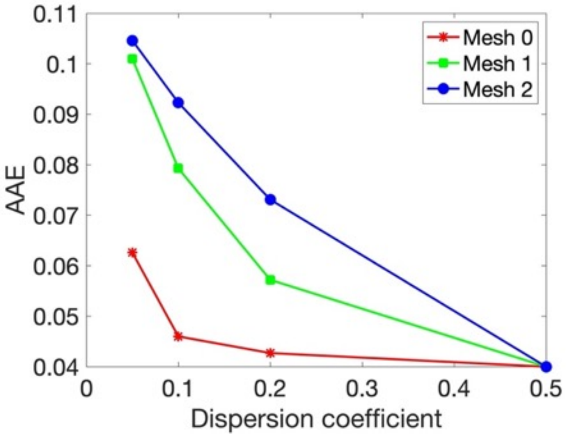

Figure 63: Average absolute error as a function of the input dispersion coefficient D_z and mesh resolution for the 3D soil column test case with advection and dispersion.

Similar to the 1D dispersion model runs, the 3D simulations show that the errors between the modeled concentrations and the analytical solution decrease as the input dispersion coefficient increases (*Figure 63*). Also in line with the 1D simulations, the error difference between the three meshes tends to decrease as the dispersion coefficient increases. With $D_z = 0.5$ [L^2T^{-1}], the three meshes converge to the same low value of concentration error.

To further assess the robustness of our analyses, we carried out a brief sensitivity analysis on the time step size, in order to verify whether the numerical dispersion arising from the transfer of concentration information between nodes and elements is affected by the number of times such transfer occurs. Taking as a reference the model run with *mesh 0* and $D_z = 0.05$ [L^2T^{-1}], we first decreased the dispersion solver time step to 0.0005 [T] (50% of the original time step), and then increased it to 0.005 [T] (five times the original time step). In the former case, the concentration AAE increases by 33% with respect to the reference run, while in the latter the AAE decreases by 10%. This would indeed suggest that the more times a transfer of information between nodes and elements occurs, the more numerical dispersion affects the results. However, the very same sensitivity analysis carried out with *mesh 0* and $D_z = 0.5$ [L^2T^{-1}], i.e., a run where the grid Péclet number is smaller than one, results in negligible error changes with respect to the reference run. This suggests that, if the grid Péclet number is small enough, not only can numerical dispersion caused by the time splitting technique be kept under control, but the simulation results are also robust with respect to the time stepping.

5.4.3 Hillslope simulations

Having determined a threshold on the grid Péclet number that ensures reasonably accurate results in the subsurface domain, we now analyze, in the third test case, how numerical dispersion affects coupled surface–subsurface solute transport processes. The simulations in the two hillslopes highlight how the contribution of pre-event water to the total streamflow hydrograph varies with the transport parameters.

Figure 64a) shows the total outflow and its pre-event water fractions in the cases where no surface–subsurface mixing is considered, i.e., solute mass can be exchanged between the surface and the subsurface via advective fluxes only. The black curve represents the total discharge, while the fraction of pre-event water is indicated by the colored lines. Unsurprisingly, given the short time scale of the event, when no-mixing is considered, the curves overlap each other, i.e., the fraction of pre-event water does not depend on the dispersion in the subsurface, but only on the way the surface is partitioned between saturated and unsaturated areas. Such partitioning is only controlled by the flow parameters.

Figure 64b) shows the results in the case of perfect solute mixing between the surface and subsurface. In this case, the mass discharge strongly depends on whether the subsurface hydrodynamic dispersion is activated or not. In the advection-only case (cyan curve), the dispersion module of CATHY is switched off, and the amount of pre-event water in the total discharge is higher than in the corresponding scenario without surface–subsurface mixing. When very low dispersion (see *Table 16*) is introduced, the dispersion module of CATHY is switched on and the modeled fraction of pre-event water jumps to very high levels. At that point, increasing the subsurface dispersion coefficient does not affect the solute mass discharge (magenta, green and yellow lines overlap each other), except for the high-dispersion run (red line), which exhibits a slightly higher pre-event water fraction.

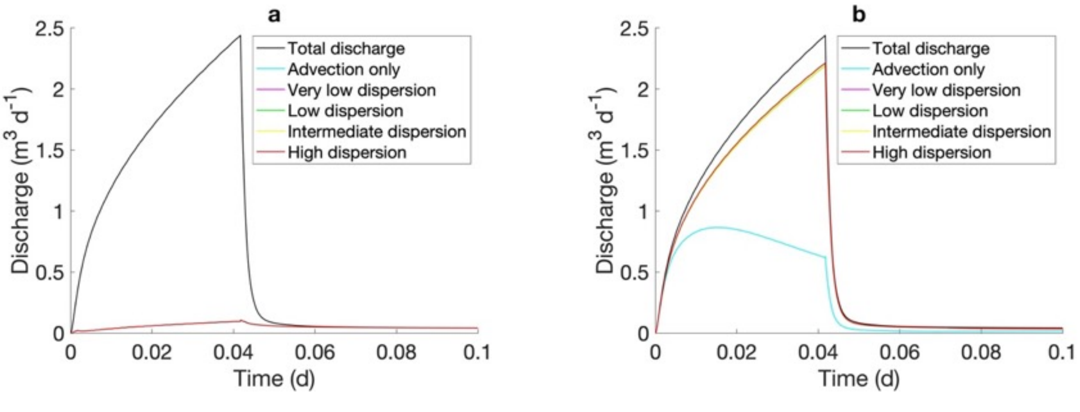

Figure 64: Total streamflow discharge (black line) and pre-event water discharge (colored lines) in the concave hillslope with a) no surface–subsurface mixing and b) perfect surface–subsurface mixing. In panel a) all the colored lines coincide with the red curve, while in panel b) the magenta and green curves coincide with the yellow curve which is visible just below the red curve.

The simulation results for the convex hillslope are reported in *Figure 65*. Compared with the concave hillslope, the main difference is that total discharge is smaller, due to the smaller fraction of surface saturated area. Similar to the concave hillslope, the pre-event water fraction is basically independent of the subsurface transport parameters in the case of no mixing, but strongly affected by the activation of the dispersion module in the case of perfect mixing.

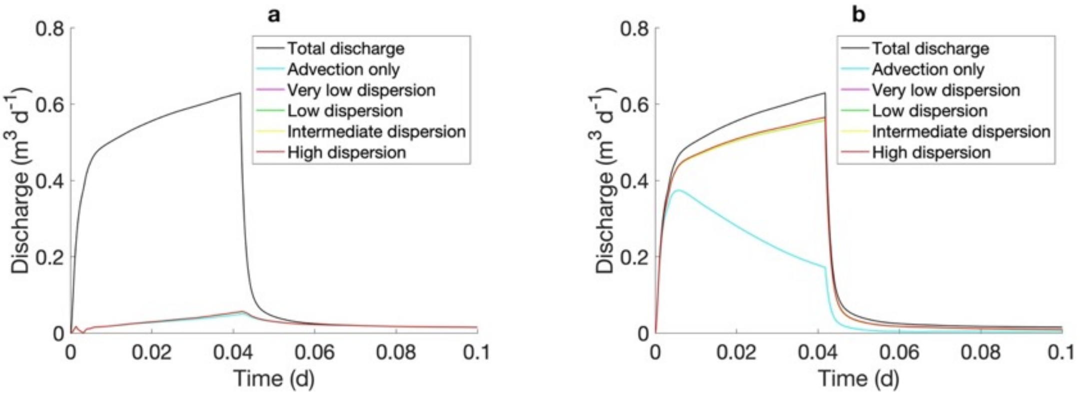

Figure 65: Total streamflow discharge (black line) and pre-event water discharge (colored lines) in the convex hillslope with a) no surface–subsurface mixing and b) perfect surface–subsurface mixing. In panel a) all the colored lines coincide with the red curve, while in panel b) the magenta and green curves coincide with the yellow curve which is visible just below the red curve.

The maximum grid Péclet numbers attained in both the concave and convex hillslopes, calculated from the input parameter values and the computed velocity field, are about 16, 16, 1.6, and 0. 16 for the very low, low, intermediate, and high dispersion runs, respectively. Comparing these *Pe* numbers with the graph of *Figure 62*, we note that the only simulations that are not expected to be dominated by numerical dispersion are those with intermediate and high dispersion, the latter being the most accurate.

Figure 66 shows the tracer concentration distributions at the end of the rainfall event in a portion of the hillslopes close to the outlet and for some selected scenarios. *Figures 66a)* and *b),* representing the scenarios with advection only and mixing, highlight how the solute remains confined within a shallow layer of soil, leading to the highest fraction of event water (i.e., smallest fraction of pre-event water) among all the mixing scenarios, consistent with the hydrographs in *Figures 64b)* and *65b).* The differences between the concave and convex hillslopes and mixing and no mixing scenarios are better appreciated when the dispersion module is switched on and a high input dispersion coefficient is used. *Figures 66c)* and *e),* representing the concave hillslope high dispersion with mixing and no mixing scenarios, respectively, highlight the enhanced capability of the tracer to transfer from the surface to the subsurface when mixing is activated. A similar effect, although less evident due to the geometry, can be seen for the convex hillslope in *Figures 66d)* and *f)*, whereby the tracer is able to penetrate underneath the “riverbed” only when mixing is activated. Note that the color scale for panels *a)* and *b)* is different from the one for panels *c), d), e)* and *f).*

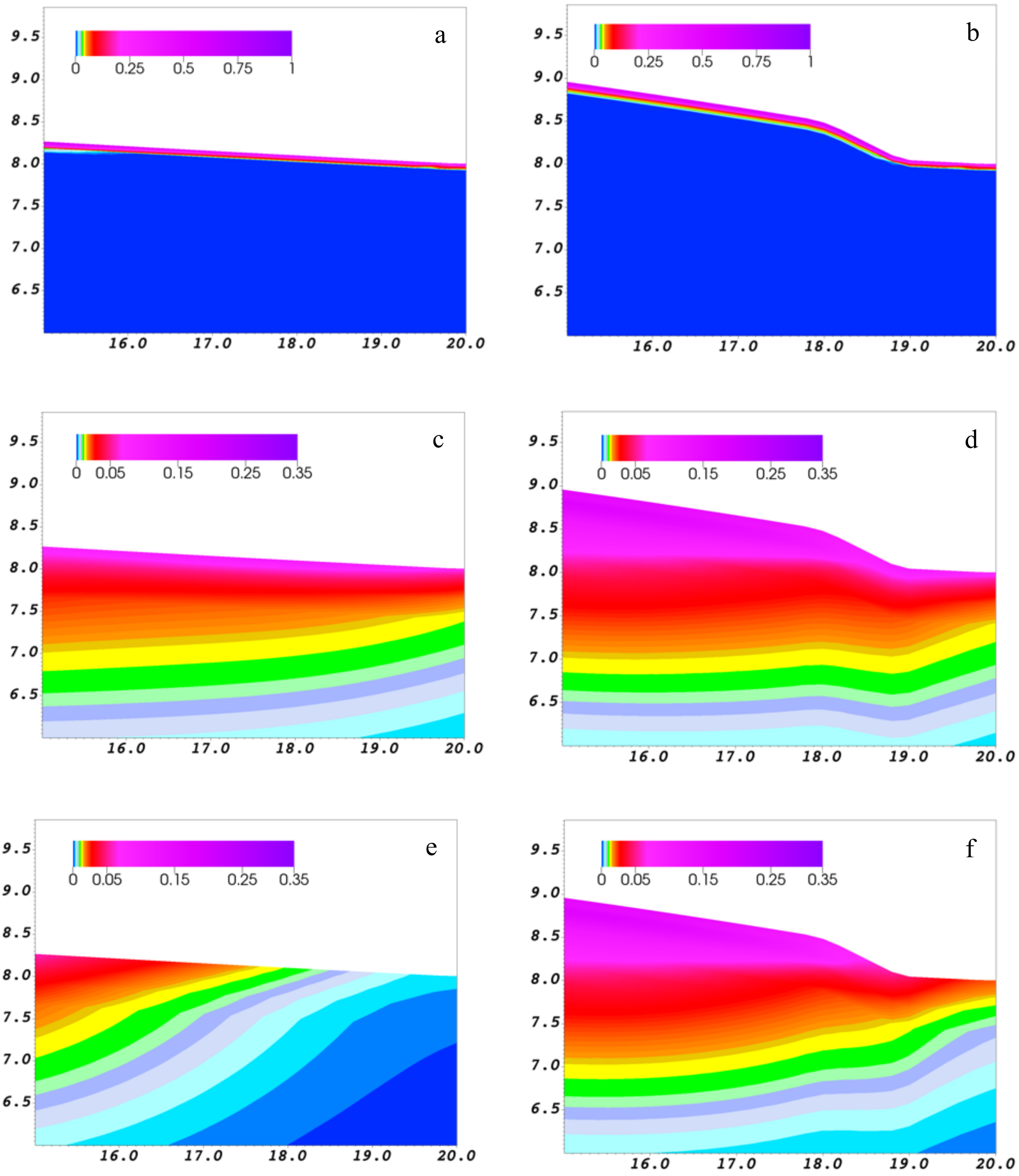

Figure 66: Concentration distribution at the downslope end (last 5 m) of the concave (graphs on the left) and convex (graphs on the right) hillslopes at simulation time 3460 s (just before the end of the 1-h rainfall event) for the cases of advection only with mixing (a and b), high dispersion with mixing (c and d), and high dispersion with no mixing (e and f). Note the two different color scales, for panels a and b and for panels c, d, e, and f.

In *Figure 67* we show the time series of solute mass balance terms for the same scenarios as *Figure 66*. The cumulative total mass ("tot. in") introduced into the system, 0.416 kg, corresponds to the input concentration (1 kg m^{-3}) applied via rainfall (0.0208 m h^{-1}) for a duration of 1 h over a domain of surface area 20 m^2. Note that this is the mass into the whole system (surface plus subsurface domains), while the mass exiting the system ("tot. out") in these runs occurs only via the designated surface outlet cell. *Figure 67* shows an excellent mass balance for all the scenarios. Indeed, the solute mass balance error over the whole surface-subsurface domain remains smaller than 0.5%. From a process point of view, panels *c)* and *d)* compared with panels *a)* and *b)* highlight how activation of dispersion (with mixing) increases the solute stored in the system, thereby decreasing the amount of tracer that reaches the outlet. Whereas the deactivation of mixing, as seen by comparing panels *e)* and *f)* with panels *c)* and *d)*, results in a dramatic decrease in surface storage, which translates to a corresponding increase of the solute tracer mass in the outflow.

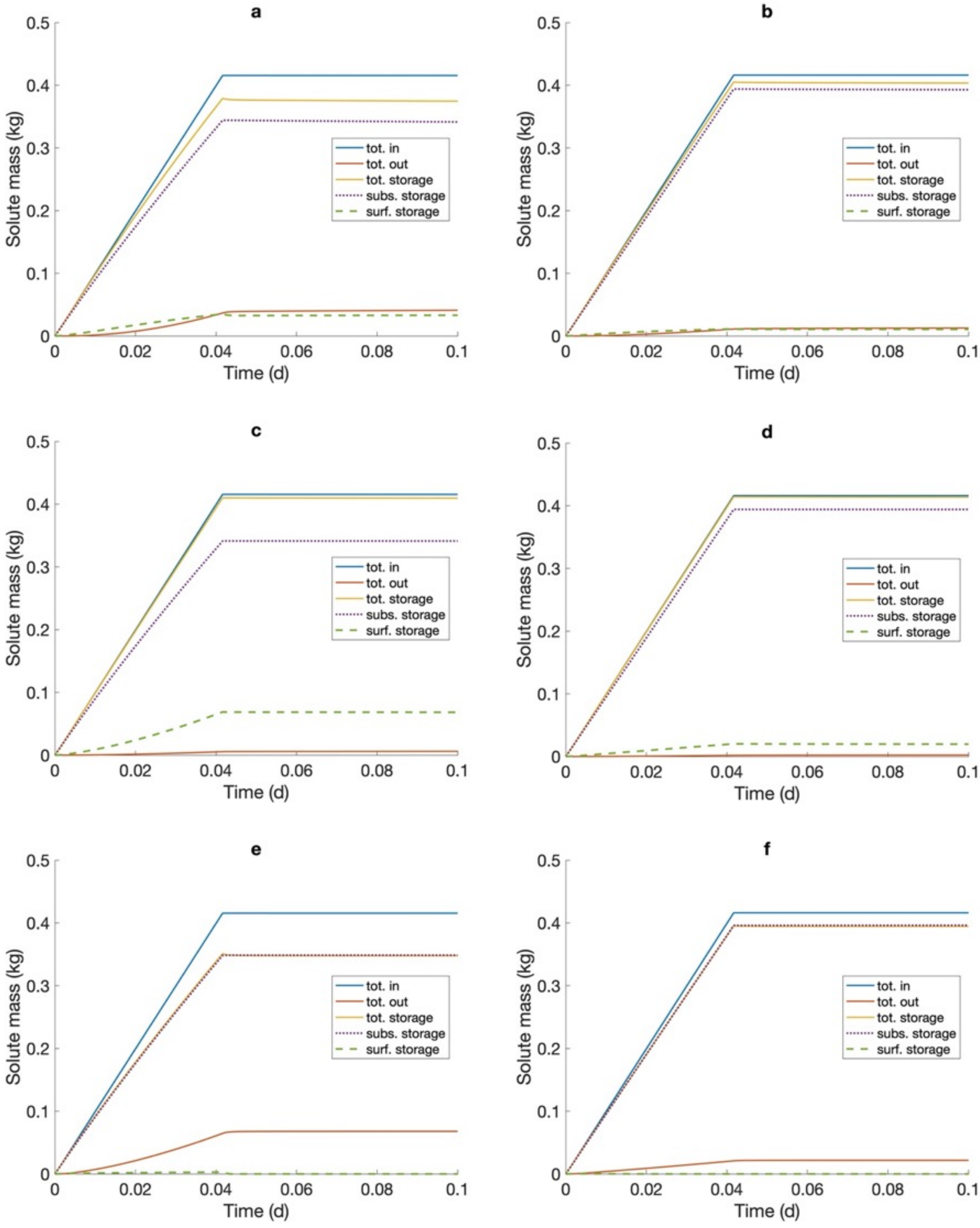

Figure 67: Time series of solute mass balance terms for the concave (graphs on the left) and convex (graphs on the right) hillslope simulations for the cases of advection only with mixing (a and b), high dispersion with mixing (c and d), and high dispersion with no mixing (e and f).

5.5 Discussion

Integrated surface–subsurface hydrological models (*Paniconi and Putti, 2015; Fatichi et al., 2016*), including CATHY (*Camporese et al., 2010*), are physics-based numerical models increasingly used not only for water flow simulations in hillslopes and catchments, but also for contaminant transport (e.g., *Weill et al., 2011*; *Ligget et al., 2015*; *Scudeler et al., 2016b*; *Daneshmand et al., 2019*; *Gatel et al., 2019*). For this reason, it is important to understand and quantify how the numerical dispersion of solute transport in the subsurface modules of ISSHMs can affect simulation results.

Numerical dispersion depends mainly on the scheme used to solve the advection–dispersion equation. In the case of CATHY, a time-splitting algorithm solves advection on elements by an explicit numerical scheme and dispersion on nodes with an implicit scheme. This makes the solver numerically robust and computationally efficient, but the continuous transfer of concentration information from nodes to elements (and vice versa) is known to lead to enhanced mass spreading (*Weill et al., 2011; Gatel et al., 2019*). However, this has never been quantified so far.

The first part of this study provides a useful quantification of the numerical dispersion in CATHY by comparing well-known analytical solutions with results from two soil column test cases (1D and 3D) in a number of scenarios, first with advection only (or negligible physical dispersion) and then including advection and dispersion. The 1D simulations with advection only show the robustness of the advection numerical scheme implemented in CATHY, an explicit finite volume solver with numerical stability ensured by enforcing the Courant–Friedrichs–Lewy condition (*Mazzia et al., 2000*). The numerical dispersion in the 1D simulations remains very small for a range of grid resolutions and flow velocities, with apparent dispersivity values that are at least two orders of magnitude smaller than the element size. It should be noted that these advection-only scenarios are useful in the analyses performed but are not intended as realistic test cases. The 1D simulations with longitudinal dispersion show that activating the dispersion module potentially leads to significant numerical dispersion. However, this can be controlled by adjusting the mesh resolution to the input value of the longitudinal dispersion coefficient in order to maintain a grid Péclet number smaller than 1.0 (ideally, 0.5 or less). This condition on *Pe* is a new criterion based on an experimental analysis of the time-splitting solver in CATHY, which is more restrictive than the common limit of 2.0 (e.g., *Diersch, 2014*) derived from the theoretical analysis of linear convective-diffusive problems solved by standard FD or FEM schemes.

The 3D simulations with the dispersion module activated, but with negligible values of the dispersion coefficients, reveal the strong numerical dispersion related to the transfer of concentration information from elements to nodes and vice versa. In this case, the numerical dispersion is characterized by apparent dispersivities of almost the same order of magnitude as the element size. Additional 3D simulations with longitudinal coefficients of dispersion as in the 1D case highlight that also in this case it is necessary to maintain the grid Péclet number smaller than 1.0 in order to prevent the numerical dispersion from becoming dominant.

As a final remark on the soil column test cases, we note that the solute mass balance error remains lower than 0.3% in all the model runs. Furthermore, the concentration errors related to the dispersion module alone, calculated in a number of simulations with flow equal to zero (not shown here), are three to five orders of magnitudes smaller than the corresponding simulations with advection and dispersion. This, combined with the fact that the numerical dispersion affecting the advection solver is also very small, confirms that the main source of numerical dispersion in CATHY is a particular numerical artifact arising from the time-splitting scheme and its related exchange of information between nodes and elements.

In the third test case of this study, the CATHY model is applied to simulate the contribution of pre-event water to the total streamflow hydrograph of two synthetic hillslopes in response to a rainfall event. Interesting insights can be gained by comparing our results with those reported by *Liggett et al. (2014)*, who applied the HGS model to the same synthetic hillslopes. For solute exchange between the surface and the subsurface, HGS relies on a dual-node approach, whereby the mass flux is computed as the sum of advective and dispersive components. *Liggett et al. (2014)* studied three different conditions: (i) advection-only, in which the solute exchange across the surface–subsurface interface occurs solely via advection, (ii) advection–diffusion, in which molecular diffusion is also introduced, and (iii) advection–dispersion, where mechanical dispersion is considered as well. For each of these three conditions across the surface–subsurface interface, *Liggett et al. (2014)* simulated the different subsurface dispersion scenarios reported in *Table 3*. Our CATHY simulations with no surface–subsurface mixing broadly correspond to the advection-only scenarios with HGS, which in this case also shows that the pre-event water contribution to the hydrograph does not depend on the subsurface dispersion parameters, over the course of a single rainfall event. The pre-event water fractions simulated by CATHY in the case of perfect surface–subsurface mixing fall within the range spanned by the HGS simulations with advection–dispersion. In particular, the subsurface advection-only scenarios simulated by CATHY closely mimic the results of HGS with very low or low dispersion, while the numerical dispersion arising from the CATHY time-splitting technique makes the very low and low-dispersions scenarios collapse onto the intermediate-dispersion scenario. This occurs because the order of magnitude of the numerical dispersion, introduced when switching on the dispersion module, is higher than the one related to the physical dispersion coefficient, to the point that any modification of this coefficient does not influence the solute concentration until a threshold on the Péclet number is reached. This threshold here corresponds to a *Pe* equal to 1 or less, consistent with the criterion developed in the soil column runs.

This issue does not seem to affect the HGS model. However, the mesh resolution used here (0.20 m horizontally with 40 vertical layers) is much coarser than the one used by *Liggett et al. (2014)* (0.04 m horizontally with 400 vertical layers). Despite the much smaller number of computational nodes, our simulations give similar results, when numerical dispersion is not dominating, thanks to the high CPU efficiency of the time-splitting technique. In summary, this series of hillslope simulations shows that, if the numerical dispersion related to time-splitting is kept under control using the grid Péclet number criterion discussed above, the CATHY model can provide robust solute transport predictions without the need for additional parameters, such as a longitudinal dispersivity across the surface–subsurface interface, and with a relatively parsimonious grid discretization.

5.6 Conclusions

We applied the CATHY model to examine the main sources of numerical dispersion in the simulation of subsurface solute transport and how such dispersion might affect solute transport predictions in integrated surface–subsurface hydrological models. To this aim, we first carried out a series of subsurface-only simulations in two soil column test cases, using known analytical solutions to accurately quantify the numerical dispersion affecting the model. These simulations allowed us to define a more restrictive threshold value for the grid Péclet number compared to typical values in standard FEM codes. To ensure a satisfactory solution accuracy, *Pe* should not exceed 1 or, even better, 0.5. Then, CATHY was applied to two synthetic hillslopes in a series of fully coupled surface–subsurface simulations to show the possible impacts of subsurface numerical dispersion on the prediction of the pre-event water contribution to the total streamflow hydrograph. Overall, this study provides quantitative recommendations for setting up integrated surface–subsurface hydrological models that can control the effects of numerical dispersion on coupled solute transport simulations. Indeed, based on the grid Péclet number threshold and the expected range of dispersion coefficient, the model user can define a proper grid size that will meet the criterion of Pe smaller than 0.5-1.0. Although the results presented here are strictly valid for the CATHY model only, the methodology proposed for the evaluation of numerical dispersion is general and therefore may be used in assessing any other ISSHM. Moreover, the column test cases with 1D and 3D analytical solutions and the hillslope test case that has now been used in assessing two widely used ISSHMs may have appeal as new benchmark problems for integrated surface-subsurface hydrological models, extending to solute transport the flow-only suite of benchmarks reported in model intercomparison studies *(e.g., Maxwell et al., 2014; Kollet et al., 2016)*.

6. General conclusions

The present study investigated the scientific issues that a water utility company is expected to face in the elaboration of the Water Safety Plans. The WSP constitutes the most effective tool to guarantee good water quality and consumers health protection. The study begun with the implementation in CATHY of a previous model originally built in FeFlow. This decision was taken because CATHY model has some characteristics that are not present in the other code, i.e., partitioning of rainfall into infiltration and runoff, direct computation of recharge, more flexibility in the implementation of new calibration algorithms, and being an open-source code. The initial mesh, representing a multilayer system of an unconfined aquifer followed by eight confined aquifers, after having been modified several times and used for sensitivity analysis, was at the end abandoned. It was cut, maintaining only the portion of the domain of the first unconfined aquifer. This allowed, among other things, for the reduction of computational time for calibration. To improve this step, FeFlow was involved again. Once calibrated and validated, the model was run to simulate an irrigation variation scenario following the European directive requirements with the aim of reducing the consumption of the water resource, in this case derived from the Piave River, where the ecological flow must be maintained. The impact of the transition from flood irrigation to sprinkler irrigation on the aquifer recharge seems less considerably than expected, with an estimated decrease of about 10% against a reduction of water withdrawn from the Piave river equal to 50%. This relatively limited impact, at least in the short term, can be explained by two main factors. First, the spatial map of the mean recharge over the irrigation season shows that overall recharge seems to be more controlled by the hydraulic conductivity distribution than by the irrigation method. Second, the area affected by the change in irrigation techniques is less than 30% of the computational domain; therefore, a more localized study focused entirely on this area would likely result in a more significant impact.

Due to lack of time, it was not possible to perform an additional step of the study, which would have been the analysis on the contamination. However, the numerical dispersion affecting CATHY together with calibrated and validated model, can be considered and interesting starting point for the study of the vulnerability to the contamination. The definition of the wells head protection and the risk assessment are two important points of the WSPs elaboration, this analysis would complete the realization of a preliminary decision support tool for the water utility companies. This could also be complemented by additional information on the structure of the subsurface in the area of interest, which should be available in the near future (e.g., through a large scale airborne electromagnetic survey currently being planned).

7. Acknowledgements

B. G. acknowledges the support of her PhD scholarship by UniSMART – Fondazione Università degli Studi di Padova and Alto Trevigiano Servizi S.r.l..

8. Appendix

CATHY - CATchment HYdrologic model

- User Guide –

Some pages of the thesis are dedicated to the description of CATHY model, in order the have a sort of guide for future users. Besides a general description of its source, input and output files, a focus will be made on the ones which setup was fundamental for this project work.

8.1 Files organization

CATHY files, when downloaded by the online page https://bitbucket.org/cathy1_0/cathy/src/master/ are grouped in 4 main folders:

- *src* containing the source files of the code
- *prepro* containing the file for the data pre-processing, useful for the mesh building
- *input* containing the input files
- *output* containing the output files

8.2 How the model works

Three phases are required to implement a working CATHY model of a specific case study, namely pre-processing, processing, and post-processing, and the following steps are necessary to create the flow model:

1) Create the input files for the pre-processor **hap**
2) Run the pre-processor **hap**
3) Create the input files for the processor **CATHY**
4) Perform the simulation by running the processor **CATHY**
5) Run the post-processing subroutines (written in **Matlab**) to extract and view results

8.3 Pre-processing

8.3.1 Modules/subroutines for the pre-processing and first mesh setup method

The CATHY pre-processing requires the main program *cppp.f90* and all the subprograms (modules and subroutines) listed in *Table 4.* During the pre-processing, the main program and all involved modules and subroutines must be compiled in a specific order (as in the *Table 4*), as recalled in the main program *cppp*. For example the *mpar* and *mbbio*, being modules the first statements, must be compiled first.

Starting from DEM data (*dtm_13.val*) and parameters file (*hap.in*), the main program *cppp.f90* and the related modules and subroutines produce a complete set of files describing physiographic features of a drainage system. Such files represent the input files for CATHY simulations and GIS visualization.

Table 4. Pre-processing modules and subroutines

Name	Type	Description

mpar	.f90	module	Module containing definitions of parameters assigned in the parameter file <parfile>.
mbbio	.f90	module	The module manages the I/O between programs and binary files basin_b/basin_i.
wbb_sr	.f90	subroutine	This program defines the structure of the binary files basin_b/basin_i using the ascii DEM file <demfile>, which contains the catchment cell elevations.
streamer	.f90	module	Module AB_Normal called by dbase.f90 and shape.f90
shape	.f90	module	Module Shapefile
qsort	.f90	subroutine	Quicksort. This subroutine is called by the subroutine csort.
csort	.f90	subroutine	The subroutine CSORT (Cells Sort) sorts the cells of a catchment in the order of descending elevations. The binary file qoi contains the number of processed cells in the first record and the pointers i_basin_qo corresponding to the sorted cell elevations qo in the subsequent records.
depit	.f90	subroutine	The subroutine DEPIT checks that each catchment cell has a lower cell among the neighbouring cells. When this is not verified the processed cell is raised of the quantity eps above le lowest neighbouring cells. The procedure is iterated until all the pits are removed. The number of modifications is recorded in the variable n_modifiche.
cca	.f90	subroutine	Contour Curvature Analysis (cca) evaluates the curvature of each cell and assigns the dmID.
smean	.f90	subroutine	The subroutine SMEAN calculates the mean catchment slope based on maximum (theoretical) values obtained from facet analysis
facet	.f90	subroutine	The subroutine FACET is called by dsf.f90. It calculates the aspect and the slope (positive downward) of the steepest direction within a given triangle (facet).
dsf	.f90	subroutine	The subroutine DSF (Drainage System Features) determines two drainage directions for each DEM cell. Depending on parameter dmID, one or two drainage directions are actually employed. For each DEM cell, the following physiographic features are assigned: (1) weights associated to drainage directions: w_1 and w_2; (2) flows directions: p_outflow_1 and p_outflow_2; (3) elemental lengths of channels: epl_1 and epl_2 (it is assumed here that delta_x=delta_y); (4) local slopes (positive downward) of channel elements: local_slope_1 and local_slope_2; (5) the funcion ASk=AS**k. For at most the two neighbours spilling cells are also updated: (1) the upstream catchment area A_inflow and (2) the upstream error made between selected and theoretical drainage directions sumdev_num. It refers to facet.f90.
hg	.f90	subroutine	The subroutine HG (Hydraulic Geometry) determines the hillslope and channel cells within the catchment and assign the hydraulic geometry parameters.
mrbb_sr	.f90	subroutine	The program MRBB (Multiple RBB) reads the parameters contained in the binary files basin_b/basin_i and writes many DTM ascii files as output.
dbase	.f90	module	Managing DBF files for both reading and writing.
bb2shp_sr	.f90	subroutine	The program reads the parameters contained in the binary files basin_b/basin_i and write a *.SHP ArcGIS file. It refers to DBF (dbase) and Shapefile (shape).
cppp	.f90	main program	Main program for the pre-processing.

CATHY pre-processing requires two input files in ASCII format (editable with a text editor):

- *dtm_13.val*
- *hap.in*

File *dtm_13.val* is a raster file containing the Digital Elevation Model (DEM) of the area of intertest. This is a matrix of elevation without the header: the number values in rows and columns individuates the mesh nodes, and they represent the elevation of the points, expressed in meters.

```
3.5    3.5    3.5    3.5    3.5    3.5    3.5    3.5
3.5    3.5    3.5    3.5    3.5    3.5    3.5    3.5
3.4375 3.4375 3.4375 3.4375 3.4375 3.4375 3.4375 3.4375
3.4375 3.4375 3.4375 3.4375 3.4375 3.4375 3.4375 3.4375
3.375  3.375  3.375  3.375  3.375  3.375  3.375  3.375
3.375  3.375  3.375  3.375  3.375  3.375  3.375  3.375
3.3125 3.3125 3.3125 3.3125 3.3125 3.3125 3.3125 3.3125
3.3125 3.3125 3.3125 3.3125 3.3125 3.3125 3.3125 3.3125
3.25   3.25   3.25   3.25   3.25   3.25   3.25   3.25
3.25   3.25   3.25   3.25   3.25   3.25   3.25   3.25
3.1875 3.1875 3.1875 3.1875 3.1875 3.1875 3.1875 3.1875
3.1875 3.1875 3.1875 3.1875 3.1875 3.1875 3.1875 3.00*
```

* Is important to set a point of the DEM that is lower to all the others.

The *hap.in* is a parameter file containing all the structural and terrain analysis parameters to perform the terrain analysis. The section "*structural parameters*" contains information on the discretization of the catchment surface.

```
--------------------------------------------------------------------------------
STRUCTURAL PARAMETERS
--------------------------------------------------------------------------------
Grid spacing along the x-direction =                     20.00            (1)
Grid spacing along the y-direction =                     20.00            (2)
DEM rectangle size along the x-direction =               45               (3)
DEM rectangle size along the y-direction =               43               (4)
Number of cells within the catchment =                 1210               (5)
X low left corner coordinate =                      2268651.15126480      (6)
Y low left corner coordinate =                      2452773.22533040      (7)
--------------------------------------------------------------------------------
```

(1), (2) Distance between each center cell in x and y directions

(3), (4) Number of square cells in x direction (number of matrix columns) and in y direction (number of matrix rows)

(5) Number of cells that make up the grid of square cells (number of elements of the matrix)

(6), (7) Information related to the x and y low left coordinates are obtained from the ASCII files exported from ArcGIS or GRASS.

The section "*terrain analysis parameters*" provides information useful for extracting a conceptual drainage network from the grid-based DEM. Much of the following descriptions are mainly extrapolated from:

- Orlandini *et al. (2003) "Path-based methods for the determination of nondispersive drainage directions in grid-based digital elevation models"*
- Orlandini and Moretti (2009) *"Determination of surface flow paths from gridded elevation data"*
- Camporese *et al.* (2010) *"Surface-subsurface flow modeling with path-based runoff routing, boundary condition-based coupling, and assimilation of multisource observation data"*

```
------------------------------------------------------------------------------------
TERRAIN ANALYSIS PARAMETERS
------------------------------------------------------------------------------------
Depit threshold slope =                                        0.100E-03         (8)
Drainage directions method (LAD:1,LTD:2) =                     2                 (9)
Upstream deviation memory factor (CBM:0,PBM:1) =               0.100E+01         (10)
Threshold on the contour curvature (NDM:-1E10;DM:+1E10) =     -0.100E+11         (11)
Nondispersive channel flow (0:not-required;1:required) =       1                 (12)
Channel initiation method (A:1,AS**k:2,ND:3) =                 1                 (13)
Threshold on the support area (A) =                            0.400000000E+06 (14)
Threshold on the AS**k function =                          16000.00              (15)
Exponent k of the AS**k function =                             2.00              (16)
Threshold on the normalized divergence (ND) =                 -0.100E-01         (17)
Path threshold slope =                                         0.100E-03         (18)
Drainage direction of the outlet cell (if necessary...)  =     8                 (19)
Boundary channel construction (No:0,Yes:1) =                   0                 (20)
Coefficient for boundary channel elevation definition =        0.50              (21)
Coefficient for outlet cell elevation definition =             0.50              (22)
------------------------------------------------------------------------------------
```

(8) The quantity used by the subroutine depit to raise depressed cell is equal to the depit threshold slope times the grid cell size. The value of the **depit threshold slope** (i.e. the ratio between that quantity used to raise depressed cells and the grid size) is often set equal to 10^{-4}. The D8-LAD or the D8-LTD method is then applied to form the drainage network and to calculate the drainage areas (through the subroutine dsf.f90). DEM cells are processed in the order of descending elevation. Upstream drainage areas are summed up over all the drained cells.

(9) The definition of the **drainage directions** is done through either the D8-LAD (eight drainage directions, least angular deviation) scheme or the D8-LTD (eight drainage directions, least transverse deviation) scheme. The classical D8 (eight drainage directions) scheme (O'Callaghan and Mark, 1984; Marks et al., 1984), the earliest and simplest method for specifying flow direction, assigns flow from each pixel to one of its eight neighbors, either adjacent or diagonal, in the direction with steepest downward slope. The algorithm that incorporates the D8-LAD and D8-LTD methods for identifying the drainage network and calculating the drainage areas within a catchment requires three preliminary operations, in which (1) DEM cells of the catchment are sorted into descending elevation order (through the subroutine *csort.f90*), (2) a

recursive procedure is used to raise (by filling them) the elevations of the cells located in flat or depressed areas (i.e. pits) so as to ensure a drainage direction with a small positive slope (downward) for all the cells of the catchment (through the subroutine *depit.f90*), and (3) DEM cells are sorted again into descending elevation order (through the subroutine *csort.f90* again).

(10) In both methods a dampening factor (λ) (i.e. **deviation memory factor**) must be considered. For λ=0 the selection of the drainage directions is based only on the local angular/transversal direction (i.e. cell based method, CBM); for λ=1, full memory of the upstream angular/transversal deviations is retained (i.e. path based method, PBM). The D8-LAD method with λ=0 reproduces the classical D8 method. As shown in Orlandini et al., 2003 along the valleys, the D8-LTD method with λ=1 appears to provide significantly better results than the D8-LAD method with λ=0.

(11) The surface flow paths can be described by using single flow directions (convergent terrains) and multiple flow directions (divergent terrains). The contour curvature, defined as the curvature of contour lines, provides a measure of the morphological convergence of the terrain, and can therefore be applied to determine whether to use single or multiple flow directions for each grid cell. The selection of the **plan curvature threshold** allows for a morphologically meaningful use of single (nondispersive, NDM:-1E10) and multiple (dispersive, DM:+1E10) flow directions across a terrain. Combining this information with the method for the definition of the drainage directions and the dampening factor (λ), the following relevant cases can be highlighted:

- *D8-LAD with λ=0 and NDM: D8 classical method proposed by O'Callaghan and Mark (1984) and Marks et al. (1984);*
- *D8-LAD with λ=0 and DM: D∞ method proposed by Tarboton (1997);*
- *D8-LTD with λ=1 and NDM: D8-LTD proposed by Orlandini et al. (2003);*
- *D8-LTD with λ=1 and DM: a variant of D8-∞ (D∞-LTD).*

(12) A further specification must be done in the section "**Nondispersive channel flow**": if equal to 0, channel cells where flow will potentially be dispersive are considered actually dispersive; if equal to 1, channel cells where flow will potentially be dispersive are forced to be nondispersive.

(13) The distinction between hillslope and channel flow can be based on three criteria (channel initiation method) (13) by posing a threshold condition on:

- the upstream drainage area A (14) (e.g., Montgomery and Foufoula-Georgiou, 1993)
- the function AS^k (15,16), being S the local terrain slope and k an exponent (Montgomery and Dietrich,1988, 1989)
- the gradient divergence normalized by mean gradient (17) (land surface curvature divided by the mean terrain slope) (Howard, 1994).

Using for instance the first criterion, rill flow is assumed to occur for all those cells for which the upstream drainage area A $[L^2]$ does not exceed the threshold value A_t $[L^2]$, while channel flow is assumed to occur for all those cells for which A equals or exceeds A_t. The option to explicitly define channel head locations is also included in the model.

(18) **Path threshold slope** is not important for the extraction of the river network. (It is used only in the tool program odx.f90 that calculates the optimal DELTA_X for the simulation according to the physiographic characteristics obtained from the application of the hydraulic geometry theory).

(19) If necessary, the **drainage direction of the outlet cell** must be specified. If this parameter is set equal to 0, the drainage direction of the outlet cell is defined automatically and set equal to the drainage direction of the upslope cell with the biggest upslope area. Drainage directions can be identified by pointers to the downslope cells. The rule employed in this set of programs is shown in the following sketch:

3	6	9
2		8
1	4	7

The other possible values of this parameter are those reported in the sketch, where the center cell is the current cell.

(20) The option "**Boundary channel construction (No:0, Yes:1)**" is useful to exceed the limitation of the program that correctly perform basins with only a single outlet cell. If, known the outlet cell, is necessary to automatically define the boundary of an unknown catchment, set this option equal to one maybe helpful. With this parameter equal to one, independently of the shape of the DEM, that obviously must exceed the extension the study basin, the elevation of the cells belonging to the boundary is pulled down and an outlet cell is defined. Is underlined here that the shape of the DEM is free but a sufficiently regular shape is suggested. Exceptional parameter value:

- Boundary channel construction = 10; the boundary channel construction is performed but the default procedure for depicting the boundary channel constructed described below is skipped.

- Boundary channel construction >10; the boundary channel construction and the other standard procedure are performed but all the DEM is shifted upward by the value of the boundary channel construction parameter.

(21) If the "Boundary channel construction" parameter is set equal to 1, the "**Coefficient for boundary channel elevation definition**" is the value of the coefficient that, multiplied for the elevation of the lowest cell of the basin, allows to define the elevation of the boundary channel cells. Value between 0.05 and 0.95 are suggested.

(22) If the "Boundary channel construction" parameter is set equal to 1, the "**Coefficient for outlet cell elevation definition**" is the value of the coefficient that, multiplied for the elevation of the boundary channel cells, allows to define the elevation of the outlet cell. To be sure that the outlet cell is lower than all boundary channel cells value between 0.05 and 0.95 are suggested.

The Boundary channel construction is performed in *wbb_sr* subroutine. After the definition of the boundary channel and the outlet cell another operation is performed: all cells of the boundary channel starting from a cell near the outlet cell are depitted with the slope defined at the parameter “Depit threshold slope”. As reported in the description of the Boundary channel construction parameter, this operation can be skipped if the Boundary channel construction parameter is set equal to 10.

```
------------------------------------------------------------------------------------
RIVULET NETWORK PARAMETERS (HYDRAULIC GEOMETRY OF THE SINGLE RIVULET)
------------------------------------------------------------------------------------
Rivulet spacing =                                   20.000                      (23)
Reference drainage area (As_rf) =                    0.484000000000E+06         (24)
Flow discharge (Qsf_rf,w_rf) =                       0.010               1.000  (25)
Water-surface width (Wsf_rf,b1_rf,b2_rf) =          13.761     0.260     0.500  (26)
Resistance coefficient (kSsf_rf,y1_rf,y2_rf) =       2.989     0.200     0.300  (27)
Initial flow discharge (Qsi_rf) =                    0.000
------------------------------------------------------------------------------------
CHANNEL NETWORK PARAMETERS
------------------------------------------------------------------------------------
Reference drainage area (As_cf) =                    0.484000000000E+06         (28)
Flow discharge (Qsf_cf,w_cf) =                       0.010               1.000  (29)
Water-surface width (Wsf_cf,b1_cf,b2_cf) =           2.752     0.260     0.500  (30)
Resistance coefficient (kSsf_cf,y1_cf,y2_cf) =      29.891     0.200     0.300  (31)
Initial flow discharge (Qsi_cf) =                    0.000                      (32)
------------------------------------------------------------------------------------
```

(23) Rivulet spacing

(24) Reference drainage area

(25) Flow discharge

(26) Water-surface width

(27) Resistance coefficient

(28) Reference drainage area

(29) Flow discharge

(30) Water-surface width

(31) Resistance coefficient

(32) Initial flow discharge

Running the pre-processor for a given case study (i.e. specific DEM and input parameters) requires the creation of an executable file. This file is generated through the compilation of the main program cppp.f90 and all the subprograms (in Teminal or Command Prompt, being in the *prepro* folder) as follows:

```
./cppp
```

Three questions appear, and the answers to be given are the following:

```
Select the header type:
 0) None
 1) ESRI ascii file
 2) GRASS ascii file
 (Ctrl C to exit)

 -> 2

 Select the nodata value:
 (Ctrl C to exit)

 -> 0

 Select the pointer system:
 1) HAP system
 2) Arc/Gis system
 (Ctrl C to exit)

 -> 1
```

Running the executable file has allowed to generate a complete set of files describing physiographic features of the drainage system, as shown in Table 2.

Table 5. Pre-processing outputs – Processing inputs

IFN		I/O file names (see subroutine OPENIO for unit IFN input)
IIN10	dem	DEM information (dem.dat)
IIN20	lakes_map	Map of lake cells (to be excluded by the domain)(lakes_map.dat)
IIN21	zone	Map of zone cells
IIN23	qoi_a	Vector containing the index of the cells ordered into descending elevation value
IIN25	dtm_w_1	Raster of the weights - cardinal
IIN26	dtm_w_2	Raster of the weights - diagonal direction
IIN27	dtm_p_outflow_1	Raster of the drainage directions - cardinal direction
IIN28	dtm_p_outflow_2	Raster of the drainage directions - diagonal direction
IIN29	dtm_local_slope_1	Raster of the local slopes - cardinal direction
IIN30	dtm_local_slope_2	Raster of the local slopes - diagonal direction
IIN31	dtm_epl_1	Raster of the elemental path length - cardinal direction
IIN32	dtm_epl_2	Raster of the elemental path length - diagonal direction
IIN33	dtm_kSs1_sf_1	Raster of surface roughness coefficient (ks) - cardinal direction
IIN34	dtm_kSs1_sf_2	Raster of surface roughness coefficient (ks) - diagonal direction
IIN35	dtm_Ws1_sf_1	Raster of surface water width - diagonal direction (Each value is the surface water width of the cells scaled in space and assigned to the cardinal drainage direction.)
IIN36	dtm_Ws1_sf_2	Raster of surface water width - cardinal direction (Each value is the surface water width of the cells scaled in space and assigned to the diagonal drainage direction.)
IIN37	dtm_b1_sf	Raster of at-a-station scaling coefficients for the surface water width (i.e., surface water width is scaled in time with a power-law function with that exponent).
IIN38	dtm_y1_sf	Raster of at-a-station scaling coefficients for the surface roughness (ks) coefficient

IIN39	dtm_nrc	Raster containing the number of rivulets per hillslope cell.

Since these files represent the input files for CATHY simulation, they must be in the same directory where other files required by the CATHY are.

It could be a good practise to create a “dataset” folder, which contains all the input/output files divided in pre-processing (for the output files of the pre-processing), input (for the other input files), and output (at the beginning it is an empty folder where the output files of CATHY simulation will be saved). Of course, this is just an idea; how to organize the input/output files is completely user's discretion. The important thing is that there is consistency between the dataset folder organization and the *cathy.fnames* file.

After this step, the pre-processing is finished, and the input files related to the mesh have been created in the *input* folder.

8.4 Processor CATHY

8.4.1 Input files for the processor CATHY and second mesh setup method

The input and output files required and generated by CATHY are listed in *cathy.fnames* file, as shown in *Figure 2*. In the first line of this file it is necessary to specify the position of these input/output files. In this file is it necessary to use backslash \ in Windows and forward slash / in Mac OS X.

The unit number associated to each input and output file (e.g. unit IIN1) are used by CATHY in reading and writing statements, respectively.

```
'..................... Directory ...................... /dataset'
'parm'                          unit IIN1
'grid'                          unit IIN2
'root_map'                      unit IIN3
'soil'                          unit IIN4
'ic'                            unit IIN5
'atmbc'                         unit IIN6
'sfbc'                          unit IIN7
'nansfdirbc'                    unit IIN8
'nansfneubc'                    unit IIN9
..............................................................................
..............................................................................

'output/enpsia'                 unit IOUT54
'output/ensubvol'               unit IOUT55
'output/enpsiz'                 unit IOUT56
'output/wtdepth'                unit IOUT57
'output/peatdef'                unit IOUTPT
'output/term'                   unit ITERM
(if ITERM=6 output is to terminal and this file is ignored)
```

Figure 1: Part of the cathy.fnames file

Some of these inputs are automatically generated during the pre-processing (*Table 2*), while others are new input files that should be updated with appropriate parameters for the specific case study (*Table 3*). All these files must be located, even empty, in the directory where you want to run the simulation, so the program can find them.

Table 6. Input files for the processor CATHY

IIN1	parm	Control parameters for the simulations FLOW3D and SURF_ROUTE
IIN2	grid	Grid info when they are different from the input DEM
IIN3	root_map	Raster map of the root zone depth
IIN4	soil	Soil parameter
IIN5	ic	Initial conditions
IIN6	atmbc	Atmospheric BC's (rainfall/evaporation rates)
IIN7	sfbc	Seepage face BC's
IIN8	nansfdirbc	Non-atmospheric, non-seepage face Dirichlet BC's (see subroutines BCONE and BCNXT for unit IIN8 input)
IIN9	nansfneubc	Non-atmospheric, non-seepage face Neumann BC's(see subroutines BCONE and BCNXT for unit IIN9 input)
IIN11	dem_parameters	DEM parameters and other parameters (if GRID=TRUE they can be found in the grid file)
IIN16	retctab	Soil characteristics in tabular data
IIN17	posizione_serb	Position of reservoirs and buffer cells (posizione_serb.dat)
IIN18	livelli_iniz_s	Initial levels in reservoirs (livelli_iniz_serb.dat)
IIN19		Depitting parameter epsilon (depit.dat)
IIN22	effraininp	Effective rainfall input file (this file is read only in the case of surface simulation)
IIN40	enkf	EnKF input
IIN50	nudging	Nudging input (see subroutines NUDONE and NUDNXT for unit IIN50 input)
IIN51	mesh	Mesh input file
IIN60	base_map	Raster map of the catchment impermeable basement.

The structural mesh of the case study presented in the thesis, was built externally using FeFlow.

When the importation method is chosen the procedure of the pre-processing is not required.

The two main files in case of mesh importing are found in the input folder: *mesh* and *grid.*

8.4.2 File *mesh*

The *mesh* file consists in the list of the (local) nodes coordinates, x, y and z, without any header on the top. The order of the lines corresponds to the order of the nodes, from 1 to *n,* the same rule applies also to all the other files.

```
0               14689.38995     88.20059685
9.60530409      14686.60909     88.16739449
4743.512485     23867.82699     158.3887641
5557.252342     24523.81379     160.9529432
8352.403592     25911.75879     118.6105216
982.4431571     16820.00247     94.16879919
1964.886314     18950.61498     96.42384163
3929.772629     23211.84001     150.8558727
```

The order of the rows assigns the order at the nodes too. In this case there are 8 nodes, identified with numbers that goes from 1 to 8, in order of appearance.

8.4.3 File *grid*

G*rid* file structure is more complex. Moreover, this file substitutes the file *dem_parameter*, necessary for the first procedure described with the pre-processing (file *dem_parameter* must be present in the input folder anyway). Here the *grid* file structure:

```
5       6       13      30        nzone   nveg   nstr   n1
7793    15183                     nnod    ntri
0       1       100.0             ivert   isp    base
0.02   0.02   0.02   0.04   0.05   0.05   0.05   0.05   0.05   0.05  0.05   0.05   0.05   0.05
0.05   0.05   0.05   0.05   0.2    zratio(i).i=1.nstr

88.2005968    88.1673944    158.388764    160.952942    118.610526   94.1687919 96.4238163
       150.855827    160.194591    17.3342003   177.526126   159.884224 56.0761928   50.7192731
       …  z(i). i=1.nnod

1288   350    355    1
752    435    1857   2
365    238    254    2
366    389    254    1
760    77     1288   5
829    1580   1581   4
760    782    200    3
1594   1596   1597   1
…                              (triang(i,k).i=1,4).k=1.ntri

0             14689.38995
9.6053041     14686.60909
4743.512485   23867.8269
5557.252342   24523.81379
8352.403592   25911.75879
982.4431572   16820.00247
1964.886314   18950.61498
3929.772629   23211.84001
…                              x(k).k=1.nnod   y(k).k=1.nnod

1
6
1
4
```

5	
2	
3	
2	
…	**`veg_type`**

Table 4: Grid file description.

Parameters	**Description**
nzone	Number of zones related to the vertical heterogeneity. See also file *soil*
nveg	Number of vegetation zone, horizontal heterogeneity. See also file *soil*
nstr	Layers number (1 less respect the number of slices)
n1	Maximum number of nodal connections
nnod	Surface nodes number
ntri	Surface triangles number of the 2D mesh
ivert	= 0 each layer will be parallel to the surface, including the base of the 3-d grid. ZRATIO is applied to each vertical cross section. = 1 base of the 3-d grid will be flat, and ZRATIO is applied to each vertical cross section = 2 base of the 3-d grid will be flat, as will the NSTR-1 horizontal cross sections above it. ZRATIO is applied only to the vertical cross section having the lowest elevation = 3 for each cell of the dem a single depth value is read in file input IIN60 (basement). ZRATIO is applied to each vertical cross section = 4 the first NSTR-1 layers from the surface will be parallel to the surface and the base of the 3-d grid will be flat. ZRATIO is applied only to the vertical cross section having the lowest elevation
isp	= 0 for flat surface layer (only one Z value is read in, and is replicated to all surface nodes) otherwise, surface layer is not flat (Z values read in for each surface node) (for ISP=0, IVERT=0, 1, and 2 yield the same 3-d mesh, given the same values of BASE and ZRATIO)
base	Value which defines the thickness or base of the 3-d mesh For IVERT=0, BASE is subtracted from each surface elevation value, so that each vertical cross section will be of thickness BASE, and the base of the 3-d mesh will be parallel to the surface. For IVERT=1 or 2, BASE is subtracted from the lowest

	surface elevation value, say ZMIN, so that each vertical cross section will be of thickness (Z - ZMIN) + BASE, where Z is the surface elevation for that cross section. The base of the 3-d mesh will thus be flat
zratio(i).i=1.nstr	Layers relative thickness (the sum is 1)
z(i).i=1.nnod	Surface nodes elevation (to be written in a single line in the correct order)
(triang(i,k).i=1,4).k=1.ntri	Nodes afferent to each triangle of the surface mesh, written line by line. The column will be 3. There can be a fourth column, as in the example, indicating the zone of vertical heterogeneity (see *Figure 1*)
x(k).k=1.nnod	X coordinate of each surface node
y(k).k=1.nnod	Y coordinate of each surface node
veg_type	Number of values equal to the number of the nodes, line by line. If the vegetation is homogeneous, the value will be a single value, equal to 1. In the case of study the vegetation classes are 6. See also file *soil*

The *nzone* parameter, related to the vertical heterogeneity, appears also in file soil.

To obtain the permeability distribution of *Figure 2* it was necessary to implement in the model the following configuration, introduced in the input model file *grid* and *soil.*

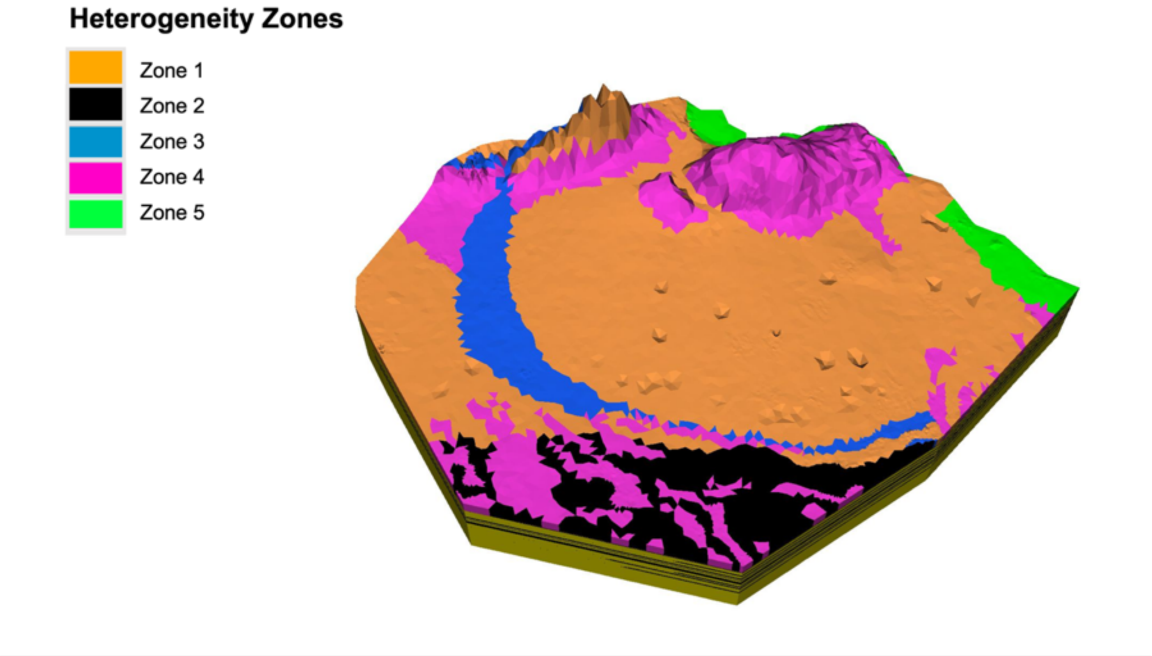

Figure 2: Vertical zones distribution implemented in CATHY, through the fourth column of parameter (triang(i,k).i=1,4).k=1.ntri, of file grid.

8.4.4 File *soil*

This file contains the information of the soil properties, the aquifer and aquitard layering together with the vertical heterogeneity, and the characteristics of the vegetation classes (PCANA, PCREF, PCULT, ZROOT, PZ, OMGC).

```
-6.40e+20                          PMIN
 0   1.0                           IPEAT SCF
 0.4 0.225                         CBETA0,CANG
 0.0 -4.0 -150.0 0.1  1.0 1.0      PCANA,PCREF,PCWLT,ZROOT,PZ,OMGC
 0.0 -4.0 -150.0 0.5  1.0 1.0      PCANA,PCREF,PCWLT,ZROOT,PZ,OMGC
 0.0 -4.0 -150.0 5.0  1.0 1.0      PCANA,PCREF,PCWLT,ZROOT,PZ,OMGC
 0.0 -4.0 -150.0 0.5  1.0 1.0      PCANA,PCREF,PCWLT,ZROOT,PZ,OMGC
 0.0 -4.0 -150.0 10.0 1.0 1.0      PCANA,PCREF,PCWLT,ZROOT,PZ,OMGC
 0.0 -4.0 -150.0 0.1  1.0 1.0      PCANA,PCREF,PCWLT,ZROOT,PZ,OMGC
 0                                 IVGHU
 0.02 2 2 0 0.333                  HUALFA,HUBETA,HUGAMA,HUPSIA,HUSWR
 1                                 HUN
-5 1                               HUA,HUB
 1.2 0 -0.345                      BCBETA,BCRMC,BCPSAT

5.00E-06     5.00E-06     5.00E-06     1.00E-03     0.58   1.88   0.065  0.1429
1.00E-06     1.00E-06     1.00E-06     1.00E-03     0.4    1.4    0.067  0.5882
5.00E-08     5.00E-08     5.00E-08     1.00E-03     0.58   1.88   0.065  0.1429     Block 1
5.00E-07     5.00E-07     5.00E-07     1.00E-03     0.58   1.88   0.065  0.1429
5.00E-05     5.00E-05     5.00E-05     1.00E-03     0.58   1.88   0.065  0.1429

5.00E-06     5.00E-06     5.00E-06     1.00E-03     0.58   1.88   0.065  0.1429
1.00E-06     1.00E-06     1.00E-06     1.00E-03     0.4    1.4    0.067  0.5882
5.00E-08     5.00E-08     5.00E-08     1.00E-03     0.58   1.88   0.065  0.1429     Block 2
5.00E-07     5.00E-07     5.00E-07     1.00E-03     0.58   1.88   0.065  0.1429
5.00E-05     5.00E-05     5.00E-05     1.00E-03     0.58   1.88   0.065  0.1429


 …            …          …         …              …      …      …      …

7.18E-03     7.18E-03     7.18E-03     1.00E-03     0.58   1.88   0.065  0.1429
7.18E-03     7.18E-03     7.18E-03     1.00E-03     0.58   1.88   0.065  0.1429
7.18E-03     7.18E-03     7.18E-03     1.00E-03     0.58   1.88   0.065  0.1429     Block 13
7.18E-03     7.18E-03     7.18E-03     1.00E-03     0.58   1.88   0.065  0.1429
7.18E-03     7.18E-03     7.18E-03     1.00E-03     0.58   1.88   0.065  0.1429
PERMX   PERMY   PERMZ   ELSTOR   POROS,   VGNCELL,   VGRMCCELL,   VGPSATCELL
```

Table 5: Soil file description.

Parameters	Description
PMIN	"Air dry" pressure head value (for switching control of atmospheric boundary conditions during evaporation)
IPEAT	Flag for peat soil deformation =0 constant porosity (in unsaturated soil) =1 consider porosity variations with water saturation
SCF	soil cover fraction (fraction of soil covered in vegetation)
CBETA0 , CANG	Parameters for Camporese adaptation of Pyatt and John relation for peat soil deformation
PCANA	Anaerobiosis point
PCREF	Field capacity
PCWLT	Wilting point
ZROOT	Mean root depth
PZ	Root distribution
OMGC	Humidity distribution
IVGHU	= -1 table look up for moisture curves = 0 for van Genuchten moisture curves = 1 for extended van Genuchten moisture curves = 2 for moisture curves from Huyakorn et al (WRR 20(8) 1984, WRR 22(13) 1986) with Kr=Se**n conductivity relationship = 3 for moisture curves from Huyakorn et al (WRR 20(8) 1984, WRR 22(13) 1986) with conductivity relationship from Table 3 of 1984 paper (log_10 Kr(Se) curve) = 4 for Brooks-Corey moisture curves
HUALFA, HUBETA, HUGAMA, HUPSIA, HUSWR, HUN, HUA, HUB,	Parameters for moisture curves from Huyakorn et al (WRR 20(8) 1984, WRR 22(13) 1986) (other 'HU' parameters - specific storage and porosity - are assigned nodally). HUN is only used for IVGHU=2; HUA and HUB are only used HUGAMA, for IVGHU=3. HUSWR is residual water saturation, which is equivalent to residual moisture content/porosity.
BCBETA, BCRMC, BCPSAT	Parameters for Brooks-Corey moisture curves (other 'BC' parameters - specific storage and porosity - are assigned nodally). BCRMC is residual moisture content
PERMX, PERMY, PERMZ	Hydraulic conductivity along the x, y and z directions
ELSTOR	Specific storage
POROS	Soil porosity

The aquifers and aquitards layering together with the vertical heterogeneity definition, in file *soil*, is given by the organization of lines containing the parameters PERMX PERMY PERMZ ELSTOR POROS, VGNCELL, VGRMCCELL, VGPSATCELL.

Suppose that the mesh we want to implement in CATHY has 13 layers (*nstr*, 1 less than the 14 slices), and 5 vertical classes (this last characteristic is implemented in *Figure 1* and in the fourth column of the parameter *(triang(i,k).i=1,4).k=1.ntri* of *grid* file). File *soil* will contain 13 blocks (number of layers) each one composed by 5 lines (number of zones). Each line will contain the properties of the specific soil that it is representing.

In the example of *soil* file structure is visible the first, the second and the thirteenth block, composed by 5 lines. According to the description of *Figure 22* of the thesis*,* zone 1 represents the *moderately high* hydraulic conductivity areas, zone 2 represents a clay layer in *risorgive* area, zone 3 the *low* hydraulic conductivity areas, zone 4 the *moderately low* hydraulic conductivity areas, and zone 5 the *high* hydraulic conductivity areas. This distinction is valid for the first three surface strata, where the indications of Veneto Region about the soil permeability are assumed. For the deeper layers the uniform calibrated *ks* is applied to all the zones.

8.4.5 File atmbc

The input file *atmbc* contains the atmospheric forcing of the model. In the case study the value is given by the sum of three quantities: rain, evapotranspiration (negative) and irrigation. The values must be expressed in m/s, in coherence with all the other data loaded.

```
0   1                         HSPATM IETO
0.0                           TIMEIN
1.669432608e-07
1.669432604e-07
1.497619766e-07
1.49258088e-07
1.504140486e-07
1.620782265e-07
1.574084306e-07
1.507196435e-07
…
```

Table 6: Atmbc file description.

Parameters	**Description**
HSPATM	= 0 for spatially variable atmospheric boundary condition inputs = blank or =9999 if unit IIN6 input is to be ignored = otherwise, atmospheric BC's are homogeneous in space
IETO	= 0 for linear interpolation of the atmospheric boundary condition inputs between different ATMTIM

	= otherwise, the inputs are assigned as a piecewise constant function (ietograph)
TIMEIN	Initial timestep (s)

After the definition of the initial timestep, in the case of the example, having decided to apply a spatially variable atmospheric boundary condition, the forcing value is listed line by line. There is a number of values equal to the number of the surface nodes. Then the second time step must be indicated, followed by a new series of data, and so on up to the final timestep. The time stepping is discretionary. A daily timestep was used in the example.

8.4.6 File *ic*

The file *ic* contains the initial condition of the model. In the study a first simulation was run by setting a uniform condition of water table depth, over all the domain, and the following simulations considering a spatially variable pressure condition, more realistic. Both the settings are presented:

```
4    0  INDP IPOND
5.0     WTPOSITION

------------------------

1    0  INDP IPOND
  -3.418053E+01  -3.314757E+01  -1.047180E+00  -4.094022E+01  -5.567600E+01
  -8.054471E+00  -9.297907E+00  -2.843338E-01  -1.641159E+01   1.116379E+00
  -3.028327E-01  -3.732052E+01  -6.610534E-01  -7.622365E+00  -6.394037E+00
  -2.807733E+00  -3.367099E+00  -1.088040E+01   1.176776E+01  -5.662458E-01
  -8.223668E-01  -2.007804E+01  -3.472677E+01  -3.248271E-01  -1.314105E+01
  -5.346584E+00  -5.091700E-01  -1.436889E+01  -7.606608E-01  -6.369637E-01
  -1.047365E+00  -6.224321E-01  -5.417474E+01  -1.783951E+00  -1.160369E+01
  -5.685667E-01  -1.226350E+00  -3.618940E+00  -4.258070E+00  -1.321500E+00
   5.793102E+00  -8.394724E+00  …
```

Table 7: Ic file description.

Parameters	**Description**
INDP	Flag for pressure head initial conditions (all nodes) = 0 for input of uniform initial conditions (one value read in) = 1 for input of non-uniform IC's (one value read in for each node) = 2 for calculation of fully saturated vertical hydrostatic equilibrium IC's (calculated in subroutine ICVHE). In the case of IPOND>0, the fully saturated hydrostatic IC is calculated (in subroutine ICVHEPOND) starting from the ponding head values at the surface nodes, rather than surface pressure heads of 0.

	= 3 for calculation of partially saturated vertical hydrostatic equilibrium IC's (calculated in subroutine ICVHWT) with the water table height (relative to the base of the 3-d grid) given by parameter WTHEIGHT = 4 for calculation of partially saturated vertical hydrostatic equilibrium IC's (calculated in subroutine ICVDWT) with the water table depth (relative to the surface of the 3-d grid) given by parameter WTPOSITION
IPOND	Flag for ponding head initial conditions (surface nodes) = 0 no input of ponding head initial conditions; otherwise (IPOND = 1 or 2) ponding head initial conditions are read into PONDNOD, and, where PONDNOD > 0, these values are used to update the surface node values in PTIMEP read in according to the previous INDP flag = 1 uniform ponding head initial conditions (one value read in) = 2 non-uniform ponding head initial conditions (one value read in for each node)
WTPOSITION	For the case INDP=4, specifies the initial water table height relative to the base of the 3-d grid

For the first simulation INDP is imposed equal to 4, and the water table position is set at a depth of 5m from the surface. No other data must be supplied. In the following simulation the value of INDP is 1, and the data to be supplied are obtained from the last timestep of the output *psi* file, that contains a value of pressure for each node of the 3D mesh.

```
 31235  3.14496000E+07    NSTEP   TIME
-3.418053E+01  -3.314757E+01  -1.047180E+00  -4.094022E+01  -5.567600E+01
-8.054471E+00  -9.297907E+00  -2.843338E-01  -1.641159E+01   1.116379E+00
-3.028327E-01  -3.732052E+01  -6.610534E-01  -7.622365E+00  -6.394037E+00
-2.807733E+00  -3.367099E+00  -1.088040E+01   1.176776E+01  -5.662458E-01
-8.223668E-01  -2.007804E+01  -3.472677E+01  -3.248271E-01  -1.314105E+01
-5.346584E+00  -5.091700E-01  -1.436889E+01  -7.606608E-01  -6.369637E-01
-1.047365E+00  -6.224321E-01  -5.417474E+01  -1.783951E+00  -1.160369E+01
-5.685667E-01  -1.226350E+00  -3.618940E+00  -4.258070E+00  -1.321500E+00
 5.793102E+00  -8.394724E+00  …
```

The values of pressure in all the nodes can be obtained by imposing the parameter IPRT in file *parm* equal to 1.

8.4.7 File *nansfdirbc*

The file *nansfdirbc* contains the Dirichlet boundary conditions of the model. These are condition in term of pressure head, defined on some of the domain perimeter nodes. If in some nodes no conditions are imposed (Dirichlet, Neumann or seepage face), CATHY assumes a no flow boundary condition, for those nodes.

```
0.0    TIME
0      1167    NDIR, NDIRIC
       64449         64540         64553         64556         64603         64604  64632
       64633         64644         64645         64646         64647  64648         64649
       64657         64665         64669         64675  64676         64680         …
       22.686        25.914        13.091        34.734        7.536         14.015  22.471
              26.793        5.179         12.831        4.882         21.53   13.889
              15.751        7.986         5.352         38.121        6.022
       21.908        26.034        …
```

Table 8: Nansfdirbc file description.

Parameters	Description
TIME	Initial timestep (s)
NDIR	Number of non-atmospheric, non-seepage face Dirichlet nodes in 2-d mesh. The BC's assigned to these surface nodes are replicated vertically (compare NDIRC). This value must always be 0.
NDIRIC	Total number of nodes in which at the current timestep the Dirichlet boundary condition is imposed

NDIRIC is followed by the list of the nodes numbers in which the Dirichlet boundary condition is imposed, reported in a line, followed by a line with the values of the Dirichlet boundary condition. The order of the nodes number and of the boundary condition must correspond. Then a new timestep can be indicated, new NDIR, NDIRIC and conditions on the nodes can be defined, up to the end of the simulation. The *nansfdirbc* file ends with the last timestep that contains a repetition of NDIR, NDIRIC and conditions of the previous one. Note that the Dirichlet boundary condition must be imposed only where the soil is saturated. If there is a negative value of pressure head this shouldn't be imposed.

8.4.8 File *nansfdirbc*

The file *nansfneubc* contains the Neumann boundary conditions of the model. This condition is represented by a flow rate that can be introduced in the domain (+) or extracted from it (-). The unit of measure of the flow rate must be in m^3/s. The structure of this input file is the same of the *nansfdirbc*.

```
0.0    TIME
0      165      ZERO, NQ
       7877         47045        8103          8093          8011          93710
       15674        39228       47021        15734       70265       54741
       39225        7886          132494        140287      101611      15800
       15851        31484        …
       -6.70e-03  -9.02e-03   -9.93e-04  -6.02e-03   -6.94e-03  -6.94e-03
       -2.84e-02  -1.22e-02   -4.89e-03  -1.97e-03   -1.97e-03  -1.38e-02
```

```
       -3.26e-03  -4.23e-03   -5.21e-03  -3.27e-02        -3.27e-03  -3.27e-03
       -1.96e-03  -1.96e-03   …
```

Table 9: Nansfneubc file description.

Parameters	Description
TIME	Initial timestep (s)
ZERO	This value must always be 0.
NQ	Total number of nodes in which at the current timestep the Neumann boundary condition is imposed

As for the *nansfdirbc* file, NQ is followed by the list of the nodes numbers in which the Neumann boundary condition is imposed, reported in a line, followed by a line with the values of the Neumann boundary condition. The order of the nodes number and of the boundary condition must correspond. Then a new timestep can be indicated, new NQ and conditions on the nodes can be defined, up to the end of the simulation.

8.4.9 File *parm*

File *parm* contains most of the simulation parameters, related to the time, to the output details, and other characteristics. When the CATHY folder is downloaded the file contains already the data of a generic case study, so it will be necessary to modify only some the following values.

```
-1          0          0                        IPRT1  NCOUT  TRAFLAG
 0          0.00       0                        ISIMGR PONDH_MIN VELREC
 0          0.01                                KSLOPE TOLKSL
-3.0       -1.0       -3.0       -1.0           PKRL   PKRR   PSEL   PSER
-3.0       -2.5       -1.5       -1.0           PDSE1L PDSE1R PDSE2L PDSE2R
 0          0          0                        ISFONE ISFCVG DUPUIT
 1          1          1                        TETAF  LUMP   IOPT
 0          0.8                                 NLRELX OMEGA
 0          5.0e-3     1.0e+30    1.0e+30       L2NORM TOLUNS TOLSWI  ERNLMX
 30         5          7                        ITUNS  ITUNS1 ITUNS2
 2          500        1.0e-06                  ISOLV  ITMXCG TOLCG
 1.0e+2    .00001      28800     36720000       DELTAT DTMIN  DTMAX  TMAX
 0.0        1.1        0.0      .5              DTMAGA DTMAGM DTREDS DTREDM
 1          0          166
7948800       8121600       8294400       8467200       8640000       8812800
8985600       9158400       9331200       9504000       9676800       9849600
…             …             …             …             …             …
34905600      35078400      35251200      35424000      35596800      35769600          35942400
       36115200      36288000     IPRT VTKF NPRT (TIMPR(I),I=1,NPRT)
19
15      35      40      41      49      51      103     109     115     119     121     141
```

```
159    191    198    229    237    243    249  NUMVP (NODVP(I), I=1, NUMVP)
0                         NR
1
16112                     NUM_QOUT (ID_QOUT(I),I=1,NUM_QOUT)
```

Only the main parameters will be commented and described.

Table 10: Parm file description.

Parameters	Description
IPRT1	Flag for output of input and coordinate data in subroutines DATIN and GEN3D = -1 reads in coordinates from file IIN51 (*mesh* input file) just after *grid* generation (in subroutine grdsys) = 0 prints parameters only (default) = 1 prints parameters + b.c. + geom. char. = 2 prints parameters + b.c. + geom. char. + grid info = 3 prints parameters + b.c. + geom. char. + grid info, X, Y, Z coordinate values in subroutine GEN3D, and then terminates program execution * This parameter must be set = 3 for the first run of the model. In this way the 3D mesh is generate by CATHY, and the output *xyz* is updated.
NCOUT	……….
TRAFLAG	Is the flag for the activation of the transport scheme = 0 the transport module is switched off = 1 the transport module is switched on
ISIMGR	Flag for type of simulation and type of surface grid =0 subsurface flow only (FLOW3D) with general triangular grid input =1 subsurface flow only (FLOW3D) with DEM input and triangular grid generated from this DEM =2 coupled subsurface flow (FLOW3D) and surface routing (SURF_ROUTE) with DEM input and triangular grid generated from this DEM =3 for surface flow (SURF_ROUTE) simulation with DEM input. The local contribution rate to surface runoff is directly read from effraininp input file by the subroutines EFFONE.f and EFFNXT.f.
PONDH_MIN	Minimum ponding head: if PNEW > PONDH_MIN, then at that node there is ponding; otherwise there is no ponding.
VELREC	………..

KSLOPE	= 0 for analytical differentiation of moisture curves = 1 for "chord slope" and analytical differentiation = 2 for "chord slope" and centered difference formulas = 3 for localized "chord slope" and analytical differentiation = 4 for localized "tangent slope" differentiation (the "chord slope" formula is the tangent approximation suggested by Huyakorn et al (WRR 20(8) 1984), wherein derivatives are approximated using pressure heads at the current and previous nonlinear iterations; "tangent slope" differentiation is a different tangent approximation wherein derivatives are approximated using pressure heads at the endpoints of a given range (eg: endpoints PKRL, PKRR for the derivative of relative hydraulic conductivity). For KSLOPE=1, 2 the chord slope formula is used at every iteration and at all nodes (with some exceptions as dictated by TOLKSL). For KSLOPE=3 or 4 the chord or tangent slope formulas are used only at those nodes whose pressure heads fall within given ranges (see PKRL, PKRR, etc), hence 'localized'; for nodes whose pressure heads fall outside these ranges, analytical differentiation is used.)
TOLKSL	Tolerance for chord slope formula. Whenever the chord slope formula is to be applied (for KSLOPE=1 or 2 at every iteration and at all nodes; for KSLOPE=3 at those nodes whose pressure heads fall within given ranges), it is applied only if the absolute pressure head difference (between the current and previous nonlinear iterations) is larger than TOLKSL. If the difference is smaller than TOLKSL, then differentiation is done either analytically (KSLOPE=1, 3) or with a centered difference formula (KSLOPE=2).
PKRL, PKRR	Left and right endpoints of the pressure head range within which the chord slope (case KSLOPE=3) or tangent slope (case KSLOPE=4) formula is used to evaluate the derivative of relative hydraulic conductivity
PSEL, PSER	Left and right endpoints of the pressure head range within which the chord slope (case KSLOPE=3) or tangent slope (case KSLOPE=4) formula is used to evaluate the derivative of effective saturation (moisture content for the case of extended van Genuchten curves, IVGHU=1)
PDSE1L, PDSE1R, PDSE2L, PDSE2R	Left and right endpoints of the two pressure head ranges within which the chord slope (case KSLOPE=3) or tangent slope (case KSLOPE=4) formula is used to evaluate the second derivative of effective saturation (moisture content for the case of extended van Genuchten curves, IVGHU=1). (Two ranges are specified since in general d(Se)/dP is non-monotonic.)
ISFONE	=0 seepage face exit point updating performed by checking all nodes on a seepage face
ISFCVG	=0 convergence of seepage face exit points is not a condition for convergence of the nonlinear iterative procedure

	=1 convergence of seepage face exit points is a condition for convergence of the nonlinear iterative procedure
DUPUIT	=0 all the nodes below the seepage face exit point are at atmospheric pressure =1 all the nodes below the seepage face exit point are at hydrostatic pressure. Caution: to use only if ISFONE=1!
TETAF	Weighting parameter for FLOW3D time stepping scheme (1.0 backward Euler; 0.5 Crank-Nicolson; TETAF is set to 1.0 for steady state problem).
LUMP	=0 for distributed mass matrix; otherwise matrix is lumped
IOPT	Iteration scheme to implement: =1 for Picard iteration scheme =2 for Newton iteration scheme
NLRELX	Flag for nonlinear relaxation =0 no relaxation =1 relaxation with constant relaxation parameter OMEGA =2 relaxation with iteration-dependent relaxation parameter OMEGA, calculated using Huyakorn et al's adaptation (WRR 1986 22(13), pg 1795) of Cooley's empirical scheme (WRR 1983 19(5), pg 1274)
OMEGA	Non-linear relaxation parameter: OMEGA > 1, over-relaxation; OMEGA < 1, under-relaxation. Input value of OMEGA is used only for the case NLRELX=1 (constant relaxation parameter). Input value of OMEGA is ignored otherwise: for NLRELX=0 relaxation is not applied; for NLRELX=2 OMEGA is calculated at each nonlinear FLOW3D iteration
L2NORM	=0 to use the infinity norm in the test for convergence of the nonlinear FLOW3D and coupled FLOW3D/SURF_ROUTE iterations; otherwise the L2 norm is used.
TOLUNS	Maximum nonlinear FLOW3D iterations per time step
TOLSWI	Tolerance for boundary condition switching check in FLOW3D iterations (switching check is only performed when PINF or PL2 are smaller than TOLSWI; so for e.g. if TOLSWI = TOLUNS, switching check is only performed after convergence and not after each iteration)
ERNLMX	Maximum allowable convergence or residual error in the nonlinear FLOW3D solution. If the convergence or residual errors become larger than ERNLMX, ERRGMX is set to TRUE and the code back-steps. This avoids occurrences of overflow or underflow when nonlinear iterations diverge.

In *parm* it must be specified the parameters related to the adaptive time-stepping approach implemented in the model. In particular the iteration bounds (ITUNS, ITUNS1, and ITUNS2), the initial DELTAT, the minimum DTMIN and the maximum DTMAX time step allowed for the computations, and the total time of the simulation TMAX.

TOLCG	Tolerance for convergence of conjugate gradient linear system solvers
ITUNS	Maximum nonlinear FLOW3D iterations per time step
ITUNS1	If ITER < ITUNS1, time step size is increased
ITUNS2	If ITUNS1 <= ITER < ITUNS2, time step size is not altered if ITUNS2 <= ITER < ITUNS, time step size is decreased if ITER = ITUNS (i.e., convergence not achieved in ITUNS iterations), we back-step unless time step size cannot be reduced any further (DELTAT = DTMIN). Back-stepping is also triggered if the linear solver failed (LSFAIL = TRUE) or if the convergence or residual errors become larger than ERNLMX (ERRGMX = TRUE).
ISOLV	Flag for non-symmetric linear solver = -5 BiCGSTAB (preconditioned with D^-1) = -4 BiCGSTAB (not preconditioned) = -3 TFQMR (preconditioned with D^-1) = -2 TFQMR (not preconditioned) = -1 TFQMR (preconditioned with K^-1) = 0 BiCGSTAB (preconditioned with K^-1) = 1 GRAMRB (minimum residual) = 2 GCRK(5) (ORTHOMIN) = 3 IBM's NONSYM (direct solver)
ITMXCG	Maximum number of iterations for conjugate gradient linear system solvers
TOLCG	Tolerance for convergence of conjugate gradient linear system solvers
DELTAT	Initial and current FLOW3D time step size. Its choice depends by the simulation resolution, in should be around 1/3 of that. In the example the simulation resolution is 1 day (86400s) and so daltat = 86400/3
DTMIN	Minimum FLOW3D time step size allowed
DTMAX	Maximum FLOW3D time step size allowed
TMAX	Final time of the simulation
DTMAGA	Magnification factor for FLOW3D time step size (additive)
DTMAGM	Magnification factor for FLOW3D time step size (multiplicative)
DTREDS	Reduction factor for FLOW3D time step size (subtractive)
DTREDM	Reduction factor for FLOW3D time step size (multiplicative)
IPRT	Flag for detailed output at all nodes and velocity and water saturation output at all elements (velocity and water saturation

	output in the case IPRT=4 can be used as input to TRAN3D and DUAL3D codes) =0 don't print nodal pressure, velocity, water saturation, or relative conductivity values =1 print only nodal pressure head values =2 print nodal pressure head and velocity values =3 print nodal pressure, velocity, and relative conductivity values =4 print nodal pressure, velocity, relative conductivity, and overall storage coefficient values, and print element velocity and nodal water saturation values
VTKF	Flag for detailed output. This flag allows the generation of the *.vtk* output files, in the respective folder. = 0 don't print nodal pressure, velocity, water saturation, or relative conductivity values = 1 print only nodal pressure head values = 2 print nodal pressure head and velocity values = 3 print nodal pressure, velocity, and water saturation = 4 print nodal pressure, velocity, water saturation and relative conductivity values
NPRT	Number of time values for detailed nodal output and element velocity
(TIMPR(I),I=1,NPRT)	Time values for detailed output. Detailed output is produced at initial conditions (TIME=0), at time values indicated in TIMPRT, and at the end of the simulation (TIME=TMAX). Detailed output consists of: values of pressure head, velocity, water saturation, and relative conductivity (depending on setting of IPRT) at all nodes; velocity, and water saturation (depending on setting of IPRT) at all elements; vertical profiles of pressure head, water saturation, and relative conductivity for the NODVP surface nodes; pressure head, water saturation, and SATSUR values at the surface nodes.
NUMVP	Number of surface nodes for vertical profile output
(NODVP(I), I=1, NUMVP)	Nodes number for surface nodes selected for vertical profile output
NUM_QOUT	Number of nodes for hydrograph output

8.4.10 File *dem_parameters*

In case the mesh to be used is regular, file *dem_parameters* can be used, instead of file *mesh* and file *grid*. In this file the resolution of the DEM must be specified through the parameters DELTA_X and DELTA_Y (these variables must appear without any comment between them). The resolution indicated in *dem_parameters* has to be set with the same grid spacing defined in the file *hap.in.*

In addition it is necessary to specify the numbers of material types in the porous media (NZONE), the number of vertical layers (NSTR), and their relative thickness (ZRATIO).

```
10. 10.                      delta_x delta_y
1.0e+0                       factor
1                            dostep
1  20   20                   nzone  nstr  n1
0  1   5                     ivert  isp   base
0.05 0.05 0.05 0.05 0.05
0.05 0.05 0.05 0.05 0.05
0.05 0.05 0.05 0.05 0.05
0.05 0.05 0.05 0.05 0.05     zratio(i),i=1,nstr
```

Table 11: Dem_parameters file description.

DELTA_X, DELTA_Y	Cell dimensions for the resolution of the DEM
FACTOR	Multiplicative factor for DEM values (e.g. to change the units of the elevation)
DOSTEP	Step adopted in coarsening the mesh
NZONE	The number of material types in the porous medium
NSTR	The number of vertical layers
N1	The maximum number of element connections to a node
ZRATIO (NSTR)	The thickness of vertical layers or the fraction of total grid height that each layer is to occupy (ZRATIO (1) is for the surface-most layer. ZRATIO values must sum to 1.)
IVERT	=0 each layer will be parallel to the surface, including the base of the 3-d grid. ZRATIO is applied to each vertical cross section. =1 base of the 3-d grid will be flat, and ZRATIO is applied to each vertical cross section =2 base of the 3-d grid will be flat, as will the NSTR-1 horizontal cross sections above it. ZRATIO is applied only to the vertical cross section having the lowest elevation. =3 for each cell of the dem a single depth value is read in file input IIN60 (basement). ZRATIO is applied to each vertical cross section. =4 the first NSTR-1 layers from the surface will be parallel to the surface and the base of the 3-d grid will be flat. ZRATIO is applied only to the vertical cross section having the lowest elevation.
ISP	=0 for flat surface layer (only one Z value is read in, and is replicated to all surface nodes); otherwise surface layer is not flat (Z values read in for each surface node);

	(for ISP=0, IVERT=0, 1, and 2 yield the same 3-d mesh, given the same values of BASE and ZRATIO).
BASE	Value which defines the thickness or base of the 3-d mesh. For IVERT=0, BASE is subtracted from each surface elevation value, so that each vertical cross section will be of thickness BASE, and the base of the 3-d mesh will be parallel to the surface. For IVERT=1 or 2, BASE is subtracted from the lowest surface elevation value, say ZMIN, so that each vertical cross section will be of thickness (Z - ZMIN) + BASE, where Z is the surface elevation for that cross section. The base of the 3-d mesh will thus be flat.
ZRATIO (NSTR)	The thickness of vertical layers or the fraction of total grid height that each layer is to occupy (ZRATIO (1) is for the surface-most layer. ZRATIO values must sum to 1.)

8.4.11 Other input files

In addition to the previously described input files, the processor CATHY needs of other input files that, even empty, must be located in the directory where you want to run the simulation, so the program can find them.

- **base_map**: raster map of the catchment impermeable basement (bedrock). Each value represents the thickness of the corresponding cell. It is used to define the catchment impermeable basement independently from the DEM; this happens when specific data are known.
- **effraininp**: effective rainfall input file (it is used by the subroutines effone.f and effnxt.f for the case of surface routing only).
- **enkf, nudging:** both of these input files contain data and are involved in the modeling when data assimilation (DA) schemes are used; otherwise they are empty files. The two DA schemes implemented in CATHY are dynamical relaxation (Newtonian nudging) and the ensamble Kalman filter (EnKF).
- **root_map**: contains the raster map of the root zone depth
- **retctab**: is used only if you want to use capillarity curves that are variable in space in the form of tabular data (soil characteristics in tabular data).
- **posizione_serb, livelli_iniz_s**: the first input file represents the position of reservoirs and buffer cells and the second input file represents the initial levels in reservoirs. Both of them are employed in the "lake boundary-following" procedure.

8.5 Running the processor CATHY

8.5.1 File CATHY.H

Defined all the parameters of the case study in the input files, also the *CATHT.H* file, in the *src* folder, must be updated. In this file it is necessary to indicate all the dimensions of the specific problem, like the number of surface mesh nodes, the number of layers, the number of nodes interested by the Dirichlet or Neumann boundary conditions, etc.

It is very important to do not exceed too much in the values actually needed for the specific problem for an accurate dimensioning of the problem. This allows you to allocate during the simulation the memory space that you actually need.

Below is presented the file section in which is necessary to update the information. This section, in file *CATHY.H*, is preceded by an explanation of each parameter meaning. The main parameters are highlighted in green.

```
PARAMETER (ROWMAX=90, COLMAX=90, DEMRES=1)
PARAMETER (MAXCEL=ROWMAX*COLMAX, MAXRES=1)
PARAMETER (NODMAX=(ROWMAX/DEMRES+1)*(COLMAX/DEMRES+1))
PARAMETER (NTRMAX=2*MAXCEL/(DEMRES*DEMRES))
PARAMETER (NP2MAX=3715, MAXSTR=19)
PARAMETER (NFACEMAX=187100)
PARAMETER (NMAX=NODMAX*(MAXSTR + 1), NTEMAX=3*NTRMAX*MAXSTR)
PARAMETER (NPMAX=74300, NPMAX_TRA=1, NQMAX=165, NSFMAX=1605)
PARAMETER (NNSFMX=5, MAXDIR=NODMAX+NPMAX+NSFMAX*NNSFMX)
PARAMETER (MAXNUDN=1, MAXNUDT=1, MAXNUDC=1)
PARAMETER (MAXZON=12, MAXTRM=1870500, MAXIT=30, MAXVEG=6)
PARAMETER (NRMAX=1, MAXPRT=137, MAXVP=105)
PARAMETER (N1MAX=30, NTPMAX=N1MAX*NMAX)
PARAMETER (MAXBOT=1, INTBOT=1, MAXQOUT=1)
PARAMETER (NIAUXMAX=NFACEMAX + MAXTRM + 1)
PARAMETER (NRAUXMAX=5*NFACEMAX + MAXTRM, NQMAX_TRA=NODMAX)
PARAMETER (NIAUXMAX=NMAX + MAXTRM + 1)
PARAMETER (NRAUXMAX=5*NMAX + MAXTRM, NQMAX_TRA=NODMAX)
PARAMETER (MAXVTKPRT=1)
PARAMETER (MAXFCONTONODE=100, MAXLKP=3)
```

Table 12: CATHY.H file description.

Parameters	**Description**
ROWMAX, COLMAX	In a mesh with a regular shape, they represent the maximum rows and column number of the surface layer. In a mesh with an irregular shape, they are 2 values whose multiplication give a number bigger or equal than the surface nodes number
DEMRES	coarsening factor for grid generation from DEM

MAXCEL	ROWMAX*COLMAX (maximum NCELL) NCELL = number of cells in the DEM of the catchment, including "lake" cells
MAXRES	maximum NUMRES, with NUMRES = number of 'reservoirs' defined in the DEM
NODMAX	maximum NNOD NNOD = number of nodes in 2-d mesh = number of surface nodes in 3-d mesh
NTRMAX	maximum NTRI NTRI = 2*NCELL when SURF_ROUTE is active, otherwise must be assigned explicitly = number of triangles in 2-d mesh
NP2MAX	maximum NDIR NDIR = number of non-atmospheric, non-seepage face Dirichlet nodes in 2-d mesh
MAXSTR	Maximum number of vertical layers (1 less respect the number of slices). See file grid
NFACEMAX	Number of tetrahedra faces. This value is given by the number of tetrahedra (NT, found after a first run in the output file risul) multiplied by 4
NMAX	NODMAX*(MAXSTR + 1) (maximum N) N = NNOD*(NSTR + 1) = number of nodes in 3-d mesh
NTEMAX	3*NTRMAX*MAXSTR (maximum NT) NT = 3*NTRI*NSTR = number of tetrahedra in 3-d mesh
NPMAX	maximum NP, NP = NDIR*(NSTR + 1) + NDIRC NP = total number of non-atmospheric, non-seepage face Dirichlet nodes in 3-d mesh NDIRC = number of 'fixed' non-atmospheric, non-seepage face Dirichlet nodes in 3-d mesh
NQMAX	Maximum number of nodes interested by the Neumann condition in the 3D mesh
NSFMAX	maximum NSF, with NSF = number of seepage faces
NNSFMX	maximum number of nodes on a seepage face + 1
MAXDIR	NODMAX + NPMAX + NSFMAX*NNSFMX (maximum NUMDIR)
MAXNUDN	maximum NUDT, with NUDT = number of observation times for nudging or EnKF
MAXNUDT	maximum NUDT, with NUDT = number of observation times for nudging or EnKF
MAXNUDC	maximum NUDC NUDC = number of concurrent observation datasets for nudging at any given time
MAXZON	Maximum number of zones (vertical heterogeneity). See file grid and soil

MAXTRM	Maximum number of nonzero elements in system matrices. This value has to be at list = (ROWMAX*COLMAX)*(NSTR+1)*10
MAXIT	maximum ITUNS, with ITUNS = maximum nonlinear FLOW3D iterations per time
MAXVEG	Maximum number of vegetation type (horizontal heterogeneity). See file grid and soil
NRMAX	maximum NR (ref. parm file), with NR = number of nodes selected for partial output
MAXPRT	Maximum time values for detailed output. See file parm (NPRT)
MAXVP	Maximum time values for vertical profile output. See file parm (NUMVP)
N1MAX	maximum N1 (it is good to have N1 ≤ 20) N1 = maximum number of element connections to a node
NTPMAX	N1MAX*NMAX
MAXBOT	maximum IBOT (defined real working storage dimension NONSYM solver) IBOT = size of real working storage for NONSYM solver
INTBOT	MAXBOT + 6*NMAX + 1 (defined integer working storage dimension for NONSYM solver) - Note: the values of MAXBOT and INTBOT should be set to 1 when NONSYM is not used
MAXQOUT	maximum NUM_QOUT, with NUM_QOUT = # of surface cells for discharge output

Once file *CATHY.H* has been filled in the right way, it is time to compile the CATHY processor in the Terminal/Command window. The executable file (**cathy_ft**) is generated through the compilation of the main program cathy.main.f and all the subprograms *.f and *.f90. From the *src* folder type:

`make clean` and then `make`

At this point the executable *cathy_ft* has been generated in *src* folder. To run the simulation, the executable must be copied in the same folder where *input, output, prepro* and *vtk* folders lie. Giving the command

```
./cathy_ft
```

the simulation will start.

Note that when "*segmentation error*" warning appears in the command window, probably at least one of the *CATHY.H* parameters has been underestimated!

8.6 Output files from the processor CATHY

Once the simulation has been successfully completed, the following output files are generated. These files are in ASCII format, and are generally constituted by a header, with the description of the data and columns of numbers. Some files can be empty, if in the input settings it was not require the specific results.

Table 17. Output files

IOUT1	debug	Debugging
IOUT2	risul	output of the simulation
IOUT3	xyz	X, Y, Z coordinate values
IOUT4	iter	Convergence behaviour and errors norms for each iteration of every time step
IOUT5	mbeconv	Mass balance and convergence behaviour at each time step (REL. MBE (%) should be as small as possible)
IOUT6	vp	Vertical profile output in fixed nodes
IOUT7	hgatmsf	Atmospheric and seepage face hydrograph output
IOUT8	hgnansf	Non-atmospheric, non-seepage face hydrograph output
IOUT9	hgflag	Detailed HGFLAG output (counter for anomalous, implausible, or erroneous atmospheric inflow, outflow, and runoff occurrences)
IOUT10	sfflag	Detailed SFFLAG output (counter for anomalous, implausible, or erroneous occurrences along seepage faces)
IOUT11	psi	Pressure head output at all nodes
IOUT12	velnod	Velocity output at all nodes (Transport)
IOUT13	sw	Water saturation output at all nodes (SW) for input to TRAN3D and DUAL3D groundwater contaminant transport
IOUT14	ckrw	Relative hydraulic conductivity output at all nodes
IOUT15	velelt	Velocity output at all elements, for input to TRAN3D and DUAL3D groundwater contaminant transport codes (Transport)
IOUT16	psisurf	Pressure head output at surface nodes
IOUT17	satsurf	SATSUR output at surface nodes
IOUT18	swsurf	Water saturatiom output at surface nodes
IOUT19	nansfdir	Non-atmospheric, non-seepage face Dirichlet BCs at each time step
IOUT20	nansfneu	Non-atmospheric, non-seepage face Neumann BCs at each time step
IOUT30	hgsfdet	Detailed seepage face hydrograph output (Incoming and outgoing flows at the seepage face)
IOUT31	hgnansfdirdet	Detailed non-atmospheric, non-seepage face Dirichlet hydrograph output
IOUT32	hgnansfneudet	Detailed non-atmospheric, non-seepage face Neumann hydrograph output
IOUT36	cumflowvol	Output of cumulative flow volumes VSFTOT, VNDTOT, VNNTOT, VNUDTOT, and VTOT
IOUT40	net.ris	SURF_ROUTE module input data (dem data, geometry data, etc.)
IOUT41	hgraph	Surface runoff hydrograph: plot the computed discharge at the outlet (streamflow)
IOUT42	pondhead	SURF_ROUTE ponding head output (Pond head superficial nodes)
IOUT43	dtcoupling	CPU, time stepping, iteration and other diagnostics of the surface and subsurface modules at each time step
IOUT44	recharge	Detailed recharge output (spatial map of recharge flux)

IOUT50	hgnudging	Detailed nudging "hydrograph" output
IOUT51	tsnudging	Detailed time series output of model results at the nudging observation points. For intercomparison with a model simulation without nudging, run the same simulation but with NUDG=0.0 or NUDEPS=0.0 (don't set NUDN=0 since NUDSMC cannot be calculated without the coordinates of the nudging observation points!), and plot the results in the IOUT51 output file from both runs, together with the NUDTIM and NUDVAL data from the nudging input file. (This output file is designed for NUDN <= 10; for NUDN > 10 the output will need re-structuring.)
IOUT52	enpsif	Detailed time series output of the ensemble of PNEW realizations before the update.
IOUT53	enqoutlet	Detailed time series output of the ensemble of outlet Q_OUT realizations after the update.
IOUT54	enpsia	Detailed time series output of the ensemble of PNEW realizations after the update.
IOUT55	ensubvol	Detailed time series output of the ensemble of subsurface water volume.
IOUT56	enpsiz	Ensemble parameters, initial conditions, weights and SIR updates
IOUT57	wtdepth	Water table depth (Time, WTDEPTH(NODVP(I)), I=1,2,...,NUMVP)
IOUTPT	peatdef	Void ratio output at all nodes in case of deformable peat
ITERM	term	Set ITERM to 6 in BLOCK DATA subprogram for terminal output; otherwise unit ITERM output is to a file
	grid2d.exp	Numbering of the grid (open with Argus1)
	grid3d	shows the 3d grid

8.7 Post-processing

Once obtain the CATHY output files, it is necessary to run the post-processing subroutines written in Matlab code to extract and view the results of the simulation. Visualizing the results is an important part of the analysis as it allows to assess the quality of the model and to analyze the parameters involved in the simulation. Running these different subroutines allows to visualize the performance of the variables contained in the output files that have been produced by the compiling of the CATHY processor.

References

Acquah S. J., Yan H. F., Zhang C., Wang G. Q., Zhao B. S., Wu H. M., 2018. *Application and evaluation of Stanghellini model in the determination of crop evapotranspiration in a naturally ventilated greenhouse*. International Journal of Agricultural & Biological Engineering; 11(6): 95–103. DOI:10.25165/j.ijabe.20181106.3972

Al-Thawadi S., 2020. *Microplastics and Nanoplastics in Aquatic Environments: Challenges and Threats to Aquatic Organisms.* Arabian Journal for Science and Engineering. Volume 45, pages 4419–4440 (2020). https://doi.org/10.1007/s13369-020-04402-z

Al-Hashimi O., Hashim K., Loffill E., Marolt Čebašek T., Nakouti I., Faisal A., Al-Ansari N., 2021. *A Comprehensive Review for Groundwater Contamination and Remediation: Occurrence, Migration and Adsorption Modelling*. Molecules (Basel, Switzerland), 26(19), 5913. https://doi.org/10.3390/molecules26195913

Aree di Salvaguardia ALLEGATI A0, A1, A2 DGR nr. 1621 del 05 novembre 2019. Piano di Tutela delle Acque, art. 15

ARPAV (2022). Consumo di suolo nella regione Veneto. https://www.arpa.veneto.it/temi-ambientali/suolo/file-e-allegati/documenti/consumo-di-suolo/consumo-di-suolo-nella-regione-veneto-nel-2021.pdf/@@display-file/file

Barbi A. (1), Cola G. (2), Mariani L. (2), 2011. *Inquadramento climatico del Veneto*. (1) Centro Meteorologico di Teolo (PD) ARPAV, Dipartimento Regionale Sicurezza del Territorio. (2) Dipartimento Produzioni Vegetali, Sezione Agronomia, Facoltà di Agraria Università degli Studi di Milano

Bartram J., Corrales L., Davison A., Deere D., Drury D., Gordon B., Howard G., Rinehold A., Stevens M.. *Water safety plan manual: step-by-step risk management for drinking-water suppliers*. World Health Organization. Geneva, 2009. ISBN 978 92 4 156263 8

Bause M., Schwegler K., 2013. *Higher order finite element approximation of systems of convection–diffusion–reaction equations with small diffusion*. Journal of Computational and Applied Mathematics 246, 52–64. http://dx.doi.org/doi:10.1016/j.cam.2012.07.005

Bizhanimanzar M., Leconte R., Nuth M., 2019. *Modelling of shallow water table dynamics using conceptual and physically based integrated surface-water–groundwater hydrologic models*. Hydrology and System Science, 23, 2245–2260. https://doi.org/10.5194/hess-23-2245-2019

Bizhanimanzar M., Leconte R., Nuth M., 2020. *Catchment-scale integrated surface water-groundwater hydrologic modelling using conceptual and physically based models: a model comparison study.* Water, 12, 363. https://www.mdpi.com/2073-4441/12/2/363

Brunner P., Simmons C.T., 2012. *HydroGeoSphere: a fully integrated, physically based hydrological model*. Groundwater, 50(2), 170-176. https://doi.org/10.1111/j.1745-6584.2011.00882.x

Camporese M., Daly E., Paniconi C., 2015. *Catchment-scale Richards equation-based modeling of evapotranspiration via boundary condition switching and root water uptake schemes*. Water Resources Research 51, 5756–5771, https://doi.org/10.1002/2015WR017139

Camporese M., Paniconi C., Putti M., Salandin P., 2009a. *Ensemble Kalman filter data assimilation for a processbased catchment scale model of surface and subsurface flow.* Water Resources Research, volume 45, W10421. https://doi.org/10.1029/2008WR007031

Camporese M., Paniconi C., Putti M., Salandin P., 2009b. *Comparison of Data Assimilation Techniques for a Coupled Model of Surface and Subsurface Flow*. Vadose Zone Jurnal, 8:837–845. https://doi.org/10.2136/vzj2009.0018

Camporese M., Paniconi C., Putti M., Orlandini S., 2010. *Surface-subsurface flow modeling with path-based runoff routing, boundary condition-based coupling, and assimilation of multisource observation data.* Water Resources Research 46 (2), W02512. http://dx.doi.org/doi:10.1029/2008WR007536

Camporese M., Daly E., Dresel P. E., Webb J. A, 2014. *Simplified modeling of catchment-scale evapotranspiration via boundary condition switching*. Advances in Water Resources, Volume 69, Pages 95-105, ISSN 0309-1708. https://doi.org/10.1016/j.advwatres.2014.04.008

Carsel R. F., Parrish R. S., 1988. *Developing Joint Probability Distributions of Soil Water Retention Characteristics*. Water resources research, vol. 24, No. 5, pages 755-769. https://doi.org/10.1029/WR024i005p00755

Chicco D., Warrens M. J., Jurman G., 2021. *The coefficient of determination R-squared is more informative than SMAPE, MAE, MAPE, MSE and RMSE in regression analysis evaluation.* PeerJ Computer Science. https://peerj.com/articles/cs-623/

Dal Prà A., Martignago G., Niceforo U., Tamaro M., Vielmo A., ZanninA., 1996. *Il contributo delle acque irrigue alla ricarica delle falde nella pianura alluvionale tra Brenta e Piave*. L'Acqua n° 4. https://www.idrotecnicaitaliana.it/wp-content/uploads/2021/01/DalPra-et-al.-LAcqua-n.-4-1996.pdf

Daneshmand H., Alaghmand S., Camporese M., Talei A., Daly E., 2019. *Water and salt balance modelling of intermittent catchments using a physically-based integrated model.* Journal of Hydrology 568, 1017–1030. http://dx.doi.org/doi:10.1016/j.jhydrol.2018.11.035

de Melo M. L. A, de Jong van Lier Q., 2021. *Revisiting the Feddes reduction function for modeling root water uptake and crop transpiration*. Journal of Hydrology, Volume 603, Part B, 126952, ISSN 0022-1694. https://doi.org/10.1016/j.jhydrol.2021.126952

Diersch H. J., 2013. FEFLOW—Finite Element Modeling of Flow, Mass and Heat Transport in Porous and Fractured Media. DOI: 10.1007/978-3-642-38739-5

Decreto del Ministero dell'Ambiente e della Tutela e del Territorio e del Mare, 30/2017 (Deflussi Ecologici)

Decreto legislative 152/2006

Dettori M., Arghittu A., Deiana G., Castiglia P., Azara A., 2022. *The revised European Directive 2020/2184 on the quality of water intended for human consumption. A step forward in risk assessment, consumer safety and informative communication*. Environmental Research, Volume 209, 112773, ISSN 0013-9351. https://doi.org/10.1016/j.envres.2022.112773

Diersch H.J, FEFLOW - *Finite Element Modeling of Flow, Mass and Heat Transport in Porous and Fractured Media*. Springer, 2014

Duan Q., Sorooshhian S., Gupta V. K., 1994. *Optimal use of the SCE-UA global optimization method for calibrating watershed models*. Journal of Hydrology 158, 265-284. https://doi.org/10.1016/0022-1694(94)90057-4

Doherty, J., 2015. *Calibration and Uncertainty Analysis for Complex Environmental Models*. Watermark Numerical Computing, Brisbane, Australia. ISBN: 978-0-9943786-0-6.

Ebele A. J., Abdallah M. A. E., Harrad S., 2017. *Pharmaceuticals and personal care products (PPCPs) in the freshwater aquatic environment.* Emerging Contaminants, Volume 3, Issue 1, 2017, Pages 1-16, ISSN 2405-6650, https://doi.org/10.1016/j.emcon.2016.12.004

Edmunds, W. M. & Shand, P. (2008). Natural Groundwater Quality. Blackwell Publishing Ltd

Famiglietti J., 2014. *The global groundwater crisis*. Nature Climate Change, 4, DOI: 10.1038/nclimate2425

Fatichi S., Vivoni E. R., Ogden F. L., Ivanov L. Y., Mirus B., Gochis D., Downer C. W., Camporese M., Davison J. H., Ebel B., Jones N., Kim J., Mascaro G., Niswonger R., Restrepo P., Rigon R., Shen C., Sulis M., Tarboton D., 2016. An overview of current applications, challenges, and future trends in distributed process-based models in hydrology. Journal of Hydrology 537, 45-60. http://dx.doi.org/doi:10.1016/j.jhydrol.2016.03.026

Feddes R. A., Kowalik P., Kolinska-Malinka K., Zaradny H., (1976). *Simulation of field water uptake by plants using a soil water dependent root extraction function*. Journal of Hydrology, 31, 13–26. https://doi.org/10.1016/0022-1694(76)90017-2

Flint A. L., Childs S. W., 1991. *Use of the Priestley-Taylor evaporation equation for soil water limited conditions in a small forest clearcut*. Agricultural and Forest Meteorology, Volume 56, Issues 3–4, Pages 247-260, ISSN 0168-1923, https://doi.org/10.1016/0168-1923(91)90094-7

Freeze R.A., Cherry J.A., 1979. *Groundwater*. Prentice-Hall, Englewood Cliffs, New Jersey

Gatel, L., Lauvernet, C., Carluer, N., Weill, S., Paniconi, C., 2020. *Sobol global sensitivity analysis of a coupled surface/subsurface water flow and reactive solute transfer model on a real hillslope*. Water 12 (1), 121. https://doi.org/10.3390/w12010121.

Gatel, L., Lauvernet, C., Carluer, N., Weill, S., Tournebize, J., Paniconi, C., 2019. *Global evaluation and sensitivity analysis of a physically based flow and reactive transport model on a laboratory experiment*. Environmental Modelling & Software, 113, 73–83. https://doi.org/10.1016/j.envsoft.2018.12.006.

Ghiat I., Mackey H.R., Al-Ansari T., 2021. *A Review of Evapotranspiration Measurement Models, Techniques and Methods for Open and Closed Agricultural Field Applications*. Water, 13, 2523. https://doi.org/10.3390/w13182523

Gleick P., Cooley He., 2021. *Freshwater Scarcity*. Annual Review of Environment and Resources. 46. 10.1146/annurev-environ-012220-101319. https://www.annualreviews.org/doi/pdf/10.1146/annurev-environ-012220-101319

Gresho P.M., Sani R., 1998. *Incompressible Flow and the Finite Element Method: Advection-Diffusion and Isothermal Laminar Flow.* John Wiley

Gumuła-Kawęcka A., Jaworska-Szulc B., Szymkiewicz A., Gorczewska-Langner W., Pruszkowska-Caceres M., Angulo-Jaramillo R., Šimůnek J., 2022. *Estimation of groundwater recharge in a shallow sandy aquifer using unsaturated zone modeling and water table fluctuation method.* Journal of Hydrology, Volume 605, 127283, ISSN 0022-1694, https://doi.org/10.1016/j.jhydrol.2021.127283

Haque A., Salama A., Lo k., Wu P., 2021. *Development of an integrated numerical flow model in the Prairie Environment – A case study of the Leech Lake Aquifer system, Saskatchewan, Canada*. Journal of Hydrology: Regional Studies 36, 100869. https://doi.org/10.1016/j.ejrh.2021.100869

Hargreaves G. H., Samani Z. A., 1985. *Reference crop evapotranspiration from temperature*. Applied Engineering in Agriculture. 1(2): 96-99. doi: 10.13031/2013.26773) @1985

Holland H.H., 1975. *Adaptation in natural and artificial systems*. University of Michigan Press, Ann Arbor.

Hossain M. F., 2019. *Sustainable design and building*. Chapter Six – Water. Page 301-418. https://doi.org/10.1016/B978-0-12-816722-9.00006-9

Hossein T., Kaveh O. A. A., 2022. *Hydro geo-sphere integrated hydrologic model in modeling of wide basins*. Sustainable Water Resources Management 8:118. https://doi.org/10.1007/s40899-022-00689-y

IRSA-CNR, Gruppo di studio sulle falde acquifere profonde della pianura Padana (1976). Indagine sulle falde aquifere profonde della pianura Padana. Quaderni dell'Istituto di Ricerca sulle Acque, 28, II

Jeon D. J., Ligaray M., Kim M., Kim G., Lee G., Pachepsky Y. A., Cha D. H., Cho K. H., 2019. *Evaluating the influence of climate change on the fate and transport of fecal coliform bacteria using the* *modified SWAT model*. Science of The Total Environment,Volume 658, Pages 753-762, ISSN 0048-9697. https://doi.org/10.1016/j.scitotenv.2018.12.21

Khorram-Manesh A, 2015. *Preparedness for Chemical Threats; New Challenges in Management of Trauma and Disasters.* Bull Emerg Trauma, 3(4):115-117. https://www.ncbi.nlm.nih.gov/pmc/articles/PMC4771303/

Knoben W. J. M., Freer J. E., Woods R. A., 2019. *Technical note: Inherent benchmark or not? Comparing Nash–Sutcliffe and Kling–Gupta efficiency scores*. Hydrology Earth System Science, 23, 4323–4331. https://doi.org/10.5194/hess-23-4323-2019

Kollet S.J., Maxwell R.M., 2006. *Integrated surface–groundwater flow modeling: a free surface overland flow boundary condition in a parallel groundwater flow model.* Advances in Water Resources 29 (7), 945–958. http://dx.doi.org/doi:10.1016/j.advwatres.2005.08.006

Kollet, S., et al., 2017. *The integrated hydrologic model intercomparison project, IH-MIP2: A second set of benchmark results to diagnose integrated hydrology and feedbacks*. Water Resources Research, 53, 867– 890, doi:10.1002/2016WR019191.

Konikow L.F., Kendy E., 2005. *Groundwater depletion: A global problem*. Hydrogeology Journal, 13, 317–320. https://doi.org/10.1007/s10040-004-0411-8

Levizzari R., 2017. *Caratterizzazione e monitoraggio della zona non satura per lo sviluppo del deposito nazionale di rifiuti radioattivi*. Centro Ricerche Bologna

Liggett J.E., Partington D., Frei D., Werner A.D., Simmons C.T., Fleckenstein J.H., 2015. *An exploration of coupled surface–subsurface solute transport in a fully integrated catchment model*. Journal of Hydrology 529, 969–979. http://dx.doi.org/doi:10.1016/j.jhydrol.2015.09.006

Liggett J.E., Werner A.D., Smerdon B.D., Partington D., Simmons C.T., 2014. *Fully integrated modeling of surface-subsurface solute transport and the effect of dispersion in tracer hydrograph separation*. Water Resources Research 50, 7750–7765. http://dx.doi.org/doi:10.1002/2013WR015040

Ling E. N., Lwanga E. H., Eldridge S. M., Johnston P., Hu H., W., Geissen V., Chen D., 2018. *An overview of microplastic and nanoplastic pollution in agroecosystems.* Science of the total environment, Volume 627, pages 1377-1388. https://doi.org/10.1016/j.scitotenv.2018.01.341

Long S.A., Tachiev G.I., Fennema R., Cook A.M., Sukop M.C., Wilhelm M.F., 2015. *Modeling the impact of restoration efforts on phosphorus loading and transport through Everglades National Park, FL, USA*. Science of the Total Environment 520, 81–95. http://dx.doi.org/doi:10.1016/j.scitotenv.2015.01.094

Lucentini L., Achene L., Fuscoletti V., Nigro Di Gregorio V., Pettine P., 2021. *Linee guida per la valutazione e gestione del rischio nella filiera delle acque destinate al consumo umano secondo il modello dei Water Safety Plans*. Istituto Superiore di Sanità, Rapporti ISTISAN 14/21 https://www.iss.it/documents/20126/45616/14_21_web.pdf/68c7940a-acd9-3569-fe07-af3fac298a79?t=1581095415282

Mahlalela P.T., Blamey R.C., Reason C.J.C., 2019. *Mechanisms behind early winter rainfall variability in the southwestern Cape, South Africa*. Climate Dynamics 53, 21–39. https://doi.org/10.1007/s00382-018-4571-y

Maxwell, R.M., et al., 2014. *Surface-subsurface model intercomparison: A first set of benchmark results to diagnose integrated hydrology and feedbacks*. Water Resources Rersearch, 50, 1531– 1549, doi:10.1002/2013WR013725.

Maxwell R., Condon L., Kollet S., 2015. *A high-resolution simulation of groundwater and surface water over most of the continental US with the integrated hydrologic model ParFlow v3*. Geoscientific Model Development 8 (3), 923–937. https://doi.org/10.5194/gmd-8-923-2015

Mazzia A., Bergamaschi L., Putti M., 2000. *A time-splitting technique for the advection-dispersion equation in groundwater*. Journal of Computational Physics*,* 157, 181–198. https://doi.org/10.1006/jcph.1999.6370

Mazzia A., Putti M., 2005. *High order Godunov mixed methods on tetrahedral meshes for density driven flow simulations in porous media*. Journal of Computational Physics*,* 208 (1), 154-174. https://doi.org/10.1016/j.jcp.2005.01.029

McNaughton K.G., Jarvis P.G, 1984. *Using the Penman-Monteith equation predictively*. Agricultural Water Management, Volume 8, Issues 1–3, Pages 263-278, ISSN 0378-3774, https://doi.org/10.1016/0378-3774(84)90057-X

Mesfin M., Arjen Y. H., 2016. *Four billion people facing severe water scarcity*. Science Advances, vol. 2, Issue 2. https://www.science.org/doi/10.1126/sciadv.1500323

Mesfin M. M., Winnie G. L., 2020. *The Water Footprint of Global Food Production*. Water 12 (10). https://doi.org/10.3390/w12102696

Monteith, J. L. 1965. *Evaporation and Environment. In: The state and movement of water in living organism*. 19th Symp. Soc. Exptl. Biol. P. 205-234.

Muma M., Gumiere S. J., Rousseau A. N., Scudeler C., Paniconi C., 2013. *Implementation of a root water extraction module in CATHY: Comparison of four empirical root-density distribution models*. Procedia Environmental Sciences 19 57 – 66. https://doi.org/10.1016/j.proenv.2013.06.007

Nelder J. A. and Mead R., 1965. *A simplex method for function minimization*. The Computer Journal, 7(4), 308-313. https://doi.org/10.1093/comjnl/7.4.308

Noye B.J., Hayman K., 1985. *Accurate finite difference methods for solving the advection-diffusion equation, in Computational Techniques and Applications: CTAC-85*. Edited by B. J. Noye and R. May, pp. 137–157, North-Holland, New York

Osiemo M. M., Ogendi G. M., M'Erimba C., 2019. *Microbial Quality of Drinking Water and Prevalence of Water-Related Diseases in Marigat Urban Centre, Kenya*. Environ Health Insights. doi: 10.1177/1178630219836988

Paniconi C., Putti M., 2015. *Physically based modeling in catchment hydrology at 50: Survey and outlook.* Water Resources Rersearch, 51(9), 7090–7129. https://doi.org/10.1002/2015WR017780

Pathania T., Eldho T.I., Bottacin-Busolin A., 2020. *Coupled simulation of groundwater flow and multispecies reactive transport in an unconfined aquifer using the element-free Galerkin method.* Engineering Analysis with Boundary Elements, 121, 31-49. http://dx.doi.org/doi:10.1016/j.enganabound.2020.08.019

Penman, H. L. 1948. *Natural evaporation from open water, bare soil and grass. Proceedings of the Royal Society of London*. Series A, Mathematical and Physical Sciences, Vol. 193, No. 1032, p. 120-145. https://doi.org/10.1098/rspa.1948.0037

Pertti A., Chris S., Hailong W., Doerthe T., 2017. *Integrated surface-subsurface model to investigate the role of groundwater in headwater catchment runoff generation: A minimalist approach to parameterisation*. Journal of Hydrology 547 664–677. http://creativecommons.org/licenses/by/4.0/

Piccinini L., Fabbri P., Pola M., Marcolongo E., 2017. *An example of aquifer heterogeneity simulation to modeling well-head protection areas*. Italian Journal of Engineering Geology and Environment 2017(Special Issue 2017):103-115 DOI:10.4408/IJEGE.2017-01.S-10

Poeter E., Fan Y., Cherry J., Wood W., Mackay D., 2020. *Groundwater in our water cycle – getting to know Earth's most important fresh water source.* The groundwater project, Guelph, Ontario, Canada https://books.gw-project.org/groundwater-in-our-water-cycle/

Price W. L., 1987. *Global optimization algorithms for a CAD workstation.* Journal of Optimtimization Theory and Applications, 55(1), 133-146. https://doi.org/10.1007/BF00939049

Priestley C. H. B., Taylor R. J., 1972. *On the Assessment of Surface Heat Flux and Evaporation Using Large-Scale Parameters*
https://doi.org/10.1175/1520-0493(1972)100<0081:OTAOSH>2.3.CO;2

Radu F.A., Suciu N., Hoffmann J., Vogel A., Kolditz O., Park C.H., Attinger S., 2011. *Accuracy of numerical simulations of contaminant transport in heterogeneous aquifers: A comparative study*. Advances in Water Resources 34, 47–61. http://dx.doi.org/doi:10.1016/j.advwatres.2010.09.012

Reszler C., Fank J., 2016. *Unsaturated zone flow and solute transport modelling with MIKE SHE: model test and parameter sensitivity analysis using lysimeter data*. Environmental Earth Science 75, 253. DOI 10.1007/s12665-015-4881-x https://link.springer.com/article/10.1007/s12665-015-4881-x

Reid R. A., Koljonen E. L., Buell J., B., 2007. *The deming cycle provides a framework for managing environmentally responsible process improvements*. Quality Engineering, Volume 12, pages 199-209.
https://doi.org/10.1080/08982119908962577

Richts A., Vrba J. 2016. *Groundwater resources and hydroclimatic extremes: mapping global groundwater vulnerability to floods and droughts*. Environmental Earth Sciences, volume 75, Article number: 926. DOI 10.1007/s12665-016-5632-3

Rossi L., Naumann G., Gabellani S., Cammalleri C., 2023. *A combined index to characterize agricultural drought in Italy at municipality scale.* Journal of Hydrology: Regional Studies. Volume 47, 101404, ISSN 2214-5818. https://doi.org/10.1016/j.ejrh.2023.101404

Scudeler C., Putti M., Paniconi C., 2016a. *Mass-conservative reconstruction of Galerkin* *velocity fields for transport simulations.* Advances in Water Resources 94, 470–485. http://dx.doi.org/doi:10.1016/j.advwatres.2016.06.011

Scudeler C., Pangle L., Pasetto D., Niu G.Y., Volkmann T., Paniconi C., Putti M., Troch P., 2016b. *Multiresponse modeling of variably saturated flow and isotope tracer transport for a hillslope experiment at the Landscape Evolution Observatory.* Hydrology and Earth System Sciences, 20, 4061–4078. http://dx.doi.org/doi:10.5194/hess-20-4061-2016

Şen Z., 2015. *Climate Change, Droughts, and Water Resources.* Applied Drought Modeling, Prediction, and Mitigation, pages 321-391. https://doi.org/10.1016/B978-0-12-802176-7.00006-7

Shen C., Phanikumar M.S., 2010. *A process-based, distributed hydrologic model based on a large-scale method for surface-subsurface coupling*. Advances in Water Resources 33 (12), 1524–1541. https://doi.org/10.1016/j.advwatres.2010.09.002

Shiklomanov's I., 1993. *Water in Crisis: A Guide to the World's Fresh Water Resources*. Peter H. Gleick (editor). https://www.usgs.gov/media/images/distribution-water-and-above-earth

Shoarinezhad V., Wieprecht S., Haun S., 2020. *Comparison of Local and Global Optimization Methods for Calibration of a 3D Morphodynamic Model of a Curved Channel*. Water, 12(5), 1333; https://doi.org/10.3390/w12051333

Stanghellini C., 1980. *Estimation of energy requirement for evaporation in greenhouses.* Symposium on More Profitable Use of Energy in Protected Cultivation. 10.17660/ActaHortic.1981.115.78

Suciu N., Radu F.A., Prechtel A., Brunner F., Knabner P., 2013. *A coupled finite element–global random walk approach to advection-dominated transport in porous media with random hydraulic conductivity*. Journal of Computational and Applied Mathematics 246, 27–37. http://dx.doi.org/doi:10.1016/j.cam.2012.06.027

L. Surinaidu, 2022. *Quantifying stream flows and groundwater response under the climate and land use change through integrated hydrological modelling in a South Indian River basin.* Water Security 17, 100129. https://doi.org/10.1016/j.wasec.2022.100129

Thornthwaite C. W., Mather J. R., 1951. *The role of evapotranspiration in climate*. Archiv für Meteorologie, Geophysik und Bioklimatologie, Serie B volume 3, pages 16–39. https://doi.org/10.1007/BF02242588

Trefry M. G., Muffels C., 2007. *FEFLOW: A Finite-Element Ground Water Flow and Transport Modeling Tool*. Groundwater, 45, 525-528. https://doi.org/10.1111/j.1745-6584.2007.00358.x

Trentin T., 2020. *Analisi quantitativa e qualitativa delle falde nell'alta pianura veneta, tra Treviso, Padova e Venezia.* PhD thesis from the University of Padova

Van Genuchten M. T., 1980. *A closed-form equation for predicting the hydraulic conductivity of unsaturated soil*s. Soil Science Society of America Journal, 44, 892-898. https://doi.org/10.2136/sssaj1980.03615995004400050002x

Visconti A., 2015. *La Pianura Padana Irrigua: storia e prospettive*. Treccani, La cultura italiana.

Water Directive 2000/60/CE

Watson S.J., Barry D.A., 2001. *Numerical analysis of stable brine displacements for evaluation of density-dependent flow theory*. Physics and Chemistry of the Earth, Part B: Hydrology, Oceans and Atmosphere, 26, 325– 331. http://dx.doi.org/doi:10.1016/S1464-1909(01)00014-4

Weill S., Mazzia A., Putti M., Paniconi C., 2011. *Coupling water flow and solute transport into a physically-based surface–subsurface hydrological model*. Advances in Water Resources 34, 128–136. http://dx.doi.org/doi:10.1016/j.advwatres.2010.10.001

Woods J.A., Teubner M.D., Simmons C.T., Narayan K.A., 2003. *Numerical error in groundwater flow and solute transport simulation.* Water Resources Research, 39(6), 1158. http://dx.doi.org/doi:10.1029/2001WR000586

Wu H., Fu P., Morris J.P., Settgast R.R., Ryerson F.J., 2019. *ICAT: A numerical scheme to minimize numerical diffusion in advection-dispersion modeling and its application in identifying flow channeling.* Advances in Water Resources 134, 103434. http://dx.doi.org/doi:10.1016/j.advwatres.2019.103434

Xiong H., Wang Y., Guo X., Han J., Ma C., Zhang X., 2022. *Current status and future challenges of groundwater vulnerability assessment: A bibliometric analysis*. Journal of Hydrology. 615 128694. https://doi.org/10.1016/j.jhydrol.2022.128694

Yang X., You X., 2013. *Estimating Parameters of Van Genuchten Model for Soil Water Retention Curve by Intelligent Algorithms*. Applied Mathematics & Information Sciences 7, No. 5, 1977-1983. http://dx.doi.org/10.12785/amis/070537

Web References

- https://www.consorziobacchiglione.it/consorzio.php?id=13 (26/04/2022)

- https://www.worldwildlife.org/threats/water-scarcity (28/04/2022)

-https://www.euro.who.int/en/health-topics/environment-and-health/water-and-sanitation/water-safety-plans (28/04/2022)

-https://www.usgs.gov/special-topics/water-science-school/science/groundwater-decline-and-depletion (15/05/2022)

- https://www.dw.com/en/are-we-running-out-of-fresh-water/a-40241057 (06/06/2022)

-http://www.feflow.info/html/help71/fepest/03_Estimation/Concepts/pest_algorithm.html (07/06/2022)

-http://userguide.cloudveneto.it/en/latest/Overview.html (22/06/2022)

-https://www.trevisotoday.it/green/veneto-acqua-irrigazione-consorzio-piave-2021.html (15/07/2022)

-https://www.nature.com/articles/d43978-022-00089-y (27/03/2023)

-http://www.liferisorgive.it/en/partners/brenta-consortium-for-land-reclamation/ (24/03/2023)

-https://altotrevigianoservizi.it/p/ats/chi-siamo (19/04/2023)

- https://www.youbuildweb.it/2022/03/10/drenaggio-le-regole-per-un-corretto-calcolo-della-permeabilita-delle-pavimentazioni/ (28/03/2023)

- https://agupubs.onlinelibrary.wiley.com/doi/full/10.1029/2008WR007536 (25/05/2023)

- http://userguide.cloudveneto.it/en/latest/index.html (28/05/2023)